# Letter of Intent: The Precision IceCube Next Generation Upgrade (PINGU)

M. G. Aartsen[b], R. Abbasi[ac], M. Ackermann[av], J. Adams[o], J. A. Aguilar[w], M. Ahlers[ac], D. Altmann[v], C. Arguelles[ac], T. C. Arlen[as], J. Auffenberg[ac], S. Axani[u], X. Bai[ai,1], M. Baker[ac], S. W. Barwick[y], V. Baum[ad], R. Bay[g], J. J. Beatty[q,r], J. Becker Tjus[j], K.-H. Becker[au], S. BenZvi[ac], P. Berghaus[av], D. Berley[p], E. Bernardini[av], A. Bernhard[ag], D. Z. Besson[aa], G. Binder[h,g], D. Bindig[au], M. Bissok[a], E. Blaufuss[p], J. Blumenthal[a], D. J. Boersma[at], C. Bohm[al], D. Bose[an], S. Böser[k], O. Botner[at], L. Brayeur[m], H.-P. Bretz[av], A. M. Brown[o], R. Bruijn[z], N. Buzinsky[u], J. Casey[e], M. Casier[m], D. Chirkin[ac], A. Christov[w], B. Christy[p], K. Clark[ap], L. Classen[v], F. Clevermann[t], S. Coenders[ag], S. Cohen[z], D. F. Cowen[as,ar,*], A. H. Cruz Silva[av], M. Danninger[al], J. Daughhetee[e], J. C. Davis[q], M. Day[ac], J. P. A. M. de André[as], C. De Clercq[m], S. De Ridder[x], P. Desiati[ac], K. D. de Vries[m], M. de With[i], T. DeYoung[as,*], J. C. Díaz-Vélez[ac], M. Dunkman[as], R. Eagan[as], B. Eberhardt[ad], B. Eichmann[j], J. Eisch[ac], S. Euler[at], J. J. Evans[ae], P. A. Evenson[ai], O. Fadiran[ac], A. R. Fazely[f], A. Fedynitch[j], J. Feintzeig[ac], T. Feusels[x], K. Filimonov[g], C. Finley[al], T. Fischer-Wasels[au], S. Flis[al], A. Franckowiak[k], K. Frantzen[t], T. Fuchs[t], T. K. Gaisser[ai], J. Gallagher[ab], L. Gerhardt[h,g], L. Gladstone[ac], T. Glüsenkamp[av], A. Goldschmidt[h], G. Golup[m], J. G. Gonzalez[ai], J. A. Goodman[p], D. Góra[v], D. T. Grandmont[u], D. Grant[u,*], P. Gretskov[a], J. C. Groh[as], A. Groß[ag], C. Ha[h,g], C. Haack[a], A. Haj Ismail[x], P. Hallen[a], A. Hallgren[at], F. Halzen[ac], K. Hanson[l], J. Haugen[ac], D. Hebecker[k], D. Heereman[l], D. Heinen[a], K. Helbing[au], R. Hellauer[p], S. Hickford[o], G. C. Hill[b], K. D. Hoffman[p], R. Hoffmann[au], A. Homeier[k], K. Hoshina[ac,ao], F. Huang[as], W. Huelsnitz[p], P. O. Hulth[al], K. Hultqvist[al], S. Hussain[ai], A. Ishihara[n], E. Jacobi[av], J. Jacobsen[ac], K. Jagielski[a], G. S. Japaridze[d], K. Jero[ac], O. Jlelati[x], M. D. Joergensen[s], O. Kalekin[v], B. Kaminsky[av], A. Kappes[v], T. Karg[av], A. Karle[ac], U. Katz[v], M. Kauer[ac], J. L. Kelley[ac], J. Kiryluk[am], J. Kläs[au], S. R. Klein[h,g], J.-H. Köhne[t], G. Kohnen[af], H. Kolanoski[i], L. Köpke[ad], C. Kopper[ac], S. Kopper[au], D. J. Koskinen[s], M. Kowalski[k], M. Krasberg[ac], C. B. Krauss[u], A. Kriesten[a], K. Krings[a], G. Kroll[ad], J. Kunnen[m], N. Kurahashi[ac], T. Kuwabara[ai], M. Labare[x], H. Landsman[ac], M. J. Larson[aq],

[*]Corresponding authors

*Email addresses:* cowen@phys.psu.edu (D. F. Cowen), deyoung@phys.psu.edu (T. DeYoung), drg@ualberta.ca (D. Grant)

[1]Physics Department, South Dakota School of Mines and Technology, Rapid City, SD 57701, USA

[2]NASA Goddard Space Flight Center, Greenbelt, MD 20771, USA

M. Lesiak-Bzdak[am], M. Leuermann[a], J. Leute[ag], J. Lünemann[ad], O. Macías[o], J. Madsen[ak], G. Maggi[m], R. Maruyama[ac], K. Mase[n], H. S. Matis[h], F. McNally[ac], K. Meagher[p], M. Merck[ac], T. Meures[l], S. Miarecki[h,g], E. Middell[av], N. Milke[t], J. Miller[m], L. Mohrmann[av], T. Montaruli[w], R. W. Moore[u], R. Morse[ac], R. Nahnhauer[av], U. Naumann[au], H. Niederhausen[am], S. C. Nowicki[u], A. Obertacke[au], S. Odrowski[ae], A. Olivas[p], A. Omairat[au], A. O'Murchadha[l], A. Palazzo[ah], T. Palczewski[aq], L. Paul[a], J. A. Pepper[aq], C. Pérez de los Heros[at], T. C. Petersen[s], C. Pfendner[q], D. Pieloth[t], E. Pinat[l], J. L. Pinfold[u], J. Posselt[au], P. B. Price[g], G. T. Przybylski[h], M. Quinnan[as], L. Rädel[a], M. Rameez[w], K. Rawlins[c], P. Redl[p], R. Reimann[a], E. Resconi[ag], W. Rhode[t], M. Ribordy[z], M. Richman[p], B. Riedel[ac], S. Robertson[b], J. P. Rodrigues[ac], C. Rott[an], T. Ruhe[t], B. Ruzybayev[ai], D. Ryckbosch[x], S. M. Saba[j], H.-G. Sander[ad], P. Sandstrom[ac], M. Santander[ac], S. Sarkar[s,aj], K. Schatto[ad], F. Scheriau[t], T. Schmidt[p], M. Schmitz[t], S. Schoenen[a], S. Schöneberg[j], A. Schönwald[av], A. Schukraft[a], L. Schulte[k], O. Schulz[ag], D. Seckel[ai], Y. Sestayo[ag], S. Seunarine[ak], R. Shanidze[av], C. Sheremata[u], M. W. E. Smith[as], D. Soldin[au], S. Söldner-Rembold[ae], G. M. Spiczak[ak], C. Spiering[av], M. Stamatikos[q,2], T. Stanev[ai], N. A. Stanisha[as], A. Stasik[k], T. Stezelberger[h], R. G. Stokstad[h], A. Stößl[av], E. A. Strahler[m], R. Ström[at], N. L. Strotjohann[k], G. W. Sullivan[p], H. Taavola[at], I. Taboada[e], A. Taketa[ao], A. Tamburro[ai], H. K. M. Tanaka[ao], A. Tepe[au], S. Ter-Antonyan[f], G. Tešić[as], S. Tilav[ai], P. A. Toale[aq], M. N. Tobin[ac], S. Toscano[ac], M. Tselengidou[v], E. Unger[j], M. Usner[k], S. Vallecorsa[w], N. van Eijndhoven[m], A. Van Overloop[x], J. van Santen[ac], M. Vehring[a], M. Voge[k], M. Vraeghe[x], C. Walck[al], T. Waldenmaier[i], M. Wallraff[a], Ch. Weaver[ac], M. Wellons[ac], C. Wendt[ac], S. Westerhoff[ac], B. J. Whelan[b], N. Whitehorn[ac], K. Wiebe[ad], C. H. Wiebusch[a], D. R. Williams[aq], W. Winter[av], H. Wissing[p], M. Wolf[al], T. R. Wood[u], K. Woschnagg[g], D. L. Xu[aq], X. W. Xu[f], J. P. Yanez[av], G. Yodh[y], S. Yoshida[n], P. Zarzhitsky[aq], J. Ziemann[t], S. Zierke[a], M. Zoll[al]

[a] *III. Physikalisches Institut, RWTH Aachen University, D-52056 Aachen, Germany*

[b] *School of Chemistry & Physics, University of Adelaide, Adelaide SA, 5005 Australia*

[c] *Dept. of Physics and Astronomy, University of Alaska Anchorage, 3211 Providence Dr., Anchorage, AK 99508, USA*

[d] *CTSPS, Clark-Atlanta University, Atlanta, GA 30314, USA*

[e] *School of Physics and Center for Relativistic Astrophysics, Georgia Institute of Technology, Atlanta, GA 30332, USA*

[f]Dept. of Physics, Southern University, Baton Rouge, LA 70813, USA

[g]Dept. of Physics, University of California, Berkeley, CA 94720, USA

[h]Lawrence Berkeley National Laboratory, Berkeley, CA 94720, USA

[i]Institut für Physik, Humboldt-Universität zu Berlin, D-12489 Berlin, Germany

[j]Fakultät für Physik & Astronomie, Ruhr-Universität Bochum, D-44780 Bochum, Germany

[k]Physikalisches Institut, Universität Bonn, Nussallee 12, D-53115 Bonn, Germany

[l]Université Libre de Bruxelles, Science Faculty CP230, B-1050 Brussels, Belgium

[m]Vrije Universiteit Brussel, Dienst ELEM, B-1050 Brussels, Belgium

[n]Dept. of Physics, Chiba University, Chiba 263-8522, Japan

[o]Dept. of Physics and Astronomy, University of Canterbury, Private Bag 4800, Christchurch, New Zealand

[p]Dept. of Physics, University of Maryland, College Park, MD 20742, USA

[q]Dept. of Physics and Center for Cosmology and Astro-Particle Physics, Ohio State University, Columbus, OH 43210, USA

[r]Dept. of Astronomy, Ohio State University, Columbus, OH 43210, USA

[s]Niels Bohr Institute, University of Copenhagen, DK-2100 Copenhagen, Denmark

[t]Dept. of Physics, TU Dortmund University, D-44221 Dortmund, Germany

[u]Dept. of Physics, University of Alberta, Edmonton, Alberta, Canada T6G 2E1

[v]Erlangen Centre for Astroparticle Physics, Friedrich-Alexander-Universität Erlangen-Nürnberg, D-91058 Erlangen, Germany

[w]Département de physique nucléaire et corpusculaire, Université de Genève, CH-1211 Genève, Switzerland

[x]Dept. of Physics and Astronomy, University of Gent, B-9000 Gent, Belgium

[y]Dept. of Physics and Astronomy, University of California, Irvine, CA 92697, USA

[z]Laboratory for High Energy Physics, École Polytechnique Fédérale, CH-1015 Lausanne, Switzerland

[aa] *Dept. of Physics and Astronomy, University of Kansas, Lawrence, KS 66045, USA*

[ab] *Dept. of Astronomy, University of Wisconsin, Madison, WI 53706, USA*

[ac] *Dept. of Physics and Wisconsin IceCube Particle Astrophysics Center, University of Wisconsin, Madison, WI 53706, USA*

[ad] *Institute of Physics, University of Mainz, Staudinger Weg 7, D-55099 Mainz, Germany*

[ae] *School of Physics and Astronomy, The University of Manchester, Oxford Road, Manchester, M13 9PL, United Kingdom*

[af] *Université de Mons, 7000 Mons, Belgium*

[ag] *T.U. Munich, D-85748 Garching, Germany*

[ah] *Max-Planck-Institut für Physik (Werner Heisenberg Institut), Föhringer Ring 6, D-80805 München, Germany*

[ai] *Bartol Research Institute and Dept. of Physics and Astronomy, University of Delaware, Newark, DE 19716, USA*

[aj] *Dept. of Physics, University of Oxford, 1 Keble Road, Oxford OX1 3NP, UK*

[ak] *Dept. of Physics, University of Wisconsin, River Falls, WI 54022, USA*

[al] *Oskar Klein Centre and Dept. of Physics, Stockholm University, SE-10691 Stockholm, Sweden*

[am] *Dept. of Physics and Astronomy, Stony Brook University, Stony Brook, NY 11794-3800, USA*

[an] *Dept. of Physics, Sungkyunkwan University, Suwon 440-746, Korea*

[ao] *Earthquake Research Institute, University of Tokyo, Bunkyo, Tokyo 113-0032, Japan*

[ap] *Dept. of Physics, University of Toronto, Toronto, Ontario, Canada, M5S 1A7*

[aq] *Dept. of Physics and Astronomy, University of Alabama, Tuscaloosa, AL 35487, USA*

[ar] *Dept. of Astronomy and Astrophysics, Pennsylvania State University, University Park, PA 16802, USA*

[as] *Dept. of Physics, Pennsylvania State University, University Park, PA 16802, USA*

[at] *Dept. of Physics and Astronomy, Uppsala University, Box 516, S-75120 Uppsala, Sweden*

[au] *Dept. of Physics, University of Wuppertal, D-42119 Wuppertal, Germany*

[av] *DESY, D-15735 Zeuthen, Germany*

**Abstract**

The Precision IceCube Next Generation Upgrade (PINGU) is a proposed low-energy infill extension to the IceCube Observatory. With detection technology modeled closely on the successful IceCube example, PINGU will feature the world's largest effective volume for neutrinos at an energy threshold of a few GeV, enabling it to reach its chief goal of determining the neutrino mass hierarchy (NMH) quickly and at modest cost. PINGU will be able to distinguish between the normal and inverted NMH at $3\sigma$ significance with an estimated 3.5 years of data. With its unprecedented statistical sample of low energy atmospheric neutrinos, PINGU will also have highly competitive sensitivity to $\nu_\mu$ disappearance, $\theta_{23}$ octant and maximal mixing, and $\nu_\tau$ appearance. PINGU can also extend the search for solar WIMP dark matter into the region currently favored by some direct dark matter experiments. At the lower end of the energy range, PINGU can use neutrino tomography to perform the first-ever direct measurement of the composition of the Earth's core. With its increased module density, PINGU will improve IceCube's sensitivity to galactic supernova neutrino bursts and enable it to extract the neutrino energy spectral shape.

*Keywords:*
neutrinos, neutrino oscillations, neutrino hierarchy, cosmic rays, dark matter, supernovae

**Contents**

# Executive Summary

This Letter of Intent describes the Precision IceCube Next Generation Upgrade (PINGU), proposed as a new in-fill array for IceCube at the South Pole Station. The primary physics goal for PINGU is precision measurement of atmospheric neutrino oscillations, with a focus on determining the neutrino mass hierarchy. Whether the mass hierarchy is normal or inverted is one of the remaining unmeasured fundamental parameters in the leptonic sector of the Standard Model, and has implications for the theoretical understanding of fundamental interactions. Determination of the mass hierarchy by PINGU also resolves possible degeneracies between the hierarchy and measurements of leptonic CP violation in long baseline experiments, and has an influence on measurements of other key unknown neutrino properties such as its Dirac or Majorana nature and the absolute mass scale.

PINGU leverages the extensive experience gained from designing, deploying and operating IceCube to achieve a project that has a short time scale to completion with minimal risk and relatively modest expense. An initial baseline detector geometry has been defined comprising 40 new strings of 60 optical modules each, deployed in the DeepCore region of the IceCube array. This dense instrumentation provides a neutrino trigger energy threshold of a few GeV and sufficient information to achieve high quality reconstructions for events between 5 and 15 GeV, where the imprint of the mass hierarchy on atmospheric neutrino oscillations is pronounced. Using the full IceCube simulation with dedicated low-energy reconstructions, the confidence with which the incorrect mass hierarchy can be excluded using this baseline PINGU geometry has been evaluated. Incorporating a wide range of detector-related systematics and uncertainties associated with the current measurements of relevant oscillation parameters, we estimate that PINGU can determine the mass hierarchy with a significance of $1.75\sigma$ with one year of data. Our studies indicate that with this unoptimized baseline PINGU detector the significance is eventually systematics limited but for the first three years scales with nearly $\sqrt{t}$, reaching a $3\sigma$ result with approximately 3.5 years of data. With several possible improvements in the analysis techniques not yet implemented, and final optimization of the detector design for this measurement still pending, we believe these estimates are robust.

PINGU will also provide substantially improved sensitivity to the on-going DeepCore neutrino oscillation measurements and dark matter searches. Estimates from studies of the baseline geometry predict the ability to establish a greater than $5\sigma$ test of the maximal nature of $\theta_{\rm atm}$ compared to current global best parameter values with 5 years of data. In addition, competitive measurements with the current world best measurements of the atmospheric mixing parameters are predicted after the first year of data taking.

The detector's low energy threshold will make it possible to search for indirect signatures of WIMP dark matter in the Sun and Galactic Center with masses as low as 5 GeV. PINGU also provides the potential for a unique tomographic measurement of the Earth's composition through exploiting the sensitivity of neutrino oscillations near 5 GeV to the proton-neutron ratio in the core. Finally, the denser instrumentation of PINGU, compared to IceCube and DeepCore, will enhance the full array's sensitivity to very low energy (approximately 15 MeV) supernova neutrino bursts, providing a predicted factor of 2 improvement in supernova sensitivity and a factor of 5 in measured precision of the average neutrino energy. Each of the above topics are discussed in detail in this Letter.

PINGU could be funded as an independent project or as part of a larger NSF MREFC project. The MREFC approach would include several additional experiments, such as an expansion of the under-ice array and a surface veto array to better observe the recently discovered extraterrestrial flux [1], and would decrease aggregate costs through resource-sharing. The estimated total US cost for PINGU, including contingency, ranges from \$55M to \$80M for the experiment as part of a larger MREFC project or as a standalone project, respectively. The assumed foreign contribution is \$25M in both cases. Detailed cost breakdowns for each scenario are provided in this Letter. We anticipate a potential completion date for the PINGU detector in the 2019/20 austral summer season.

## 1. Introduction

Over the past decade, the South Pole has emerged as a site for world-class astronomy, particle astrophysics and neutrino physics. The Amundsen-Scott South Pole Station offers very special characteristics — the deep, clear ice below the surface and the dry air and clear sky above. The glacial ice at the South Pole is 2.8 km thick and extremely clear [2], making neutrino telescopes of unprecedented scale and sensitivity possible. IceCube, the largest underground (under-ice) neutrino detector, was constructed with funding from the Major Research Equipment and Facilities Construction (MREFC) program of the National Science Foundation (NSF), (which supports the acquisition and construction of major research facilities and equipment that extend the boundaries of science, engineering, and technology) and a roughly 10% contribution from non-US sources.

Two smaller subarrays that were deployed along with IceCube – IceTop and DeepCore – are instrumental parts of the detector. DeepCore is the low energy extension of IceCube located in the lower region of the detector's center, which provides substantially increased sensitivity to neutrinos with energies of approximately 10-100 GeV. The full under ice array has been in operation since 2011, with 5160 optical sensors distributed on 86 strings (cables), transforming one gigaton of clear ice into a Cherenkov detector. IceCube detects atmospheric muons at a rate of 2800 kHz and atmospheric neutrinos at rate of more than 50,000 events per year at TeV energy scale. The IceTop surface detector consists of 162 detector tanks for measurements of air showers and, therefore, may also act as a veto against these same events for the under ice array.

The NSF's Amundsen-Scott station provides excellent infrastructure for IceCube's scientific activities, including the IceCube Laboratory building (see Fig. 1) that houses power, communications, and data acquisition systems. Because the outermost IceCube sensors can be used to veto incoming muons, background rates due to undetected muons in the deep detector can be reduced to levels comparable to deep mines. Figure 2 shows an estimate of the muon rate after applying a downward-going muon veto based on a simple majority trigger. The South Pole ice at depths below 2100 m is not only exceptionally clear but also extremely pure. The age of the ice at a depth of 2500 m is about 100,000 years, and radioactive contaminants in the deep ice are in the range of 0.1-1 $\times 10^{-12}$ g(Uranium or Thorium)/g and 0.1-1 $\times 10^{-9}$ g(Potassium)/g . The cold environment greatly reduces thermionic electron noise in the photomultipliers. Thus, the South Pole provides a unique environment to host future detectors.

The recent successful detection of high energy neutrinos of astrophysical origin by Ice-

Figure 1: The IceCube Laboratory building houses power, communications and data acquisition systems for IceCube and other experiments at the South Pole (photo by S. Lidström).

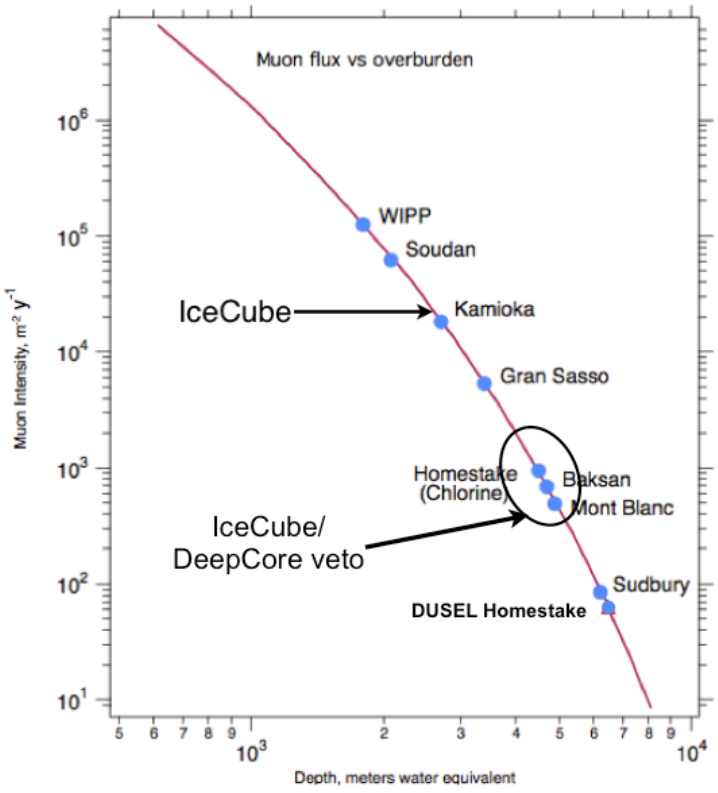


Figure 2: Estimated muon rate in the deep ice after applying a veto based on a simple majority trigger.

Cube [1], as well as measurements of neutrino oscillations [3, 4] and world-leading searches for dark matter [5] with DeepCore, has led the IceCube Collaboration to begin investigating possible extensions of IceCube with improved performance at both high and low energy. The technological solutions to drill and deploy instruments in the deep ice exist, the risks are small, and the costs are understood. In addition, it is possible to share the costs of operational support across multiple new experiments, such as winter-over personnel to maintain the detector and general support for new groups, in cooperation with NSF and the Antarctic support contractor.

At high energy, an expanded detector in the deep ice and an improved surface array for identifying the air showers that produce atmospheric neutrinos are under consideration. At low energy, the Precision IceCube Next Generation Upgrade (PINGU) is proposed as an in-fill array for IceCube. PINGU is designed to determine the neutrino mass hierarchy (NMH) using atmospheric neutrinos that undergo Mikheyev-Smirnov-Wolfenstein (MSW) [6, 7] and parametric [8] oscillations as they pass through the Earth. Whether the NMH is normal or inverted represents one of the remaining unmeasured fundamental parameters in the neutrino sector and its nature has deep implications for the theoretical understanding of fundamental interactions. In particular, its measurement would allow us to distinguish between certain theoretical models at the GUT mass scale [9]. A measurement of the hierarchy would also impact ongoing and future research of other crucial neutrino properties. In fact, the unknown NMH is a major ambiguity in running or approved accelerator neutrino oscillation experiments with sensitivity to leptonic CP-violation [10, 11, 12, 13]. In addition, the determination of the NMH will influence the interpretation of non-oscillation experiments (neutrinoless double beta decay and beta decay) sensitive to the particle nature of the neutrino (Dirac vs Majorana) and/or its absolute mass [14], and will thus help to test popular see-saw neutrino mass models and the related mechanism of leptogenesis in the early universe [15].

There are a number of operating and planned experiments with sensitivity to the neutrino mass hierarchy. The NOvA experiment [16] in the NuMI beam line at Fermilab can determine the hierarchy at $3\sigma$ for a limited range of values of the CP-violating phase ($\delta_{\mathrm{CP}}$) [17]. This range is extended with the inclusion of results from T2K [18] and further still with the proposed CHIPS [19] experiment. PINGU's observations would essentially be insensitive to $\delta_{\mathrm{CP}}$, a determination of the mass hierarchy by PINGU is highly complementary to these efforts, resolving possible degeneracies between the mass hierarchy and CP violation and possibly increasing the precision with which CP violation can be measured by these long baseline experiments.

In the longer term, LBNE [20] could make a $3\sigma$ determination of the hierarchy for all values of $\delta_{\rm CP}$ with less than 10 years of operation, while JUNO [21] in China and RENO-50 [22] in South Korea are proposed to exploit reactor neutrino oscillations at medium-scale baselines of about 50-60 km to measure the hierarchy above $3\sigma$ with 6 years of operation. The ICAL at INO [23] proposes to use charge discrimination to distinguish between neutrinos and anti-neutrinos to determine the hierarchy with between $2.2 - 2.8\sigma$ significance using 10 years of data with a 50 kton detector. Measurements of neutrinos from a nearby supernova, the CMB polarization, and neutrinoless double beta decay may also each provide indirect sensitivity to the hierarchy [17]. PINGU offers the possibility of a more rapid determination of the mass hierarchy via a very different type of measurement than those made by LBNE, JUNO, or RENO-50, as shown in Fig. 3.

Throughout the full range of neutrino oscillation parameter space, the complementarity of PINGU, beam and reactor experiments provides the surest path to determining the NMH, with synergistic effects that can improve the combined significance beyond purely statistical addition of results [26]. Consistency in the results obtained from several of these experiments would provide assurance that our interpretation of the results in the three-flavor neutrino paradigm is indeed correct.

Our simulations of PINGU, informed by experience with IceCube, and in particular DeepCore data, indicate that our reconstruction algorithms will provide sufficient angular and energy resolutions. Known systematic errors are found to be sufficiently small to enable a measurement of the neutrino mass hierarchy with $1.75\sigma$ precision with one year of data. This estimate is based on a conservative analysis in which the detector geometry has yet to be carefully optimized and a number of possible improvements, such as the use of event elasticity to provide some $\nu$-$\bar{\nu}$ separation or downgoing atmospheric neutrinos to provide an oscillation-free control sample, have not yet been included, increasing our confidence in this estimate.

In addition, PINGU will have enhanced sensitivity to other important neutrino oscillation physics. It would be capable of high precision measurements of atmospheric muon neutrino disappearance and tau neutrino appearance, and would be able to study whether or not the mixing angle $\theta_{23}$ is maximal. PINGU would also probe a lower WIMP dark matter mass range in searches for these particles annihilating to neutrinos in the terrestrial and solar cores, the galactic center, dwarf spheroidals and other candidate astrophysical WIMP dark matter accumulators. The detector also has the potential to provide a neutrino-based tomography of the Earth, and enhanced sensitivity to very low energy neutrinos from supernovae.

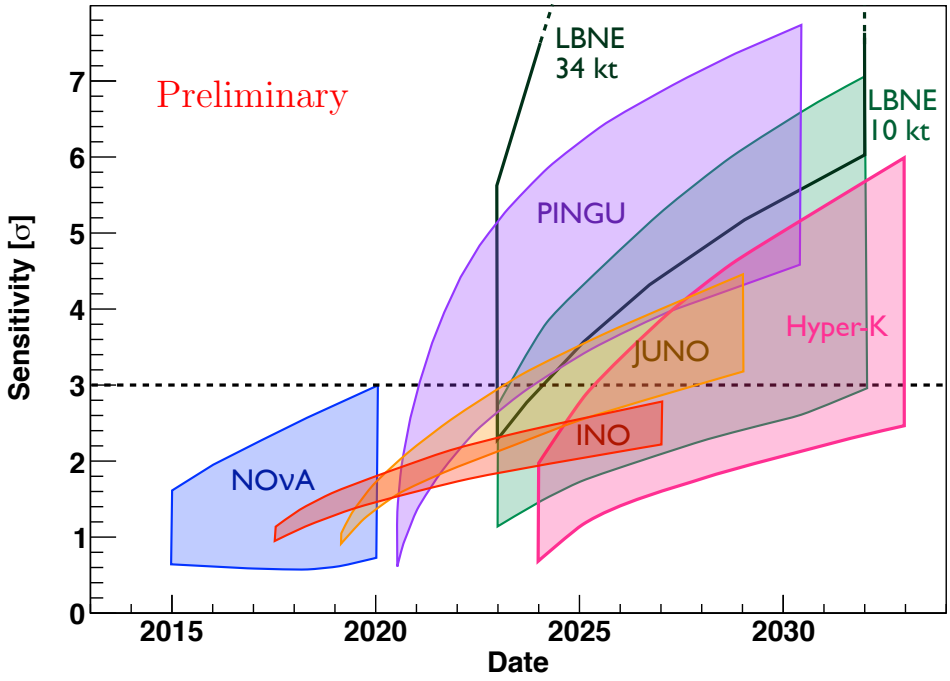


Figure 3: Comparison of the expected sensitivities (for rejecting the inverse hierarchy assuming the normal hierarchy) of different experiments with the potential to measure the neutrino mass hierarchy, following [24]. The widths of the bands cover the maximum sensitivity differences corresponding to the two hierarchy cases in combination with true values of the CP phase $\delta$ for NOvA and LBNE, different energy resolutions ranging from $3.0\%\sqrt{1\text{ MeV}/E}$ to $3.5\%\sqrt{1\text{ MeV}/E}$ for JUNO, and atmospheric mixing angles $\theta_{23}$ ranging from the first to the second octant for PINGU (38.7° to 51.3°) and INO (40° to 50°). The starting date and growth of sensitivity with time for PINGU are those presented in this letter, and all other curves are taken from [24] (Fig. 11), where the left and right plots of that figure have been merged to form the largest envelope from the curves for each experiment. Finally, the Hyper-K sensitivity is from [25].

PINGU will be composed of the same sensors, and installed using the same techniques and equipment as the IceCube high energy extensions under consideration, potentially leading to substantial scaling efficiencies. The estimated total US cost for PINGU, including contingency, ranges from \$55M to \$80M for the experiment as one of several IceCube extensions or as a standalone project, respectively. The assumed foreign contribution is

$25M in both cases. Detailed cost breakdowns for each scenario are provided in Table 8. The expertise developed in designing, deploying, and operating IceCube means that the PINGU could be deployed quickly and with well-understood and minimal risk. Because PINGU is designed as an extension of IceCube, close integration with IceCube's online and offline systems will be straightforward, enabling us to use the surrounding IceCube DOMs to provide a nearly hermetic active veto against downward-going cosmic ray muons, the chief background of all PINGU physics channels. In addition, the incremental cost of both developing software systems and operating PINGU will be dramatically lower than normal for a project of this scale.

This Letter of Intent presents the detailed physics cases for the neutrino mass hierarchy, muon neutrino disappearance, maximal mixing, Earth tomography, supernova neutrinos and WIMP dark matter indirect detection measurements. We describe the baseline design of the PINGU detector and requirements for the hot water drill, highlighting salient points of departure from that used in IceCube [27, 28, 29]. With an eye towards future detectors beyond PINGU, we also describe planned R&D efforts to build new photon collection devices for co-deployment on PINGU strings. Finally, we provide an estimate of the schedule and cost for the design, construction, deployment and operation of PINGU.

## 2. Detector Design and Predicted Performance

### *2.1. Introduction*

The PINGU design follows closely that which was used for IceCube and DeepCore. A further in-fill of the central DeepCore volume, using hardware similar to standard DeepCore Digital Optical Modules (DOMs), will ultimately lower the energy threshold and significantly improve the sensitivity for neutrinos below 20 GeV.

### *2.2. Detector Geometries*

We have simulated several detector geometries but principally report the results from the baseline 40-string geometry. Feasible geometries are those that can be deployed in either a two- or three-year period and have adequate inter-string horizontal spacing and sufficient inter-DOM vertical spacing to satisfy drilling and deployment constraints. The baseline 40-string geometry and a 20-string geometry are detailed in Table 1. An artist's rendering of the existing IceCube array is shown in Fig. 4, and overhead and side views of the baseline PINGU geometry are shown in Fig. 5 along with a sketch of signal and background event topologies. The 20-string geometry shown in Table 1 is not adequate for measuring the hierarchy, but was used to study the sensitivty of PINGU to MeV-scale neutrinos from supernovae. Additional detector geometries are presently under study to maximize the sensitivity of PINGU to the neutrino mass hierarchy.

| Number of Strings | Average Inter-string Spacing | Number of DOMs/String | Inter-DOM Spacing |
|---|---|---|---|
| 20 | 26 m | 60 | 5 m |
| 40 | 20 m | 60 | 5 m |

Table 1: The baseline 40-string PINGU detector geometry used in this study, and an alternate 20-string geometry investigated for studies of supernova neutrinos.

The effective volume at analysis level is defined as

$$V_{\text{eff}} = V_{\text{gen}} \times \frac{N^{\nu}_{\text{reco}}}{N^{\nu}_{\text{gen}}}, \tag{1}$$

where $V_{\text{gen}}$ is a large volume in which simulated neutrinos may interact, $N^{\nu}_{\text{reco}}$ is the number of neutrinos passing all analysis selection criteria, and $N^{\nu}_{\text{gen}}$ is the total number

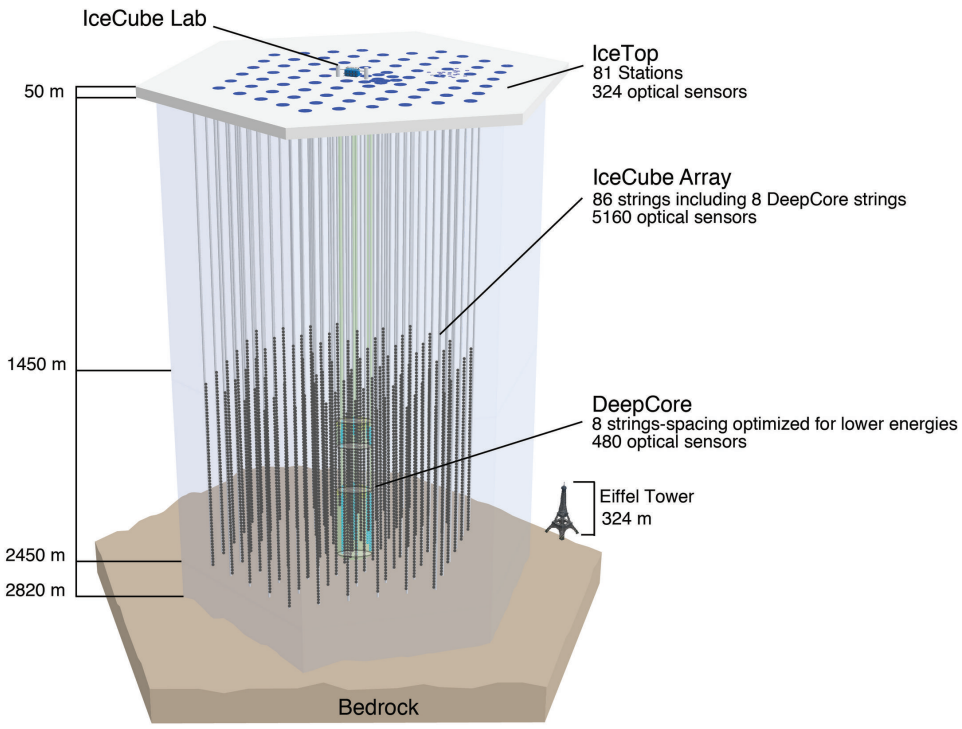


Figure 4: Artist's rendering of the IceCube and DeepCore detectors. The PINGU detector strings would in-fill the existing DeepCore array at similar depths, with substantially closer vertical spacing between modules.

of neutrinos generated. Using the final event selection for the neutrino mass hierarchy measurement described in Sec. 4.1.1, this is shown as a function of energy for muon neutrinos in Fig. 6(a) and for electron neutrinos in Fig. 6(b).

### *2.3. Detector Hardware and Simulation*

Although some changes will be made to the DOM electronics, as described in detail in Sec. 10, the single photoelectron (SPE) data extracted from PINGU DOMs (PDOMS) will be essentially identical to that of DeepCore DOMs. We have therefore simulated PINGU using IceCube Monte Carlo software. To ensure accurate simulation of low energy events, the GENIE [30] generator was used to model neutrino interactions, GEANT4 [31] was used to propagate particles through the detector (including full simulation of all secondaries

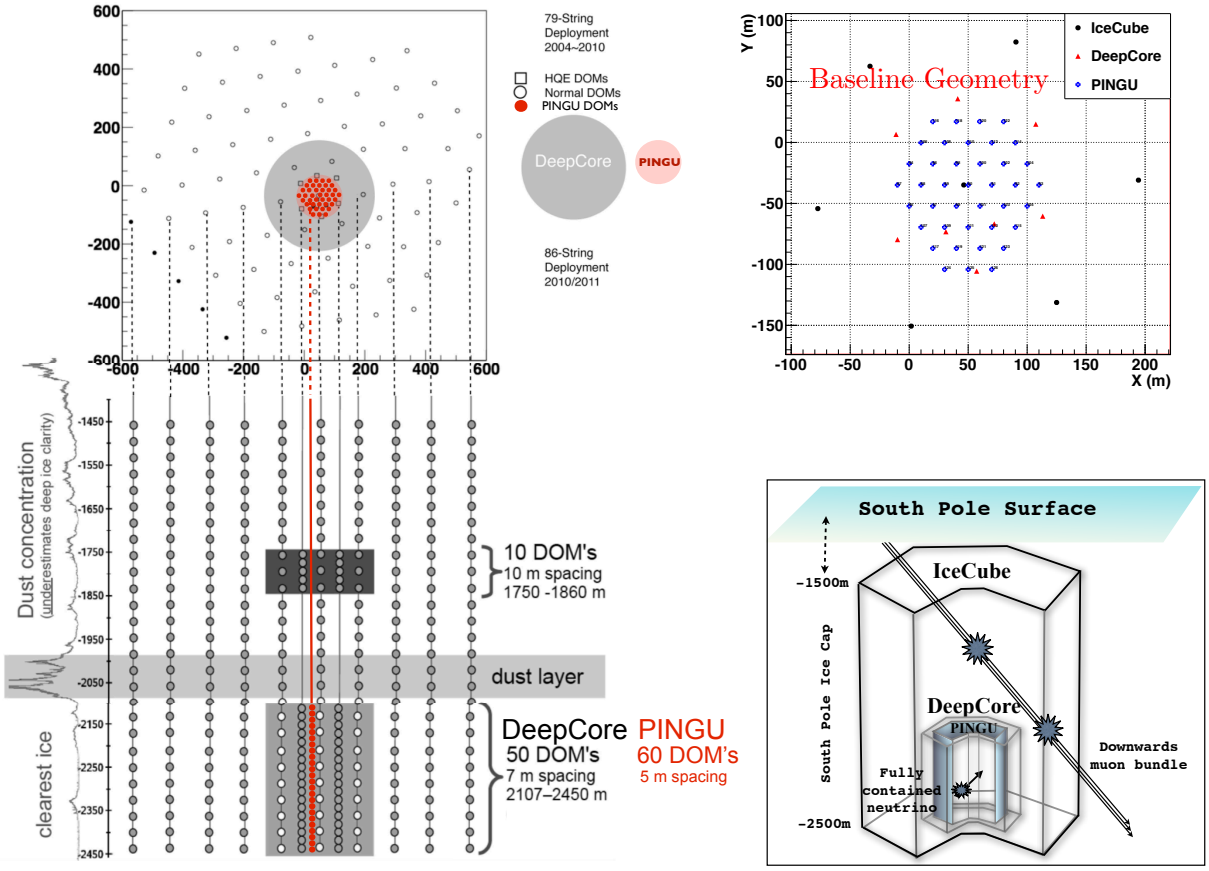


Figure 5: The left figure shows overhead and side views of the baseline 40-string PINGU detector. It also shows the surrounding IceCube and DeepCore strings, and vertical spacings for DeepCore and PINGU modules. In the side view only some of the strings are shown for clarity. Like DeepCore, the PINGU modules will all house high quantum efficiency (HQE) PMTs. The leftmost plot along the side of the figure delineates the dust concentration in the ice and shows that PINGU occupies the clearest ice. The top right figure shows an enlarged top view of the baseline 40-string geometry. The bottom right figure provides a sketch of a contained $\nu_\mu$ CC event (signal) and a throughgoing muon bundle from a cosmic-ray air shower (one type of background, rarely coincident with neutrinos but shown this way for simplicity).

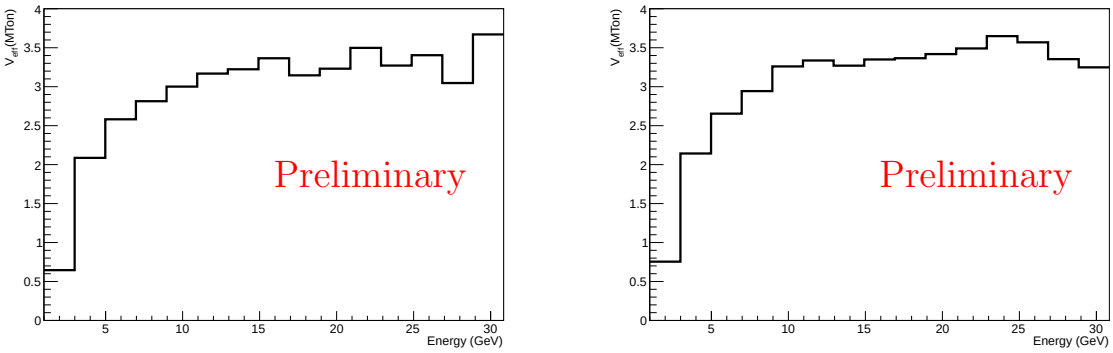


(a) $V_{eff}(\nu_\mu)$ (b) $V_{eff}(\nu_e)$

Figure 6: Effective volume for muon (left) and electron (right) neutrinos in PINGU in the baseline 40-string configuration as a function of neutrino energy. Only events passing the final event selection criteria described in Sec. 4.1.1 are included in the plots.

produced at the interaction vertex), and Cherenkov photons were tracked individually through the detector using the CLSim GPU-based software (similar to that described in Ref. [32]) to treat the depth-dependent Mie scattering observed in IceCube (see 13.4 for more details).

### *2.4. Event Reconstruction*

The most detailed PINGU reconstruction employs likelihood methods at the single photon level for energy estimation, direction reconstruction and/or particle identification. Since the scattering length of Cherenkov photons in the deep Antarctic ice is approximately 20-30% that of the absorption length, we are in an intermediate regime between free-streaming photons and diffusive propagation and must rely on numerical descriptions of light propagation through the ice. The expected detector responses are computed and tabulated for a variety of event topologies in the detector. These tables are then fit with splines to reduce numerical instabilities from the binning and ensure a smooth parametrization. To reconstruct an event, all DOM readouts are subdivided in time, and a Poisson likelihood is calculated for the contents of each time bin, in all DOMs in PINGU and IceCube, comparing a reconstruction hypothesis to the data. The hypothesis is adjusted, and the process is repeated until the hypothesis with the maximum likelihood is found.

PINGU is designed to observe neutrinos with energies as low as a few GeV. At this

energy scale, most or all of the secondary particles and Cherenkov photons created in the neutrino event will be contained within the detector volume; this is a significant change from the typical events observed by the IceCube detector, the vast majority of which are high energy through-going muons from cosmic ray air showers. Furthermore, at neutrino energies below roughly 100 GeV, the hadronic shower at the interaction vertex can contribute a significant fraction of all the Cherenkov photons detected in the event and must be considered in event reconstruction. However, stochastic processes such as bremsstrahlung are much rarer than at high energies, and muon tracks produced by $\nu_\mu$ CC events can safely be assumed to be minimum-ionizing particles.

For these reasons, we have developed a new reconstruction strategy for the low energy events that are relevant for the measurement of the NMH. We perform a simultaneous global likelihood fit to all eight event parameters: the interaction vertex position and time, the zenith and azimuthal angles, the energy of the cascade at the vertex, and the length of the daughter muon (only truly present for $\nu_\mu$ CC events). It is possible to extract the measured event inelasticity from the fit and use that information to improve the neutrino mass hierarchy sensitivity [33], but in this letter we do not take advantage of this. In principle, for $\nu_\mu$ CC events the muon and the hadronic shower at the interaction vertex are not perfectly aligned with each other, and their relative directions could be treated as independent parameters in the fit, but here we treat them as collinear. The event inelasticity and complete interaction kinematics will be explored in future refinements of the analyses presented here.

We use the nested sampling algorithm MultiNest [34] to determine the best point in the eight dimensional likelihood space describing the event. MultiNest was applied to fully simulated $\nu_\mathrm{e}$, $\nu_\mu$ and $\nu_\tau$ PINGU events, producing the two main signatures (tracks and cascades), for the baseline 40-string geometry shown in Table 1. The reconstructed vertex of each event was required to be contained within the PINGU fiducial volume, defined as a cylinder (radius 75 m and height 250 m) coaxial with the central PINGU string, 25 m below its topmost module, and 25 m above its bottommost. The zenith angle resolution ($|\theta_\mathrm{true} - \theta_\mathrm{reco}|$) and fractional energy resolution ($|E_{\nu,\mathrm{reco}} - E_{\nu,\mathrm{true}}|/E_{\nu,\mathrm{true}}$) are shown for $\nu_\mu$ in Figs. 7(a) (with respect to the outgoing muon), 7(b) (with respect to the incoming neutrino), and 7(c). For $\nu_\mathrm{e}$ the angle and energy resolutions are shown in Figs. 8(a) and 8(b).

The MultiNest algorithm successfully reconstructs about 90% of atmospheric neutrino events that satisfy a loose trigger criterion (three modules hit in spatial and temporal coincidence) and whose true vertex is contained within the PINGU fiducial volume; these

events produce enough photoelectrons to fully constrain the fit. Although many of the 10% of events for which the algorithm fails can be recovered by re-running the fit with a different random selection of starting points, at present we only use events that pass on the first try. Table 2 shows the reconstruction efficiency for MultiNest for each neutrino flavor and interaction.

| Flavor (Interaction) | $N_{\mathrm{reco}}/N_{\mathrm{total}}$ |
|---|---|
| $\nu_{\mathrm{e}}$(CC) | $90.1 \pm 0.5\%$ |
| $\nu_{\mu}$(CC) | $93.1 \pm 0.6\%$ |
| $\nu_{\tau}$(CC) | $99.0 \pm 1.0\%$ |
| $\nu$(NC) | $87.2 \pm 1.7\%$ |

Table 2: Efficiencies for MultiNest reconstruction of neutrinos, defined as the ratio $N_{\mathrm{reco}}/N_{\mathrm{total}}$; the number of events successfully reconstructed inside the fiducial volume divided by the total number of events satisfying the trigger condition whose true vertex is contained. The neutrinos have energies between 1-80 GeV and follow an atmospheric spectrum [35]. Tau neutrinos have a higher efficiency due to kinematic effects that reduce the number of low energy tau neutrinos that trigger the detector, resulting in an energy spectrum is peaked at higher energies than for other neutrino flavors.

### *2.5. Cosmic-Ray Muon Background Rejection*

Downward-going atmospheric muons outnumber atmospheric neutrinos by a factor of roughly $10^6$:1 at PINGU detector depths, and criteria must be put in place to reject this background at high efficiency. The published analysis of showering events induced by atmospheric neutrinos [36] in IceCube's DeepCore detector attained an atmospheric muon rejection factor of over $10^7$ by vetoing events with early light in the surrounding IceCube modules. Furthermore, the improved reconstruction performance for low energy events described in Sec. 2.4 also provides the possibility to reject any remaining downward-going events based on the reconstructed direction (at the cost of rejecting downward-going neutrinos). Thus we do not anticipate contamination from this particular source of background in PINGU.

### *2.6. Particle ID*

The ability to separate the track-like events created by $\nu_{\mu}$ CC events (and a small fraction of $\nu_{\tau}$ CC events) from the cascade-like events arising from other neutrino interactions

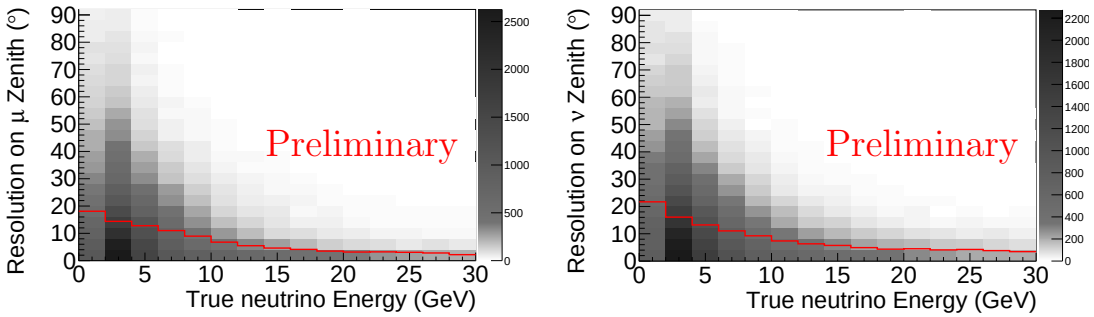


(a) $|\theta_{\mu,\text{true}} - \theta_{\mu,\text{reco}}|$ vs. $E_{\nu,\text{true}}$.

(b) $|\theta_{\nu,\text{true}} - \theta_{\nu,\text{reco}}|$ vs. $E_{\nu,\text{true}}$.

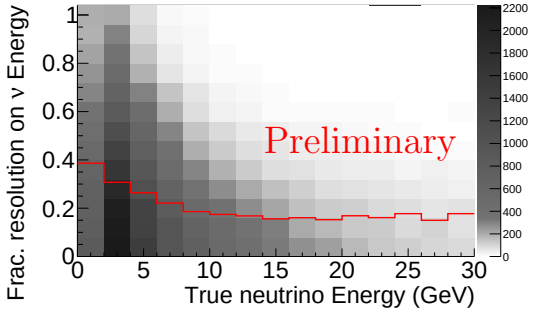


(c) $|E_{\nu,\text{reco}} - E_{\nu,\text{true}}|/E_{\nu,\text{true}}$ vs. $E_{\nu,\text{true}}$.

Figure 7: Zenith angle and fractional energy resolutions for $\nu_\mu$ events with reconstructed vertices within the PINGU fiducial volume. The red line indicates the median value in each bin. The gray scale indicates number of simulated events in each bin.

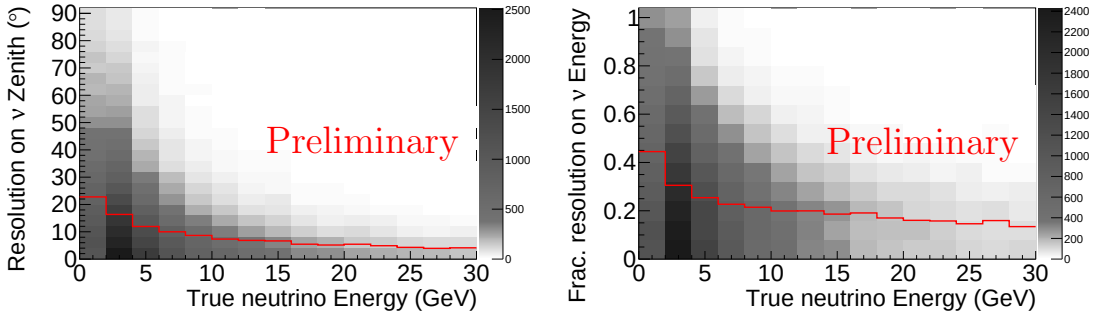


(a) $|\theta_{\nu,\text{true}} - \theta_{\nu,\text{reco}}|$ vs. $E_{\nu,\text{true}}$.

(b) $|E_{\nu,\text{reco}} - E_{\nu,\text{true}}|/E_{\nu,\text{true}}$ vs. $E_{\nu,\text{true}}$.

Figure 8: Zenith angle and fractional energy resolutions for $\nu_\text{e}$ events with reconstructed vertices within the PINGU fiducial volume. The red line indicates the median value in each bin. The gray scale indicates number of simulated events in each bin. The resolutions for $\nu_\tau$ and NC events are similar.

would benefit many PINGU analyses. Initial studies using variables such as the reconstructed muon track length and the relative quality of fit for a track vs cascade hypothesis in a binary decision tree using the FisherG method [37] show promise. Figure 9 shows the separation achieved in these initial studies.

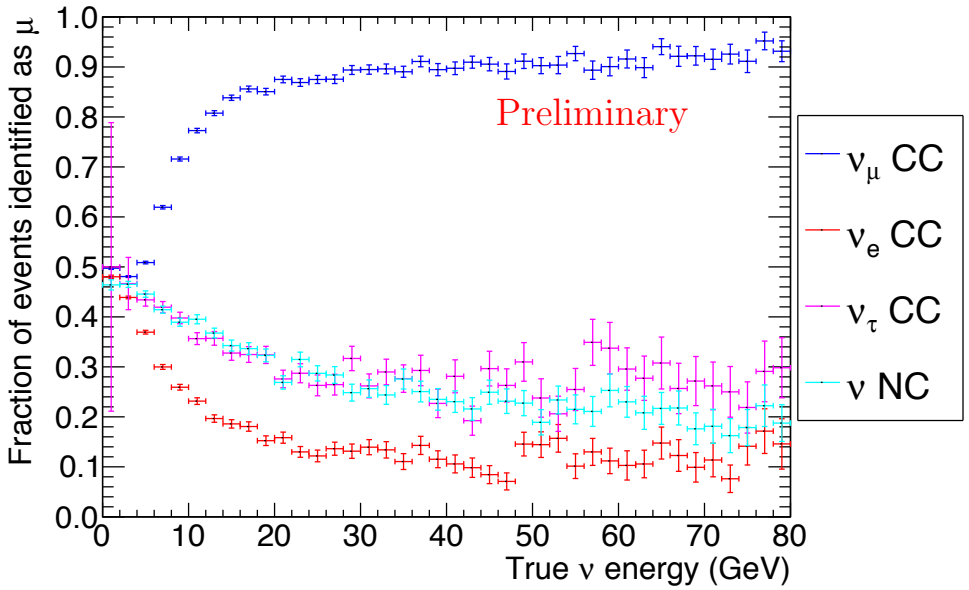


Figure 9: The fraction of events identified as track-like as a function of true neutrino energy for each neutrino flavor and interaction, using the TMVA Fisher discriminant method with Gauss-transformed input variables [37].

## 3. Neutrino Oscillations

The mixing angles and mass-squared differences that describe oscillations in the neutrino sector have been measured with good precision through the efforts of a variety of experiments worldwide [38]. The remaining unknowns in the leptonic sector include the nature of the neutrino (Dirac or Majorana), the extent to which Charge-Parity symmetry may be violated in the sector, and the ordering of the mass eigenstates. The ordering, or mass hierarchy, is denoted "normal" (NH) when $\nu_3$ is the most massive of the three neutrino mass eigenstates and "inverted" (IH) if it is the least. This ordering can be described in terms of the sign of mass-squared difference measured by atmospheric neutrino oscillation experiments, $\Delta m^2_{\rm atm}$, where $\Delta m^2_{\rm atm} > 0$ corresponds to the normal hierarchy and $\Delta m^2_{\rm atm} < 0$ to the inverted. To minimize the dependence of the absolute value of $\Delta m^2_{\rm atm}$ on the hierarchy, we define $\Delta m^2_{\rm atm} = |m^2_3 - \frac{1}{2}(m^2_1 + m^2_2)|$, rather than $\Delta m^2_{32}$, following the convention of [39].

Atmospheric neutrino studies have proven to be effective in constraining oscillation parameters, including the discovery of neutrino oscillations and the first measurements of $\theta_{23}$. In addition to vacuum oscillations there are two distinct physical effects that play a role in the oscillations as neutrinos propagate through the Earth. The first is the MSW effect [6, 7] that enhances the oscillation probability for $\nu_\mu \to \nu_e$ (NH), or $\bar{\nu}_\mu \to \bar{\nu}_e$ (IH), which is strongly dependent on the matter density for all path lengths through the Earth. The second effect arises from the density transition at the Earth's mantle-core interface (see Fig. 10) where neutrinos passing through this interface can undergo "parametric enhancement" of their oscillation probability [8].

The survival probabilities for atmospheric muon neutrinos that reach the detector after propagation through the Earth (i.e., from below) depend on $E$ and propagation length ($L$). Since propagation length is strictly correlated with arrival direction, the zenith angle is used as a proxy for $L$ and a common observable used is a two-dimensional event distribution binned in energy and zenith angle for a sample of atmospheric muon neutrinos. The aggregate effect of the Earth-crossing phenomena on muon neutrinos, in both the NH and IH scenarios, is shown in Fig. 11. The survival probabilities of antineutrinos in the NH are essentially identical to those of neutrinos in the IH, and vice versa. Under these circumstances, the distribution measured by a detector like PINGU is effectively the sum of the two distributions shown in Fig. 11, which look the same regardless of the hierarchy, making discrimination between the hierarchies appear unattainable. However, the asymmetries in the cross sections and kinematics of $\nu$ and $\bar{\nu}$ interactions with nuclei, and the higher atmospheric flux of neutrinos relative to antineutrinos, lead to different detected

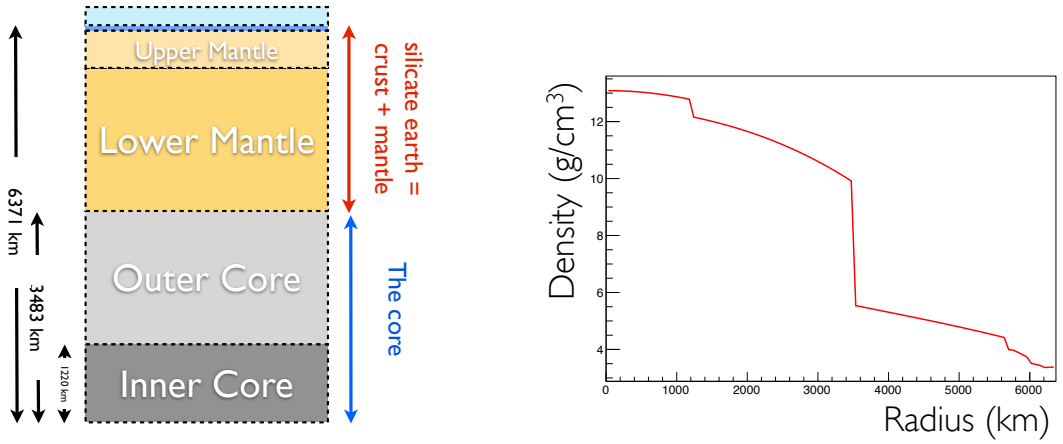


Figure 10: Structure of the Earth and density as a function of radius $r$ from the center, showing the large change in density at $r \simeq 3500$ m. This provides the foundation for the preliminary reference Earth model (PREM) [40] used to map Earth's interior mass density and to account for matter effects in neutrino oscillations.

event rates depending on the hierarchy. Therefore a precision measurement of the survival probabilities in the energy range targeted by PINGU in the presence of these matter effects permits a determination of the NMH without explicit $\nu - \bar{\nu}$ discrimination [41].

IceCube with its DeepCore extension has demonstrated the ability to measure the "atmospheric" mixing parameters, and further improvements toward becoming competitive with world-leading experiments in this area are expected as analysis techniques are refined and systematic uncertainties are better understood. Besides the mass hierarchy and the value of the $\delta_{\mathrm{CP}}$, an additional open question in the neutrino sector, as parameterized by the Pontecorvo-Maki-Nakagawa-Sakata (PMNS) matrix, is whether mixing is maximal in the atmospheric ("23") domain. Maximal atmospheric mixing refers to the case $\theta_{23}$=45° which implies that $\nu_3$ contains equal fractions of muon and tau neutrinos. Most measurements thus far are consistent with maximal mixing, but a global analysis [42] of all oscillation measurements finds evidence for non-maximality at a 2-3$\sigma$ level, depending on mass hierarchy. If atmospheric mixing is non-maximal, it remains to determine in which "octant" the mixing angle $\theta_{23}$ lies. For a $\theta_{23}$ in the first octant ($< 45°$) the mass eigenstate $\nu_3$ is "tau heavy," i.e., the tau neutrino fraction is larger than the muon neutrino fraction. Conversely, for a $\theta_{23}$ in the second octant ($> 45°$) the state $\nu_3$ is "muon heavy." Currently, both the octant of $\theta_{23}$ and its deviation from 45° are unknown and contribute to the problem of parameter degeneracy for neutrino oscillation measurements.

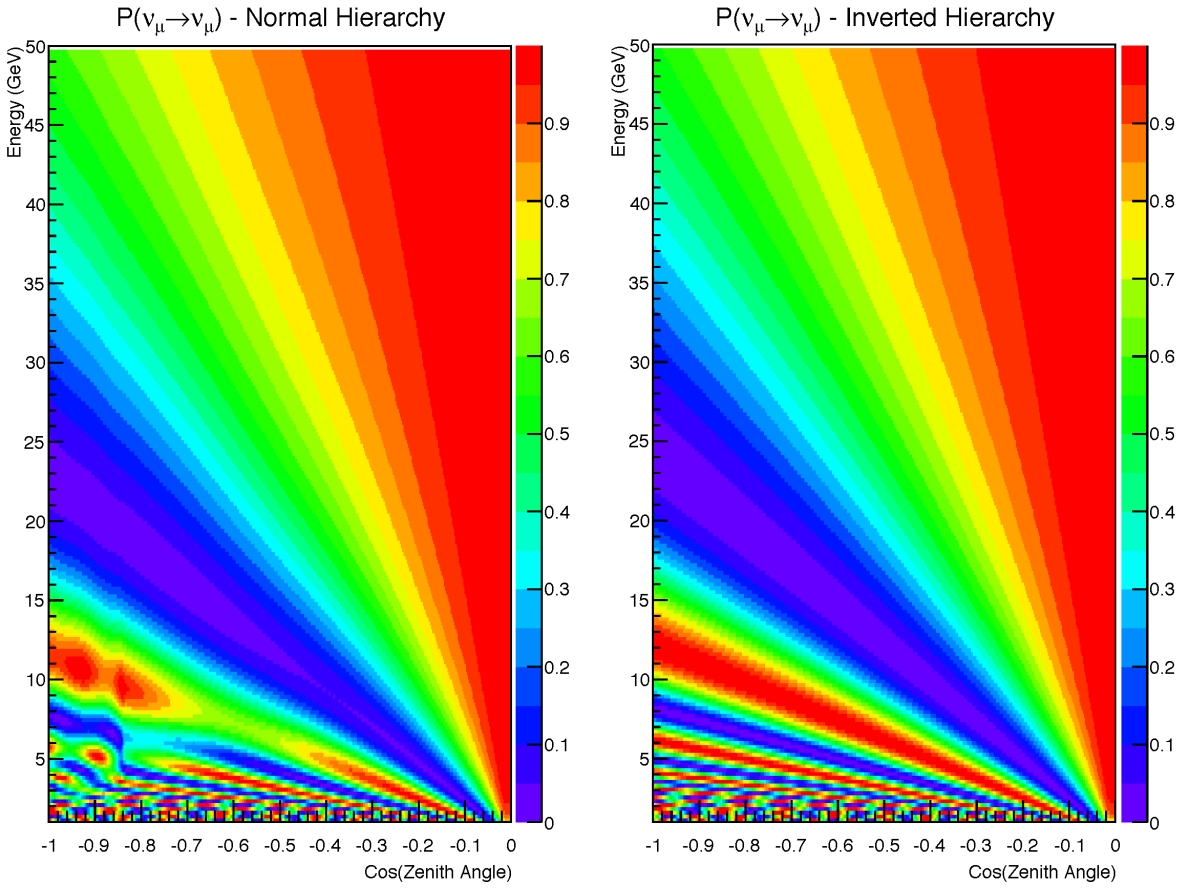


Figure 11: Muon neutrino survival probability after traveling through the earth, binned in both neutrino energy and cosine of the zenith angle. (A path directly through the center of the Earth corresponds to $\cos\theta = -1$.) The survival probabilities for antineutrinos in a given hierarchy are essentially the same as those for neutrinos under the opposite hierarchy.

In the following sections, we present results that use atmospheric neutrinos in the energy range of 1-80 GeV with fluxes as predicted by [35]. The neutrinos are tracked through the Earth using a full three-flavor formalism including matter effects based on the standard PREM model of the Earth. The PINGU sensitivity to the mass hierarchy, capable of determining this mass ordering by virtue of its ability to collect a high-statistics sample of atmospheric neutrinos in the energy range above roughly 5 GeV, is discussed in Sec. 4. Sections 5 and 6 present the expectations for PINGU to provide precision extraction of the oscillation mixing parameters and test of the maximal nature of the atmospheric neutrino

mixing angle, respectively. Finally, from the expected atmospheric neutrino oscillation signature, Sec. 7 presents the expectation for identifying the composition of the inner Earth core using neutrino tomography.

## 4. Neutrino Mass Hierarchy

The impact of the MSW effect and parametric enhancement on atmospheric neutrinos, and thus the signal for determining the hierarchy, is illustrated in Fig. 12. The figure shows the difference between the number of detected neutrino events per year under each hierarchy, after applying the selection criteria and event reconstruction described below, scaled by the Poisson error on the number of NH events to obtain something analogous to a $\chi^2$ term. The plots are binned as a function of the reconstructed neutrino energy, $E_\nu$, and the cosine of the reconstructed zenith angle of the neutrino ($\cos\theta_\nu$). To illustrate the individual contributions to the NMH signal, each neutrino flavor is shown separately, i.e., assuming perfect flavor identification. One finds regions in which the number of events expected for the NH is greater than that expected for the IH (blue regions) and vice-versa (red regions). Sensitivity to this pattern of the event number differences as a function of $E_\nu$ and $\cos\theta_\nu$ permits one to determine the neutrino mass hierarchy. This "distinguishability" metric [43] is useful for understanding the regions of interest in the energy-angle space from which useful information may be extracted, and can be used to calculate a rough approximation of the PINGU sensitivity to the NMH. More detailed simulations and analysis methods are then used to determine the sensitivity with improved accuracy, as discussed below.

### *4.1. Analysis*

#### *4.1.1. Simulated Dataset and Event Selection*

The simulated neutrino events (see Sec. 2.3) are reconstructed without regard to neutrino flavor and employ a basic algorithm for particle identification (PID) to separate track-like events produced by $\nu_\mu$ CC interactions from cascade-like events produced by $\nu_e$ CC, $\nu_\tau$ CC, and all-flavor NC interactions. We also conservatively reject downward-going atmospheric neutrinos using the reconstructed event direction although, in the future, the subset of these events that start in the PINGU fiducial volume could be retained and used for normalization of the intrinsic flux to further mitigate systematics.

Events that are successfully reconstructed using the procedure described in Sec. 2.4 are then required to satisfy the following additional containment and directional criteria:

- reconstructed $\nu$ vertex within 75 m radially from the central axis of PINGU

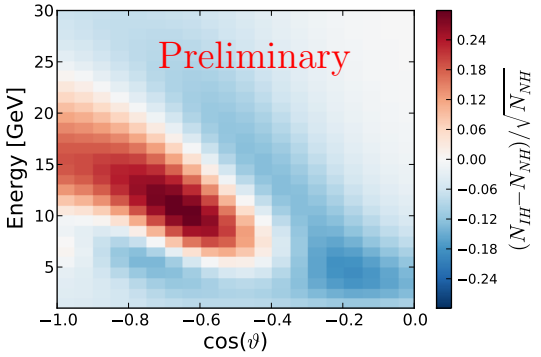


(a) $\nu_\mu$ CC events.

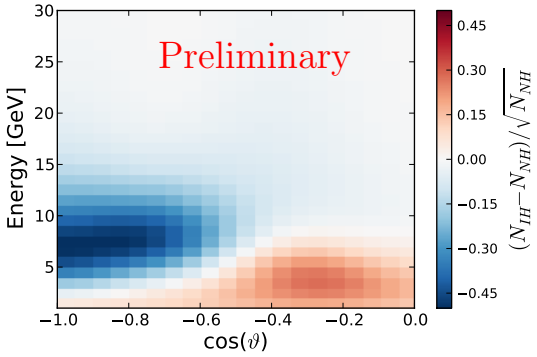


(b) $\nu_\mathrm{e}$ CC events.

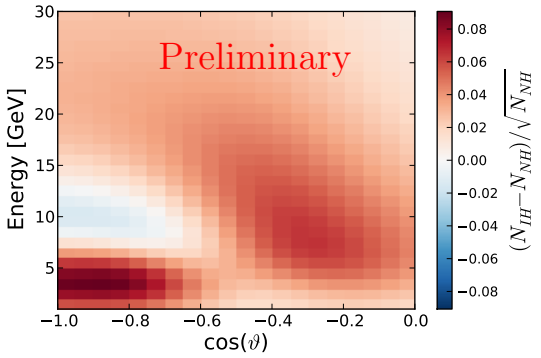


(c) $\nu_\tau$ CC events.

Figure 12: Distinguishability metric as defined in [43] for one year of simulated PINGU data, with parametrized reconstruction resolutions as described in Appendix A. The sum of the absolute values of each bin in each plot gives an estimate of the number of $\sigma$ separating the two hierarchies. For illustrative purposes we assume perfect particle ID in creating these figures. The top left figure shows track-like events from CC $\nu_\mu$ interactions. The top right figure shows $\nu_\mathrm{e}$ CC events and bottom $\nu_\tau$ CC.

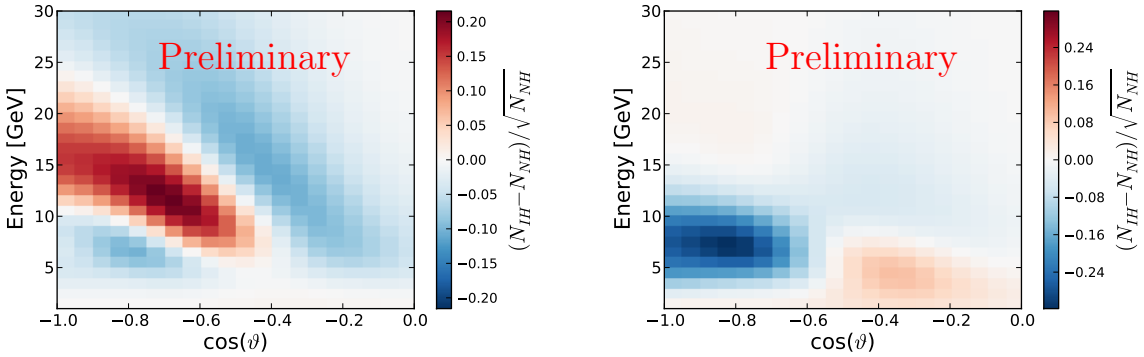


(a) Track-like events.

(b) Cascade-like events.

Figure 13: Distinguishability metric as defined in [43] for one year of simulated PINGU data with reconstruction and particle identification applied. The left panel shows track-like events (mostly due to CC $\nu_\mu$) while the right shows cascade-like events (mostly $\nu_e$ and $\nu_\tau$ CC events, as well as NC events from any neutrino flavors).

- reconstructed vertex depth within PINGU or the IceCube instrumented volume directly below PINGU
- $\theta_{\text{rec}} > 90°$ (all events are upward going)

In Fig. 13 we show the distinguishability metric evaluated for the track channel and cascade channel, where the energy-dependent PID efficiency for separating the two channels is parametrized using Fig. 9, based on a full simulation and reconstruction of simulated data.

### *4.1.2. Analysis Method*

Three different independent analyses were employed in this study. Full details of the statistical methods are given in Appendix A, where we show that the approaches agree at the 5% level. The most detailed method, using a library of simulated events to generate the distribution of observables ($E_\nu$ and $\cos\theta_\nu$) expected from different possible combinations of true oscillation parameters, generates ensembles of pseudo-experiments for these scenarios and uses a likelihood ratio method to determine the degree to which one hierarchy is favored. Although this approach is currently too computationally intensive to incorporate the full range of systematics under investigation, it provides a benchmark to ensure that the statistical approximations used in the other two methods are valid.

The second analysis likewise uses the library of simulated events, and therefore incorporates all event-to-event correlations in the impact of systematics and reconstruction resolutions. It uses the so-called "Asimov" approximation instead of generating ensembles of pseudo-experiments for every possible combination of oscillation parameters [44]. This technique essentially assumes that statistical fluctuations in the experimental data are as likely to reinforce as to obscure the signature of the correct hierarchy, so that only the single most probable set of data from any given set of parameters must be analyzed. A $\chi^2$ statistic can then be calculated between the assumed true observable distribution and every alternate set of observables. The systematic factors are incorporated as nuisance parameters to be fit simultaneously, and the significance of the hierarchy is determined from the $\Delta\chi^2$ between the best fits in the subspaces corresponding to the normal and inverted hierarchies. We have verified that this "Asimov" approximation is valid by comparing the output to the full ensemble-based likelihood analysis. Because the computational demands of this statistical analysis are much smaller, the full range of systematics could be incorporated in this analysis.

The third analysis uses the simulated events to build a parametrized model of the detector response, including the analysis selection efficiency, the reconstruction resolutions and biases, and the particle identification efficiency, similar to the procedure used in [26, 41, 43]. The Fisher information matrix (the inverse of the covariance matrix), describing the effect of different systematics and of changes in the oscillation parameters, then provides a measure of the confidence with which the correct hierarchy can be determined [45]. The advantage of this method is that the analysis is not limited by the size of the available Monte Carlo event library so that statistical noise in the expectations for different sets of oscillation parameters does not impact the analysis. Although the event library corresponds to approximately 5 years of actual data, there is evidence that statistical noise in the expected distributions causes a systematic upward bias in the significances predicted by the first two analyses described. Because the significances predicted by this analysis are lower than those predicted by the others, we conservatively choose to present the results from this study as the baseline expectation for the performance of PINGU. The analysis of data from the actual detector would, of course, be based on a full likelihood analysis.

The analyses presented here have been refined in several respects from those used to generate the preliminary range of sensitivities estimated for the US High Energy Physics Community Summer Study 2013 [46]. While only preliminary estimates of analysis efficiency, and limited Monte Carlo data sets, were available for the Community Summer Study, a fully developed baseline analysis, including reconstruction and event selection,

has been developed for the baseline geometry of 40 strings and implemented in these current studies. A real particle identification algorithm to discriminate $\nu_\mu$ CC events from cascade-like events has been developed so that the effects of all flavors of neutrinos and neutral current events are now modeled in complete detail. In order to explore differences between our own estimates and those produced by some external studies, and to extend the range of systematics incorporated into our studies, we developed a parametric statistical analysis (the Fisher/Asimov analysis) similar to those used in the literature.

With the selection of a baseline geometry, the size of the Monte Carlo event library has been greatly expanded. An unforeseen interplay between statistical noise in the expected distributions of reconstructed experimental observables and the finite angular and energy resolutions of the detector can artificially enhance the apparent signature of the hierarchy (cf. Appendix A); that statistical fluctuations can systematically bias the estimate in one direction was unexpected and led to a reduction in the predicted significance of the measurement. We conservatively present estimates from the parametric (Fisher) analysis to ensure that such purely statistical effects do not affect the current estimates. This analysis also predicts a somewhat larger impact of systematic uncertainties on the final sensitivity than is seen in the analyses based on Monte Carlo pseudo-data; this difference remains under investigation, but the results given here represent the more conservative analysis. This larger impact also slows the growth of the significance below $\sqrt{t}$ scaling earlier than is predicted by the Monte Carlo event-based analyses. The net impact of all of these changes is to reduce the estimated sensitivity to the hierachy to a level comparable to, but slightly below, the conservative end of the range estimated at the time of the Community Summer Study, and in agreement with external estimates [26, 24].

### *4.1.3. Systematics and Results*

The complex neutrino oscillation pattern appearing in the PINGU detector arises from the wide range of atmospheric neutrino energies and baselines to which PINGU has sensitivity. PINGU has sufficient energy and angular resolutions to determine the NMH, and it is shown in the following that detector-related systematics do not impact the oscillation pattern in such a way as to induce a hierarchy misidentification. In addition to detector-related systematics, we categorize as a second broad class of systematics those arising from uncertainties in externally measured values of neutrino fluxes and oscillation parameters. In what follows we describe and quantify each of these systematics, and indicate possible ways to better constrain them to reduce their impact on the final significance.

The external systematics studied include uncertainties in the atmospheric neutrino flux

and spectral index, $\Delta m^2_{12}$, $\sin^2(\theta_{12})$, $\Delta m^2_{\rm atm}$, and $\sin^2(\theta_{23})$. External studies have predicted negligible dependence on $\delta_{\rm CP}$ [43], which we have verified using the full analysis of simulated event data. The most relevant detector-related systematics studied in this analysis include uncertainties in the absolute energy scale (i.e., energy calibration), a scale factor and energy-dependent shift in the effective volume, as well as uncertainties in the interaction cross-sections for both neutrinos and anti-neutrinos[3]. Some detector uncertainties are degenerate, such as the scale factors applied to the atmospheric neutrino flux, effective volume and cross-sections, and therefore in the Fisher/Asimov approach we only include one of these uncertainties. On the other hand, the flux and cross-section will be different for neutrinos and anti-neutrinos. Since the signal depends on the difference between neutrinos and anti-neutrino events, one needs to treat these two systematics separately. Although MINERvA [47] results will likely reduce the uncertainties on the relevant cross-sections substantially by the time of the PINGU data analysis, we have added a conservative (Gaussian) uncertainty of 15% on possible scale factors for neutrino and anti-neutrino cross-sections (see Fig. 14). The cross-section, the effective volume, or the flux can show an energy dependence that is not properly modeled; we include this possibility by adding an extra linear energy dependence of the effective volume, *i.e.*, $V^{\rm sys}_{\rm eff}(E_\nu) = V_{\rm eff}(E_\nu)(1 + \epsilon E_\nu)$, where $\epsilon$ is a nuisance parameter determined by the data. The list of systematic uncertainties investigated so far is extensive but not complete. For instance, the impact of uncertainties in the optical ice properties still needs to be studied although the calibration devices to be deployed as part of PINGU will reduce them considerably below their present values. Additionally , with the Fisher/Asimov technique we observe sensitivity to possible errors in the estimation of the energy and angular resolutions, but these are not yet incorporated into our systematics budget until we are able to identify physical effects that could cause misestimation of these quantities.

The effect of the systematic uncertainties on the event rates is parametrized, providing one linear (nuisance) parameter for each source. The Fisher information matrix is then evaluated including the systematic uncertainties, leading to a significance of $1.75\sigma$ with the first year of data. Figure 15 illustrates the "impact" of the individual sources of uncertainty, defined as the increase in significance seen when a particular uncertainty is disabled in the analysis. The figure also indicates that the combined effect of individual detector-specific systematic uncertainties studied so far is moderate and generally dominated by the combined physics-related systematic uncertainties. Our studies indicate that

[3]A systematic error in detector pointing (i.e., a bias in the angular reconstruction) was investigated in the Monte Carlo-based study using the Asimov approximation, but was found not to have a strong impact and was omitted from the Fisher matrix-based analysis used to obtain our sensitivity estimate.

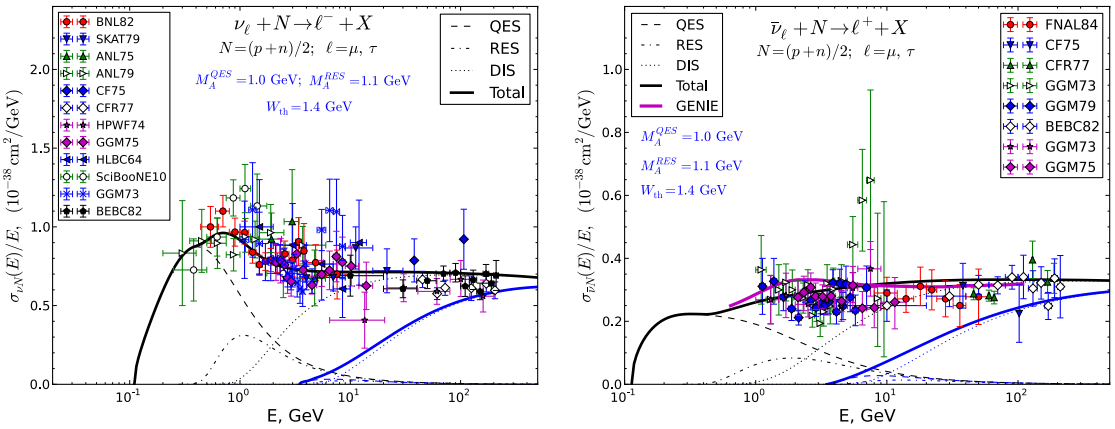


(a) Neutrino cross-sections (b) Anti-neutrino cross-sections

Figure 14: Cross-sections calculated for neutrinos (left) and anti-neutrinos (right) [48]. The thick black curve represents the $\nu_\mu$ cross-section while the blue curve represents the $\nu_\tau$ cross-section.

the measurement is limited by systematics and that the significance will grow slightly more slowly than $\sqrt{t}$ on the time scale of a few years. The resulting significance as a function of the amount of data taken by the full detector is summarized in Fig. 16, assuming $\theta_{23}$ is in the first octant. A comparison of the significance for the first vs. second octants of $\theta_{23}$ is shown in Fig. 17. It should be noted that the times indicated are slightly pessimistic, since data taking will commence prior to the completion of the full detector.

### *4.2. Conclusions*

We have developed and compared three independent Monte Carlo studies of the expected sensitivity of PINGU to the neutrino mass hierarchy. The sensitivity estimates are based on detailed simulations of the detector, and the statistical methods used were validated against a full likelihood analysis in the case of a more limited range of systematics. Our estimates also agree well with external studies [26, 24].

We find that most detector-related systematics investigated so far, with the exception of the energy calibration scale, play a smaller role than physics-related systematics. The latter arise from uncertainties in measured oscillation parameters, some of which PINGU itself will be able to measure. We also find that including non-$\nu_\mu$-CC events in the final sample with simple particle ID greatly improves the significance of the measurement.

Using the Fisher/Asimov technique with parametrizations based on fully simulated and

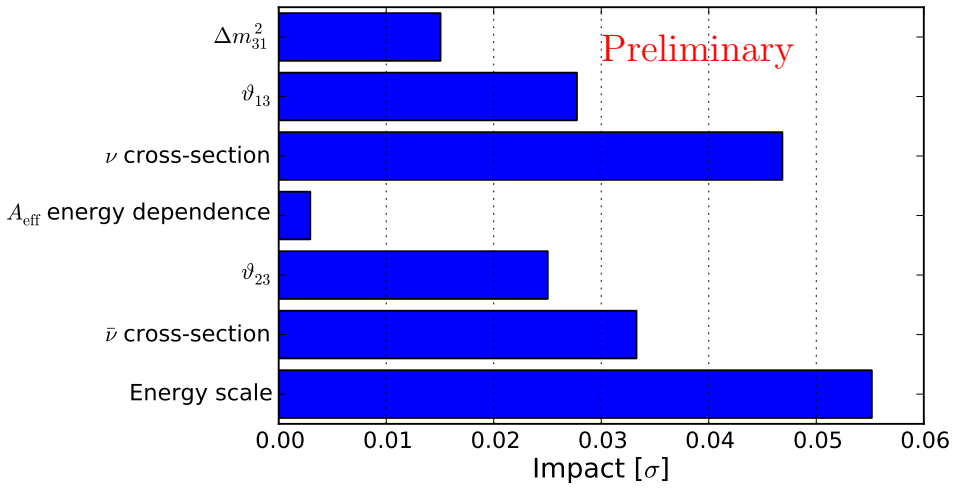


Figure 15: Summary of the systematic errors, their assumed variations, and their impacts on the estimated one-year significance of the mass hierarchy measurement. See text for details.

fully reconstructed events of all flavors, a wide array of detector- and physics-related systematics, and using a basic form of particle ID, we estimate a significance of $1.75\sigma$ with one year of data in the baseline 40-string PINGU geometry. The measurement is expected to scale nearly with $\sqrt{t}$ to significances beyond $3\sigma$, which can be achieved with slightly more than 3 years of data. We expect PINGU to be very competitive with the signficance and timescale quoted for the JUNO reactor-based experiment.

There are a number of future improvements that we believe will further improve the significance. The two most prominent involve particle ID improvements and the use of the reconstructed inelasticity of the neutrino event, which is a weak $\nu/\bar{\nu}$ discriminator. More sophisticated particle ID will enable us to better exploit the distinct patterns of $\nu_\mu$ events relative to those of $\nu_{\mathrm{e}}$ and $\nu_\tau$. The use of the inelasticity would help us distinguish neutrinos from antineutrinos on a statistical basis and could provide between a 20-50% increase in significance [33]. In addition, further geometry optimization, improved event selection efficiency and more accurate event reconstruction will also improve the significance.

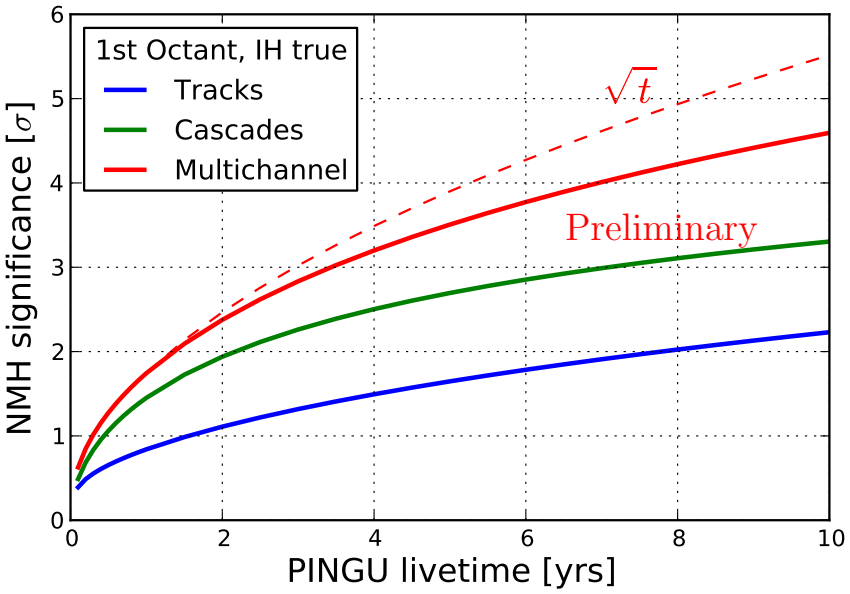


Figure 16: Significance of the neutrino mass hierarchy determination as a function of time, using the Fisher/Asimov approach and a full complement of systematics (see text for details). Note the red dashed line shows the expectation for a $\sqrt{t}$ dependence.

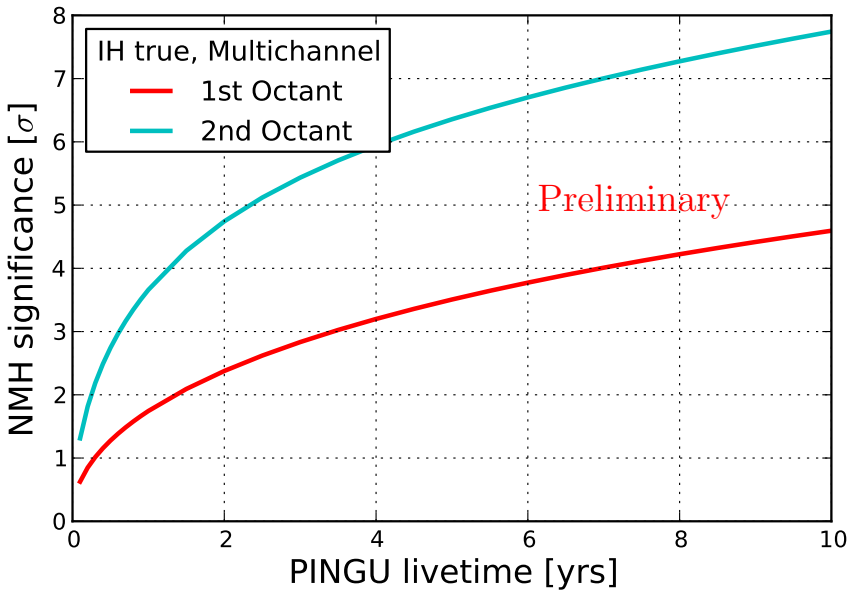


Figure 17: Signficance of the neutrino mass hierarchy determination as a function of time for the first octant compared to the second octant using the Fisher/Asimov approach, multichannel events, and a full complement of systematics (see text for details). The lower first octant line in the plot is the same as the upper multichannel line in Fig. 16.

## 5. Muon Neutrino Disappearance

The recent atmospheric oscillation analysis by IceCube's DeepCore [3] demonstrated the detector's ability to extract neutrino oscillation parameters. This measurement focuses on resolving the first minimum in the $\nu_\mu$ survival probability for vertically upward-going $\nu_\mu$ at roughly 25 GeV. Here we discuss how PINGU can improve this measurement. While intrinsically interesting, this measurement is also relevant for the determination of the NMH because the current uncertainties in the atmospheric oscillation parameters $\Delta m^2_{32}$ and $\sin^2(\theta_{23})$ are considered for the NMH measurement.

### *5.1. Event Selection and Reconstruction*

The analysis considers the PINGU 20-string geometry with a realistic event selection based on the latest DeepCore $\nu_\mu$ disappearance analyses [4]. The event selection is very stringent and includes veto cuts against atmospheric muons from air showers (using the outer string layers of IceCube as a veto), cuts on the reconstructed direction of neutrino-induced muons (selecting upward-going events), cuts on the containment of events inside PINGU and quality cuts commonly used in other IceCube analyses. We ensure that the background of atmospheric muons is adequately rejected by including the outer DeepCore strings to the veto cuts. The corresponding efficiency for signal (upward-going $\nu_\mu$ CC events contained inside PINGU) is calculated by applying these cuts to $\nu_\mu$ and $\nu_\mathrm{e}$ simulations. These simulations are based on an older version of the IceCube Monte Carlo software where the calculation of the hadronic light yield below 10 GeV was incorrect. The background of cascade events is therefore overestimated, which makes this analysis conservative. We expect approximately 22,000 upward-going $\nu_\mu$ events per year, taking three-flavor oscillations and matter effects into account, where the maximum rate (dN/dE) is expected between 5–10 GeV. For all events, the reconstructed interaction vertex is required to lie inside the fiducial volume of PINGU, defined here as a right circular cylinder of radius 80 m and height 290 m located at the bottom center of IceCube.

In order to measure atmospheric neutrino oscillations we reconstruct the neutrino zenith angle, which is an estimator of the propagation length of the neutrino through the Earth, and the neutrino energy. The latter is estimated by a linear combination of the reconstructed energy of the hadronic cascade ($E^\mathrm{reco}_\mathrm{had}$) from the neutrino interaction and the reconstructed track length of the muon ($L^\mathrm{reco}_\mu$), converted into an energy by assuming the energy loss of a MIP, given by

$$E^\mathrm{reco}_\nu = E^\mathrm{reco}_\mathrm{had} + L^\mathrm{reco}_\mu / 4.5\,\mathrm{mGeV}^{-1}. \quad (2)$$

The hadronic cascade energy and the neutrino zenith angle are reconstructed using simpler and less accurate reconstruction algorithms than those described in section 2.4. The zenith angle algorithm searches for hyperbolic time patterns on individual strings and represents a stringent event cleaning and discarding almost 50 % of the upward-going charged-current $\nu_\mu$ events in the final event sample. Instead of removing those events from the sample, the neutrino zenith angle of those events is reconstructed with a maximum-likelihood approach based on the multi-photoelectron (MPE) likelihood [49]. The neutrino zenith angle is reconstructed with a median resolution of 20° and the energy resolution ($|E_\nu - E_\nu^{\mathrm{reco}}|/E_\nu$) is approximately 35 % in the energy range of 1–20 GeV using this method.

### *5.2. Likelihood analysis*

A data challenge was performed in order to determine how precisely PINGU would measure the oscillation parameters $\Delta m^2_{32}$ and $\sin^2(\theta_{23})$, given certain systematics. Two-dimensional histograms of $\cos(\theta_\nu^{\mathrm{reco}})$ versus $\log(\mathrm{E}_\nu^{\mathrm{reco}})$ are compared in a binned two-dimensional likelihood-ratio test for experiment-like data with a set of Monte Carlo data (consisting of $\nu_\mu$ and $\nu_\mathrm{e}$ events) re-weighted with different values for $\Delta m^2_{32}$ and $\sin^2(\theta_{23})$. The experiment-like histogram is created from the same Monte Carlo data using bin-by-bin Poisson statistical fluctuations and taking the world best fit values for all oscillation parameters as input parameters [42].

Figure 18 shows the mean of 1,000 scans over $\Delta m^2_{32}$ and $\sin^2(\theta_{23})$. At each scan point, the atmospheric neutrino flux normalizations ($c_{e/\mu}$ for $\nu_\mathrm{e}$ and $\nu_\mu$) and the mixing angle $\theta_{13}$ are adjusted such that the likelihood expression given by

$$\mathcal{L} = \prod_{i,j} \mathcal{L}_{\mathrm{Poisson}}\left(s_{ij}|\{\Delta m^2_{32}, \sin^2(\theta_{23})\}, \{q_k\}\right) \cdot \frac{1}{\sqrt{2\pi}\sigma_{\theta_{13}}} \exp\left(-(\theta_{13} - \hat{\theta}_{13})^2/2\sigma^2_{\theta_{13}}\right), \quad (3)$$

is maximal. Here, $s_{ij}$ is the number of events in bin $(i, j)$, and $\{q_k\} = \{c_e, c_\mu, \theta_{13}\}$ the nuisance parameters. A Gaussian penalty term is incorporated in Eq. (3) for $\theta_{13}$ according to its world best fit value. All remaining oscillation parameters are fixed to the world best fit values. The true values for $\Delta m^2_{32}$ and $\sin^2(\theta_{23})$ are reproduced within the uncertainties of the fit. Here, maximal mixing ($\theta_{23} = 45°$) can be excluded at the 68 % confidence level with one year of PINGU data. For 17 % of the pseudo-experiments, the minimum negative log-likelihood value lies in the region of the opposite octant of $\theta_{23}$ and for 4 % of the pseudo-experiments in the region of the opposite sign of $\Delta m^2_{32}$.

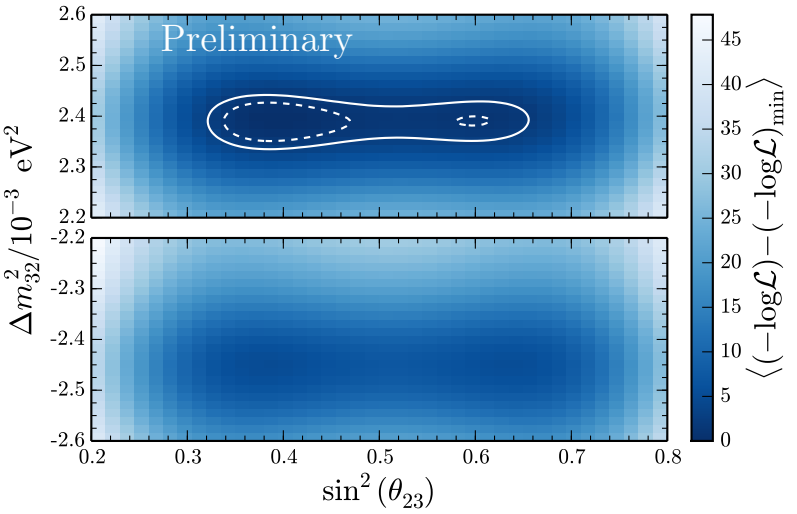


(a) Normal neutrino mass hierarchy assumed.

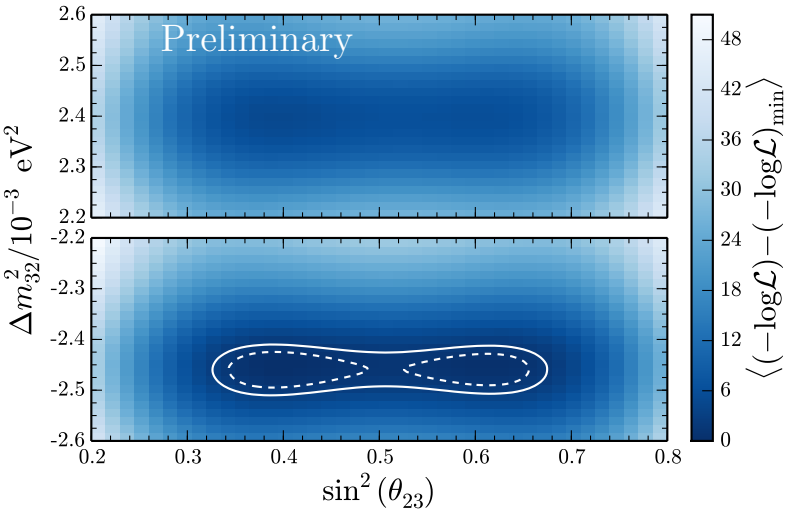


(b) Inverted neutrino mass hierarchy assumed.

Figure 18: Mean of 1,000 likelihood scans over $\Delta m^2_{32}$ and $\sin^2(\theta_{23})$ with one year of PINGU data. The inner and outer white curve show the 68 % and 90 % contours, respectively.

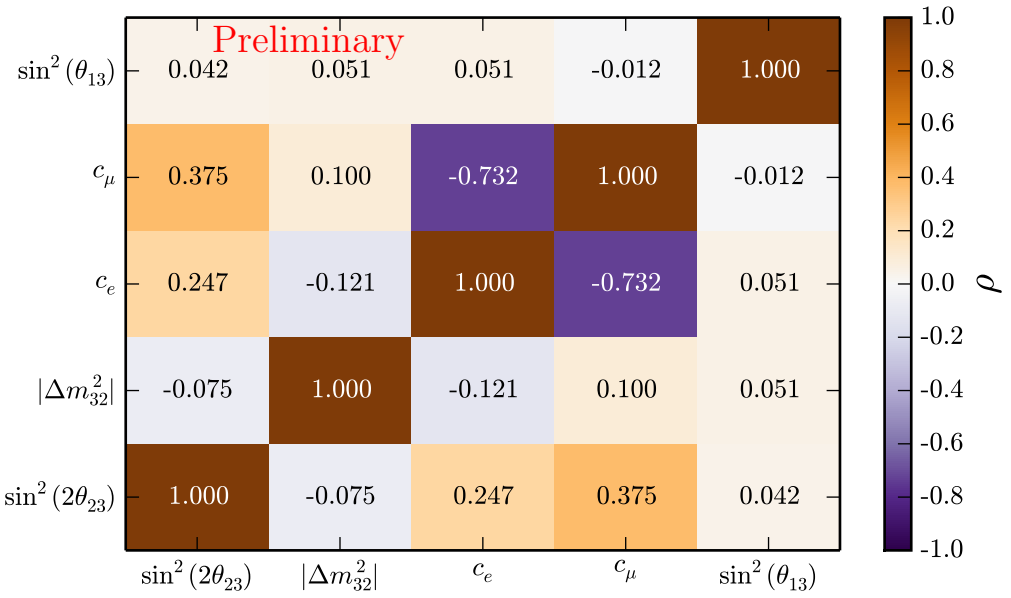


Figure 19: Illustration of the correlation coefficient $\rho$ between the best fit values for $\sin^2(2\theta_{23})$, $|\Delta m^2_{32}|$, $c_e$, $c_\mu$ and $\sin^2(\theta_{13})$.

### *5.3. Systematic uncertainties*

We consider systematic uncertainties due to the normalizations of the atmospheric electron and muon neutrino fluxes and uncertainties in the oscillation parameters measured by other experiments. We identified $\theta_{13}$ as the oscillation parameter which has the largest impact on the measurement while $\Delta m^2_{21}$ and $\theta_{12}$ only cause a significant change in the oscillation pattern below the energy threshold of PINGU (a few GeV). The influence of the $\delta_{\mathrm{CP}}$ has not yet been investigated.

Figure 19 shows the correlation between the best fit values for $\sin^2(2\theta_{23})$, $|\Delta m^2_{32}|$, $c_e$, $c_\mu$ and $\sin^2(\theta_{13})$. While $\sin^2(2\theta_{23})$ and $c_\mu$ are strongly correlated (correlation factor of $\rho = 0.375$), $\sin^2(\theta_{13})$ has only a small influence on the measurement of $\Delta m^2_{32}$. Matter effects in the Earth, which are driven by $\theta_{13}$, affect the position of the first oscillation minimum only marginally. The strong correlation between the flux normalization and the atmospheric mixing angle implies that the measurement of $\theta_{23}$ could be significantly improved with better constraints on the atmospheric fluxes. One possible approach to achieve this would

be to remove any angular cuts in the event selection to retain downward-going $\nu_\mu$, which do not oscillate, and use them to provide a flux normalization. Such an event selection would have to rely primarily on veto information (with outer DeepCore strings providing additional veto power) to reject the background of atmospheric muons.

### *5.4. Comparison to other Measurements*

Figure 20 shows the predicted 90 % confidence region associated with one year of PINGU data compared to recent results from MINOS [50] and T2K [51]. Predicted sensitivities for MINOS and MINOS+ through 2016 reach $\pm 5\%$ for $\sin^2(2\theta_{23})$ and $\pm 2.7\%$ for $\Delta m^2_{32}$.[4] Predicted sensitivities for T2K reach $\pm 10\%$ for $\sin^2(\theta_{23})$ and $\pm 1.7\%$ for $\Delta m^2_{32}$ with $7.8 \times 10^{21}$ protons on target (POT).[5] After the first year of data taking PINGU would be competitive and has the potential to set improved constraints on the atmospheric neutrino oscillation parameters, provided the systematic uncertainties can be adequately controlled. In particular, detector-related and ice property uncertainties, which were not considered in the analysis presented here, may play an important role. Moreover, the underlying MC statistics considered represent only one year of PINGU data and may affect the obtained results. In contrast to MINOS, the oscillation parameters $\Delta m^2_{32}$ and $\sin^2(\theta_{23})$ would be uncorrelated in the PINGU measurement. PINGU is able to cover the whole range of the first minimum in the $\nu_\mu$ survival probability at 25 GeV (for vertically upward-going neutrinos), including the rising edge toward lower energies, leading to strong constraints on $\Delta m^2_{32}$.

### *5.5. Conclusions*

PINGU's dense instrumentation and the resulting low energy threshold allow precision measurements of atmospheric neutrino oscillations with at least twice as much statistical accuracy as current DeepCore oscillation analyses. PINGU would be able to resolve the first minimum in the $\nu_\mu$ survival probability at 25 GeV (for vertically upward-going events) with a high accuracy. This leads to strong constraints on $\Delta m^2_{32}$ and $\sin^2(\theta_{23})$. PINGU is expected to be capable of improving recent results from MINOS and T2K and could provide competitive constraints on the atmospheric oscillations parameters with its first year of data.

[4] K. Lang and J. Thomas, personal communication.
[5] M. Friend, presentation at 17th J-PARC PAC.

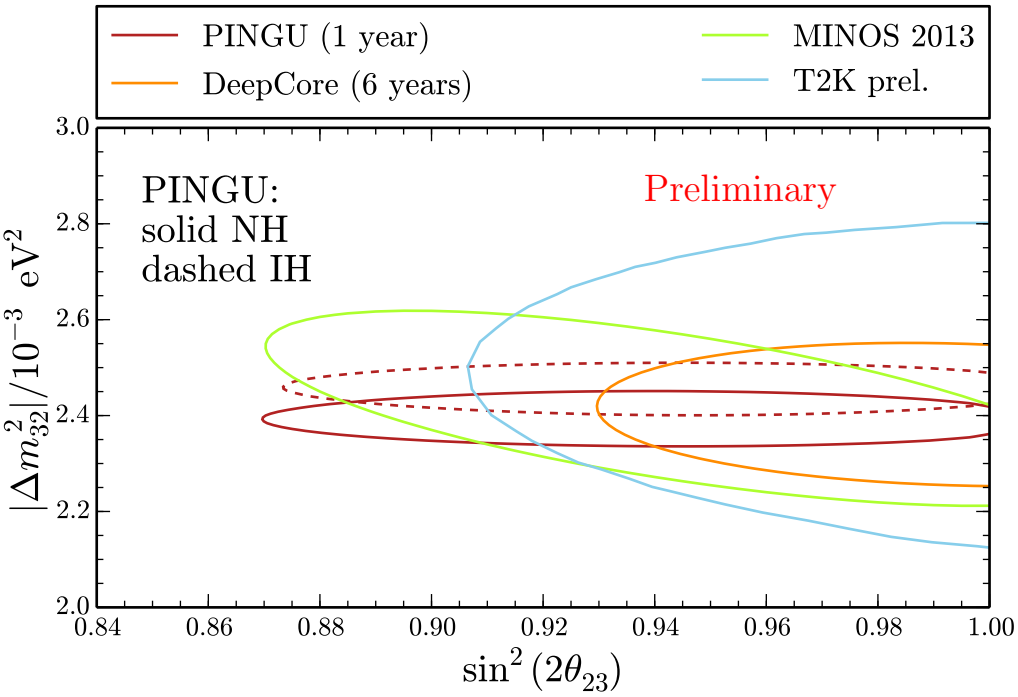


Figure 20: Comparison of expected PINGU confidence regions with one year of data to recent results from MINOS [50] and T2K [51] and to the expected DeepCore confidence regions with six years of data [52]. Note the vertical shift observed in the contours is due to the use of $\Delta m^2_{32}$ rather than $\Delta m^2_{atm}$.

The determination of the neutrino mass hierarchy (as described in section 4) involves a $\chi^2$/likelihood scan over $\Delta m^2_{32}$ and $\sin^2(\theta_{23})$, extended to negative values of $\Delta m^2_{32}$, and therefore depends on the precision at which these parameters can be measured. The sensitivity of PINGU to atmospheric oscillations, as demonstrated in this section, reduces the uncertainties in the associated oscillation parameters, independent of other measurements.

## 6. Sensitivity to Non-Maximal $\theta_{23}$ Mixing

In the following, we present a preliminary estimate of the potential of PINGU data to establish a deviation in $\theta_{23}$ from maximality, and to determine the $\theta_{23}$ octant. Although this analysis does not include the range of detector-related systematics included in the studies of the sensitivity to the mass hierarchy, it provides an initial measure of the potential reach of PINGU data to investigate these questions.

### *6.1. Analysis*

#### *6.1.1. Simulation Event Selection and Reconstruction*

For this analysis we use up-going events occurring within 100 m radially from the center of the IceCube detector and with vertical coordinate -100 m > z > -500 m. Experimental resolution effects are approximated by smearing the zenith angle ($\theta_z$) and neutrino energy ($E$) of each event by a Gaussian with $\sigma_E = 2.5$ GeV and $\sigma_{\theta_z} = 8.5°$. Although this parametrization does not account for the energy dependence of the experimental resolutions, the actual resolutions shown in Sec. 2 are better than these values over much of the energy range relevant for this measurement.

#### *6.1.2. Method*

The $\nu_\mu \to \nu_\mu$ oscillation probability depends strongly on neutrino energy in the region of interest (3–40 GeV). For this analysis the reconstructed track length serves as our energy proxy. Each point in the atmospheric oscillation parameter space $(\theta_{23}, \Delta m^2_{\rm atm})$ is associated with a unique muon neutrino event distribution $\mathcal{D}$. Repeated measurements of this distribution would yield experimental distributions $d_i$. To estimate PINGU's ability to discriminate in this space we adopt and extend the method of maximum likelihood outlined in Sec. 4 and Appendix A. The crucial difference here is that rather than applying the method to only two hypotheses, we apply the method to a grid of points in the $(\theta_{23}, \Delta m^2_{\rm atm})$ space, using a particular combination of parameters $p_1 = ((\theta_{23})_1, (\Delta m^2_{\rm atm})_1)$, associated with an event distribution $\mathcal{D}_1$, as a reference point. A second point $p_2 = ((\theta_{23})_2, (\Delta m^2_{\rm atm})_2)$, associated with a distribution $\mathcal{D}_2$, is then tested against $p_1$ to determine the significance at which a measurement of $p_2$ can exclude $p_1$ using the test statistic

$$\mathrm{LLR}_i = \ln\left(\frac{\mathcal{L}(d_i|\mathcal{D}_1)}{\mathcal{L}(d_i|\mathcal{D}_2)}\right), \tag{4}$$

with $\mathcal{L}$ being the likelihood function and $\mathrm{LLR}_i$ the natural logarithm of the ratio of likelihood functions. By varying $p_2$ in the parameter space around $p_1$, contours of constant significance are mapped out around the reference point.

### *6.2. Results*

#### *6.2.1. Sensitivity to Non-Maximal Mixing*

The test described above is first applied in the $(\theta_{23}, \Delta m^2_{\mathrm{atm}})$ parameter space while keeping all other mixing parameters fixed at their global best values (see Table 3). We present here contours of constant significance in this space about given reference points (e.g., the point of maximal $\theta_{23}$ mixing may be compared to the neighboring space). The contours should be interpreted as follows: the n$\sigma$ contour about a reference point is the ensemble of points in the parameter space for which, if these were the best fit to PINGU data, we could exclude that reference point at n$\sigma$, assuming all other parameters were held constant. If the experimental best fit was at any point outside the contour, we could thus exclude the reference point at greater than n$\sigma$.

Figures 21 and 22 show the separation potentially achievable in 5 years between the current global best fit and maximal $\theta_{23}$ mixing under both mass hierarchies and assuming different $\theta_{23}$ octants, before accounting for systematic uncertainties. We find that a separation of better than $5\sigma$ is potentially achievable within this time frame, regardless of the true $\theta_{23}$ octant and the true mass hierarchy.

PINGU's potential sensitivity in this sector also compares well to the projected sensitivities of other experiments (see Fig. 23 for a comparison with NOvA and T2K).

#### *6.2.2. Sensitivity to the $\theta_{23}$ Octant*

PINGU's potential to distinguish $\theta_{23}$ octants in the case of non-maximal mixing is also investigated. We find this to be highly dependent on the true mass hierarchy and true $\theta_{23}$ octant (compare Figs. 21 and 22). Assuming the true oscillation parameters are $\theta_{23}$ at its global best fit value for the 1st octant (i.e. $\theta_{23} = 40.0°$) and normal mass hierarchy, PINGU may exclude the entire second octant at significances greater than $5\sigma$ (Fig. 21(a)). If the true value of $\theta_{23}$ is at the current global best fit for the second octant (i.e. $\theta_{23} = 50.4°$), then PINGU may exclude the entire first octant after five years by $3\sigma$ for a normal mass hierarchy, or by $1\sigma$ for an inverted mass hierarchy (Fig. 22).

| Oscillation Parameter | Global Best Fit $\pm$ $1\sigma$ | $3\sigma$ range |
|---|---|---|
| $\theta_{12}/^\circ$ | $33.36^{+0.81}_{-0.78}$ | $31.09 \rightarrow 35.89$ |
| $\theta_{23}/^\circ$ | $40.0^{+2.1}_{-1.5} \oplus 50.4^{+1.3}_{-1.3}$ | $35.8 \rightarrow 54.8$ |
| $\theta_{13}/^\circ$ | $8.66^{+0.44}_{-0.46}$ | $7.19 \rightarrow 9.96$ |
| $\delta_{CP}/^\circ$ | $300^{+66}_{-138}$ | $0 \rightarrow 360$ |
| $\frac{\Delta m^2_{21}}{10^{-5}eV^2}$ | $7.50^{+0.18}_{-0.19}$ | $7.00 \rightarrow 8.09$ |
| $\frac{\Delta m^2_{31}}{10^{-3}eV^2}$(NH) | $2.473^{+0.070}_{-0.067}$ | $+2.276 \rightarrow +2.695$ |
| $\frac{\Delta m^2_{32}}{10^{-3}eV^2}$(IH) | $-2.427^{+0.042}_{-0.065}$ | -2.649 $\rightarrow$ -2.242 |

Table 3: Global best fit values for three flavour neutrino oscillations, as used in the analysis of this section. Note that the global best fit for $\theta_{23}$ is given for both the first and second octants [53].

### *6.3. Parameter Degeneracies*

#### *6.3.1. Experimental Uncertainties in $\theta_{23}$ and $\Delta m^2_{\rm atm}$*

As an initial investigation of parameter degeneracy we allow $\theta_{23}$ to vary within a range of $\pm 1\sigma$ of the global best fit while testing the ability to rule out with the maximal $\theta_{23}$ mixing point. At the extrema of this range we find minimum significances of $3\sigma$ (NH) and $1.5\sigma$ (IH). As expected, the further the true value of $\theta_{23}$ deviates from maximal mixing ($45^\circ$) the higher the significance found. Variance of the $\Delta m^2_{\rm atm}$ parameter is found to result in a vertical translation of contours (i.e., shifts along the $\Delta m^2_{\rm atm}$ axis in Fig. 21), with significances between mixing angles along lines of constant $\Delta m^2_{\rm atm}$ remaining roughly the same.

#### *6.3.2. Correlations with other Mixing Parameters*

Degeneracy effects are then extended to the remaining neutrino mixing parameters by varying one parameter at a time from its global best fit. This amounts to expanding the above method to a three-dimensional parameter space (e.g., the $(\theta_{23}, \Delta m^2_{\rm atm}, \delta_{\rm cp})$ space) in which we have in effect already explored a plane (e.g., the $\delta_{\rm cp} = 300^\circ$ plane).

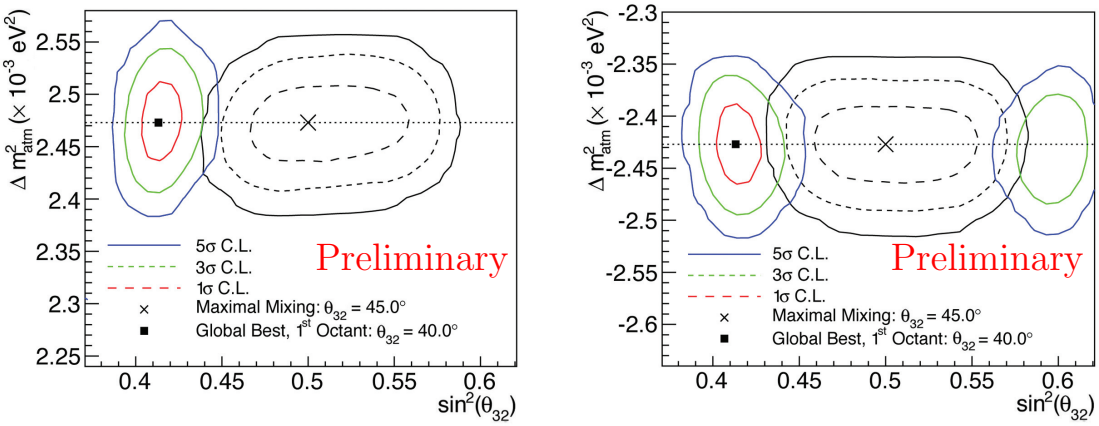


(a) Normal Mass Hierarchy

(b) Inverted Mass Hierarchy

Figure 21: Atmospheric oscillation parameter space constraints under normal (left) and inverted (right) mass hierarchy expected from five years of PINGU data. Significance contours are shown about two reference points: the global best fit in the first octant (filled squares) and maximal $\theta_{23}$ mixing (crosses). For conciseness, contours of constant significance about each point are drawn together (colorscale for global best, dashed lines for maximal mixing). We find the significance of each of the above reference points with respect to the other exceeds $5\sigma$. Octant discrimination is much stronger for a normal mass hierarchy than for an inverted one, with the entire second octant excluded at more than $5\sigma$. Note the appearance of a second set of contours in (b) in the second octant, indicating PINGU's inability to distinguish octants under inverted mass hierarchy beyond $3\sigma$.

Variations in $\theta_{12}$ or $\Delta m^2_{12}$ over a $\pm 3\sigma$ range are found to have almost no impact on the significance between fixed $(\theta_{23}, \Delta m^2_{\text{atm}})$ values. We find that the significances obtained above (Figs. 21 and 22) are most sensitive to changes in the parameters $\theta_{13}$ and $\delta_{\text{cp}}$ (see Fig. 24). Although this study does not take into account the effect of uncertainties on multiple parameters simultaneously, these initial results suggest that the systematic uncertainties investigated so far will not have drastic effects on PINGU tests of maximality.

### *6.4. Summary*

We have applied a maximum likelihood method to perform hypothesis testing in the atmospheric neutrino oscillation parameter space. Using current global best fit values for oscillation parameters, we find that PINGU has the potential to exclude the case of maximal mixing at more than $5\sigma$, independent of true mass hierarchy, although the impact of detector-related systematics and of more realistic models of the detector response have yet to be assessed. In the case of normal mass hierarchy, PINGU may also distinguish

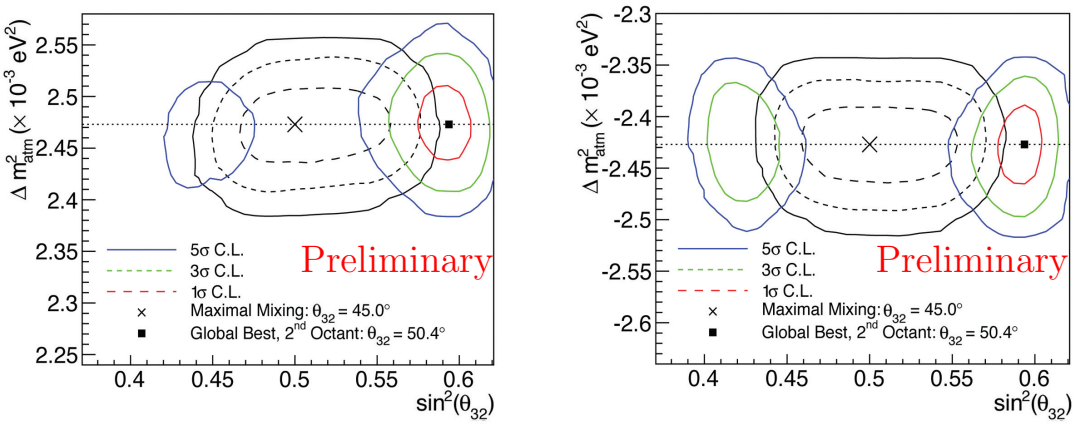


(a) Normal Mass Hierarchy

(b) Inverted Mass Hierarchy

Figure 22: Same as Fig. 21 but with the second $\theta_{23}$ octant global best fit value used for the non-maximal mixing reference point (filled squares). For an inverted mass hierarchy, octant discrimination is similar to the true first octant case. For a normal mass hierarchy, octant discrimination is weaker than when $\theta_{23}$ lies in the first octant.

the correct $\theta_{23}$ octant by more than $5\sigma$ if the true value of $\theta_{23}$ lies in the second octant, or by more than $3\sigma$ if the true value lies in the first octant. This analysis is now being refined to include full event reconstructions and systematic uncertainties.

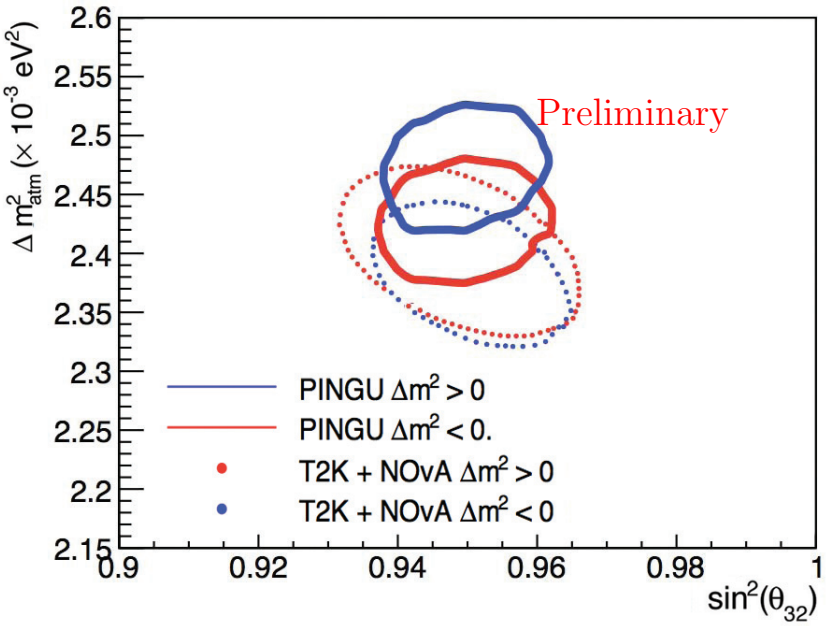


Figure 23: Comparison of potential 90% confidence intervals for normal (blue) and inverted (red) mass hierarchies for PINGU (solid line) and T2K and NOvA (dashed line) experiments. Contours for T2K+NOvA were generated assuming the following: global best fit of $\sin^2(2\theta_{23}) = 0.95$ ($\theta_{23} = 38.54°$), $\Delta m^2_{31} = 0.0024$ for both hierarchies, $\nu$:$\bar{\nu}$ ratio of 1:4 with 7.8e21 protons on target (POT) for T2K and 3.6e21 POT for NOvA; T2K is expected to reach this POT level by 2020 ([54]). Contours for PINGU do not yet include systematic uncertainties and assume 5 years of data taking using global best fit of $\sin^2(2\theta_{23}) = 0.949$ ($\theta_{23} = 38.5°$), $\Delta m^2_{31} = 0.002473$ (NH), and $\Delta m^2_{32} = -0.002427$ (IH).

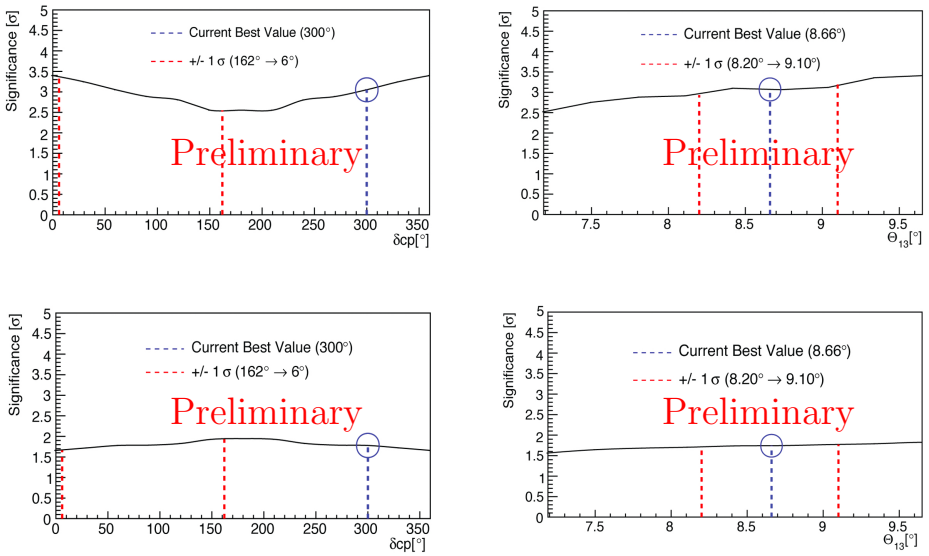


(a) $\delta_{\mathrm{cp}}$ (b) $\theta_{13}$

Figure 24: Dependence of significance with which two points in $(\theta_{23}, \Delta m^2_{\mathrm{atm}})$ space can be distinguished on uncertainties in $\delta_{\mathrm{cp}}$ (left) and $\theta_{13}$ (right) for a normal mass hierarchy (NH; top) and an inverted mass hierarchy (IH; bottom). As in previous figures, the significance is between the global best fit point $(\theta_{23}, \Delta m^2_{\mathrm{atm}}) = (42.1°, 2.473{\times}10^{-3}\mathrm{eV}^2)$ and maximal mixing at $(\theta_{23}, \Delta m^2_{\mathrm{atm}}) = (45.0°, 2.473{\times}10^{-3}\mathrm{eV}^2)$ and assumes five years of PINGU data. In each panel, the identified mixing parameter was varied over a $\pm 3\sigma$ range.

## 7. Neutrino Tomography

### *7.1. Motivation*

Seismological data based on primary (compressional) p-waves and secondary (shear) s-waves have been used in the construction of the preliminary reference Earth model (PREM) that describes the Earth matter density profile. While the matter density is well known through these measurements, the chemical composition of the Earth has not yet been measured. Neutrino tomography provides the first and possibly the only way to measure directly the Earth's composition. By exploiting the dependence of neutrino oscillation probabilities on the electron density, PINGU with its large atmospheric neutrino sample could be the first experiment to be able to use neutrino tomography to distinguish between proposed Earth core composition models. Systematic uncertainties associated with the unknown true values of oscillation parameters are reduced by the observation of oscillating neutrinos that do not cross through the Earth's core.

### *7.2. Introduction and Earth Composition Models*

The Earth's geomagnetic field was discovered at the end of 16th century [55], and since then many models have been proposed to explain its origin. The dynamo model is the leading model to explain the field, and it implies that the Earth contains a conducting fluid and is convecting [56]. If the composition of the interior of the Earth could be measured it may help resolve the longstanding mystery of the origin of the geomagnetic field and further advance our understanding of the Earth.

Direct sampling of the Earth interior is limited by the reach of drills, which have only penetrated down to a depth of about 12 km [57]. Coarse information about deeper regions of the Earth can be obtained by eruption entrainment sampling [58], and the interior of the Earth has mainly been studied using seismic waves.

The inner Earth consists of two distinct parts: silicate Earth and the core (see Fig. 10 for a schematic view). The silicate Earth consists of the crust and lower and upper mantles. The core is divided into outer and inner regions. Boundaries between these layers are relatively precisely known and uncertainties on their positions are smaller than 10 km [59]. The outer core was found to be liquid from the absence of detected s-waves [60]. The PREM matter density structure was developed by combining astronomic-geodetic parameters, free oscillation frequencies, and seismic wave velocity [40]. The uncertainty

on the average density of the lower mantle is estimated to less than 0.7% [61], and of the inner core as less than 0.5% [62].

It is believed that the bulk chemical composition of the Earth is the same as the composition of the "Ivuna" type carbonaceous chondritic meteorites (CI) [63]. The crust and upper mantle contains less iron, nickel, and sulfur than CI chondrites, therefore, the core region should contain more iron and nickel. By comparing high pressure experimental data and seismological velocity profiles, the inner and outer core is presumed to be mostly made of iron with some additional light elements [64].

The convection of the outer core is assumed to be a combination of thermal and compositional convection. Without the compositional convection, it is difficult to maintain the geo-dynamo [65]. Measuring the composition of the Earth's core is therefore expected to lead to the understanding of the geo-dynamo model. In addition, scenarios of the Earth formation depend on Earth core composition models [66].

There is little doubt in the interpretation of the outer core as liquid iron alloyed with nickel and some light elements, but the content and type of light elements are still uncertain because of limitations of the observational data. From high-pressure experimental constraints, possible candidates for the light elements are hydrogen, carbon, oxygen, silicon, and sulfur [67]. Hydrogen is the least understood candidate regarding chemical composition of the Earth, but liquid iron alloyed with 1% hydrogen by weight could also explain the outer core density [68].

### *7.3. Methodology*

The Earth composition measurement with PINGU is made feasible by the fact that neutrino oscillations depend on the electron density $N_e$. The electron density is related to the mass density via the factor $Y = Z/A$, weighted by the relative elemental abundances. As an example iron has a value of $Y = 0.466$, while lighter elements have values closer to $Y = 0.5$, and hydrogen a very distinctive value of $Y = 1.0$.

The effect of the core composition (or changed electron density) is illustrated in Fig. 25. The effect is evident in the up-going neutrino events that cross the inner or outer core, corresponding to zenith angles greater (smaller) than $\theta_\nu = 168^\circ$ ($\cos\theta_\nu = -0.98$) and $\theta_\nu = 147$ ($\cos\theta_\nu = -0.84$), respectively. The most relevant energy range is between about 2 GeV and 6 GeV. Good energy resolution in this energy range is essential for the success of a neutrino tomography measurement.

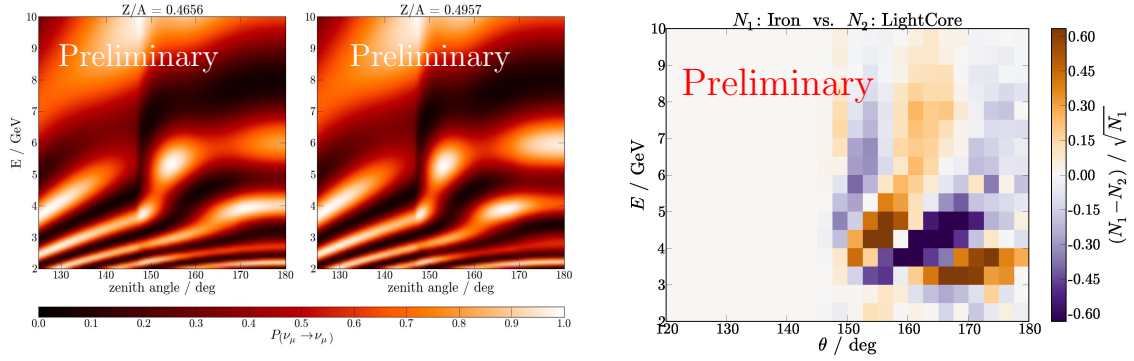


Figure 25: The impact of a changed core composition on the muon-neutrino survival probabilities is demonstrated by comparing the left most figure (pure iron core) and the middle figure (iron mixed with lighter elements). Signature of a pure iron Earth core with respect to a model assuming the same composition for mantle and core are shown on the right. The true neutrino energy and direction are shown for one year of data with 35% electron neutrino contamination.

### *7.4. Analysis Method*

The tomography analysis presented here uses the 40-string PINGU baseline geometry. A realistic event sample is based on the latest IceCube and DeepCore oscillation analyses [4]. This yields a sample of starting events with the interaction vertex inside the fiducial volume of PINGU. We expect approximately 33000 upward-going muon neutrinos per year, with roughly 50% coming from the energy region between 2 GeV and 6 GeV.

The neutrino energy and zenith angle are reconstructed using the deposited charge and track length to fit the cascade and muon, respectively. The neutrino is reconstructed with a median energy resolution of $\sigma_{\mathrm{E}_\nu} \approx 0.33\, E_\nu$ and median zenith angle resolution of 15° for muon neutrino charged-current events between 2 GeV and 6 GeV. (Future work will use the better-performing reconstruction presented in Sec. 2.)

For the sensitivity calculation, a likelihood ratio test as described in Appendix A is performed for different core composition models. The data are binned in $\log_{10}(\mathrm{E/GeV})$ and zenith angle $\theta_\nu$. For $\theta_\nu > 146°$, neutrinos cross the Earth's core. For each bin, the likelihood for a given core composition is calculated. Systematic uncertainties are treated as nuisance parameters in the fitting procedure. These uncertainties include the atmospheric neutrino flux normalizations and the neutrino oscillation parameters $\Delta m^2_{\mathrm{atm}}$, $\theta_{23}$, and $\theta_{13}$. Values far from the world best fit values [42] are penalized using Gaussian

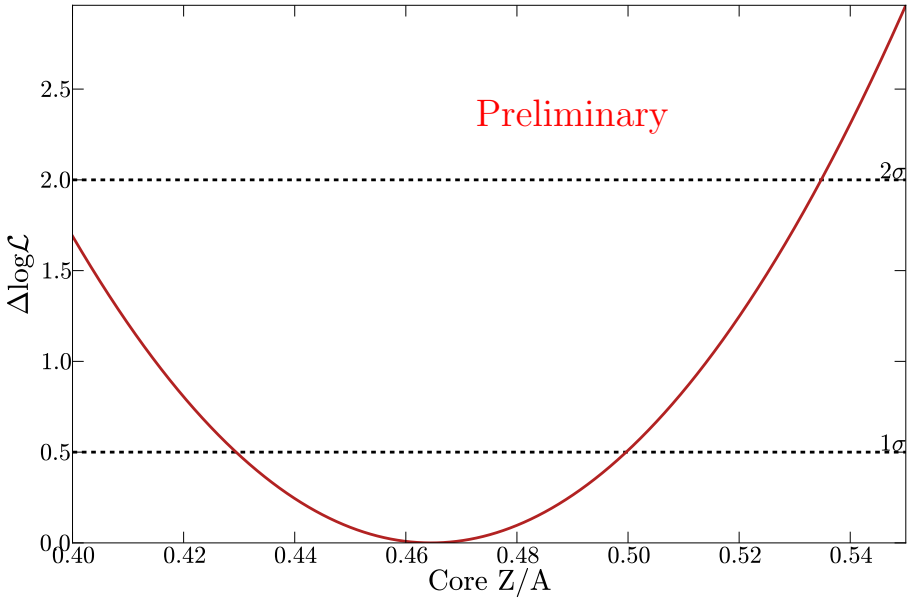


Figure 26: Mean of 1000 likelihood scans over proton to nucleon ratio Z/A of the inner and outer Earth core with 5 years of PINGU data. The input value assuming a pure iron Earth core is reproduced correctly. In addition, the input can be reconstructed with an accuracy of eight percent at $1\sigma$-level.

priors. The total likelihood is then calculated as

$$\mathcal{L} = \prod_{i,j} \mathcal{L}_{\text{Poisson}}\left(x_{ij} \mid \{\zeta_k\}, \{\xi_l\}\right) \cdot \prod_{\xi \in \{\xi_l\}} \frac{1}{\sqrt{2\pi}\sigma_\xi} \exp\left(-\left(\xi - \xi_0\right)^2 / 2\sigma_\xi^2\right) \ , \tag{5}$$

where $x_{ij}$ is the number of events in bin $(i, j)$, $\{\zeta_k = \text{Z/A}|_k \mid k \in \{\text{Mantle, Core}\}\}$ are the physics parameters, and $\{\xi_l\}$ are the nuisance parameters. Neutrinos at energies greater than 10 GeV that do not cross the Earth's core can be used to further constrain theoretical systematics.

A scan over the parameter space of electron densities, *i.e.,* the proton to nucleon ratio $Z/A$, can be seen in Fig. 26. For each point, the nuisance parameters $\Delta m^2_{\text{atm}}$, $\theta_{23}$, $\theta_{13}$, and flux normalizations have been adjusted so that the likelihood in Eq. 5 is maximal. The input values ($Z/A = 0.4656$ for the inner and outer Earth core) are reproduced correctly with an accuracy of $\pm 8\%$ ($\pm 1\sigma$) on $Z/A$ after five years.

Figure 27 (left) shows the exclusion level vs. time for a pure iron core ($Z/A = 0.4656$) relative to a mantle-like pyrolite core ($Z/A = 0.4957$). These models can be distinguished with more than 68% confidence within five years assuming normal neutrino mass hierarchy. Figure 27 (right) shows that this corresponds to an accuracy of 8% using a pure iron Earth core as baseline.

We also show the model comparison of pyrolite with respect to iron, where the values of $\theta_{13}$ have been shifted by $1\sigma$ from the current best fit values. The accuracy in $\theta_{13}$ is expected to increase, so our shift overestimates this systematic effect.

A more crucial systematic than the value $\theta_{13}$ is the neutrino mass hierarchy. If the hierarchy is inverted, the possibility to exclude one model with respect to another drops by 50%. Under the normal hierarchy, resonant matter oscillations due to the MSW-effect [6, 7] occur only for neutrinos; under the inverted hierarchy, they occur only for antineutrinos. In the energy range of interest, the cross section for the interaction of neutrinos with matter is roughly twice of that of antineutrinos [69]. This decreases the relative number of signal events in the inverted hierarchy case, leading to a drop in significance. Under the inverted hierarchy, the two Earth models—iron and pyrolite—can be distinguished by no more than $0.4\sigma$ in 10 years. Assuming the wrong hierarchy for the llh-scan gives no sensitivity for composition measurements, see lower two lines in Fig. 27.

The right figure of Fig. 27 shows the impact of improved reconstructions. The Monte Carlo events have been smeared using a Gaussian distribution with standard deviation of $\sigma_E = A_E\, E$ and $\sigma_\theta = A_\theta \,/\, \sqrt{E/\mathrm{GeV}}$ for energy and zenith angle, respectively. A smearing with $A_i = 0.25$ estimates the impact of improved performance of event reconstructions explained in Sec. 2.4. Even better reconstructions with $A_i = 0.1$ show the increasing sensitivity. An improved zenith angle reconstruction yields better distinguishability of neutrinos passing the Earth core. A good energy reconstruction is necessary for the observation of the MSW resonance. With good reconstructions, an accuracy of a few percent can be achieved within 10 years.

### *7.5. Conclusions*

Resonant neutrino oscillations inside Earth driven by the large magnitude of the $\theta_{13}$ mixing angle can probe the composition of the Earth's core. These oscillations are sensitive to the electron density. With good knowledge of the mass density from seismic measurements, one can derive the proton to nucleon ratio $Z/A$ inside the Earth. In particular, the composition of the liquid outer core might be testable with PINGU. Depending on

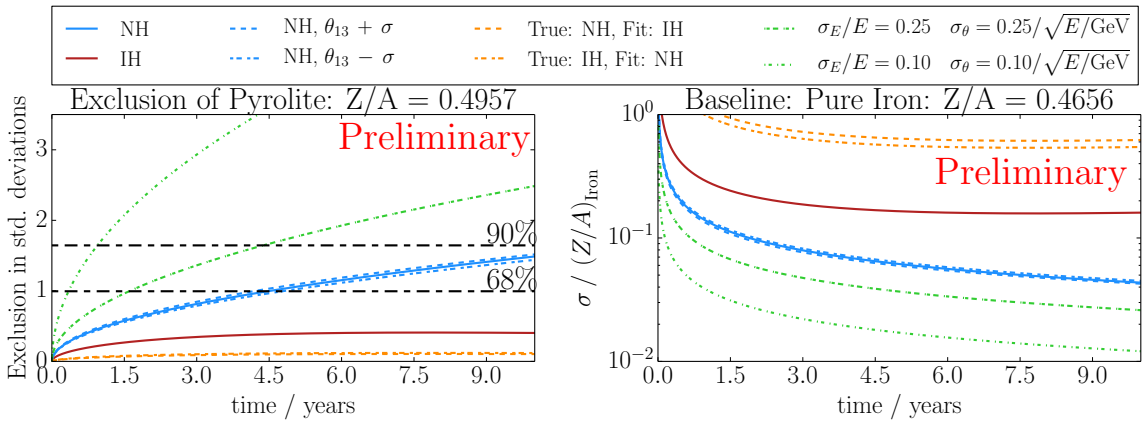


Figure 27: Left: Exclusion of a pyrolite core model (as in the mantle) with respect to a pure iron core a time range of ten years using the likelihood ratio method. Different cases of oscillation parameters are considered as well as normal and inverted hierarchy. Right: The accuracy, measured in units of $\sigma$, of the $Z/A$ measurement for the assumption of an iron core. In addition to systematic shifts, scenarios with better zenith angle and energy reconstruction assuming Gaussian smearing (green lines) are shown.

the mass hierarchy, PINGU could distinguish between Earth models assuming pure iron or mixtures of iron and lighter elements with 8% (NH) or 20% (IH) accuracy limited by the used energy and zenith angle reconstructions. Clearly, knowledge of the hierarchy is critical for understanding Earth core composition. However, measurement of the mass hierarchy is not strongly dependent on the core composition because the hierarchy measurement also uses neutrinos that cross only the mantle. These neutrinos can be used to fix the oscillation parameters and minimize systematics induced by these parameters. The uncertainty in $\theta_{13}$ is small enough to have negligible impact on Earth model determination. PINGU thus offers the best and possibly only way to test geophysical models of the Earth core's composition by measuring matter-induced neutrino oscillations of atmospheric neutrinos.

Further improvements to the Earth tomography analysis are possible with an improved event selection, potentially based on high-level reconstructions described in Sec. 2.4. These improvements would yield higher statistics in the interesting region, and allow a better identification of matter-induced oscillation effects by adding inelasticity measurements to the likelihood fit Eq. 5.

## 8. Dark Matter

### *8.1. Motivation*

Observational evidence for dark matter can be obtained at many scales, from the motion of stars to imprints on the cosmic microwave background (CMB) [70, 71, 72]. Dark matter candidates could be indirectly detected through the observation of signals produced from daughter particles created in dark matter self-annihilations. The search for neutrinos created as part of these annihilations is of particular interest, since neutrinos can be used to probe dark matter properties, as well as its self-annihilation and nucleon scattering cross sections. Weakly Interacting Massive Particles (WIMPs, denoted by $\chi$) are attractive candidates for dark matter, and arise naturally in many theories beyond the standard model of particle physics which were developed to explain the origin of electroweak symmetry breaking and solve the gauge hierarchy problem [72]. Although we will use the term WIMP and dark matter candidates interchangeably in the rest of the section, the reader should note that there are other scenarios that provide viable non-WIMP dark matter candidates [73, 74] with similar signatures in neutrino telescopes.

WIMPs could be captured in the Sun after scattering off nuclei, accumulate and self-annihilate producing a flux of neutrinos originating from the annihilation products. Under the assumption of equilibrium between WIMP capture rate ($\Gamma_C$) and annihilation rate ($\Gamma_A$) in the Sun, $\Gamma_A$ depends only on the total scattering cross-section. Since the Sun is primarily a proton target, strong constraints can be derived on the spin-dependent WIMP-proton scattering cross-section $\sigma_{p,SD}$ by measuring a neutrino flux from the Sun. IceCube has set the world's best limits on this process for WIMP masses above 50 GeV [5].

Searches for dark matter annihilation signals in the Milky Way can be used to test the thermal average of the WIMP annihilation rate, which is the product of the annihilation cross section and the relative velocity of WIMPs averaged over the velocity distribution, $\langle \sigma_A v \rangle$. IceCube has set tight constraints on $\langle \sigma_A v \rangle$ with searches for signals from the Galactic halo [75] and Galactic Center [76] and dwarf spheroidal galaxies and clusters of galaxies [77, 78]. These results improved upon theoretical predictions [79, 80].

PINGU will allow us to enhance current searches and extend the reach to test lower WIMP masses that are below the IceCube detection threshold. WIMP scenarios motivated by DAMA's annual modulation signal [81] and isospin-violating scenarios [82] would be testable.

### *8.2. Solar WIMPs*

The primary WIMP annihilation spectrum is model dependent, hence we consider two extreme benchmark scenarios, where WIMPs annihilate exclusively to $\tau^+\tau^-$ and $b\bar{b}$, respectively. The first case results in a hard neutrino spectrum, while the second case leads to a softer spectrum with lower average neutrino energy. One can expect that a general model with a mix of various annihilation channels will be bracketed by these two extrema.

#### *8.2.1. Experience from DeepCore*

The most recent IceCube Solar WIMP analysis [5] searched for signal neutrinos originating from potential WIMP masses, ranging from 20 GeV to 5 TeV. Within this mass-range, signal events can have very different event topologies in the detector. To accommodate all expected event topologies within one single analysis, the full dataset is split into three independent non-overlapping event selections that were later combined; first into two seasonal data streams, "summer" and "winter," when the Sun is above and below the horizon at the South Pole, respectively. The winter dataset comprises a low-energy and high-energy sample. During the summer period events are selected that interact inside DeepCore to reduce the down-going atmospheric muon background. The winter high-energy event selection has no particular track-containment requirement and aims to select upward-going muon tracks. The low-energy counterpart is focused on starting or fully contained neutrino-induced muon tracks inside DeepCore.

The inclusion of DeepCore allowed us to extend the search to the austral summer when the Sun is above the horizon and extend the WIMP mass reach from 50 GeV to 20 GeV, which was not possible in past IceCube searches [5]. Similarly, PINGU will allow us to extend to even lower WIMP masses.

#### *8.2.2. PINGU Sensitivity*

Building on the experience gained with DeepCore analyses we utilize the much improved energy detection threshold of PINGU to significantly lower the sensitivity for WIMP masses in the range between 5 and 50 GeV. We perform a straightforward event based Monte-Carlo (MC) study, using the baseline 40-string PINGU detector geometry as described in Table 1. The datasets are identical to the ones used in the neutrino mass hierarchy sensitivity studies, described in Sec. 4. In contrast to previous IceCube WIMP

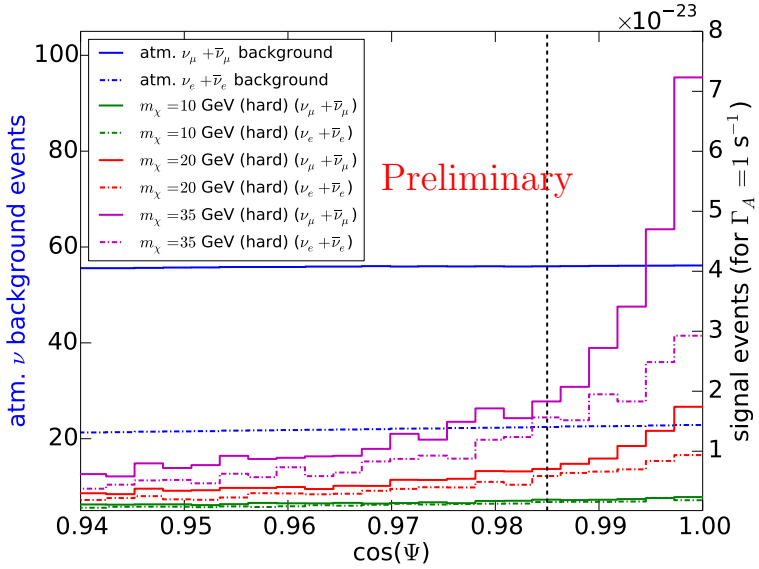


Figure 28: Background (left ordinate) and signal (right ordinate) event number distributions as a function of the cosine of the opening angle $\Psi$ from the Sun. The dashed vertical line shows cos(10°). Solid and dashed-dotted lines show the contributions from the track and cascade channels, respectively. Signal lines show the expected number of $\nu$-signal events for different WIMP masses and annihilation into $\tau^+\tau^-$ (hard $\nu$ energy spectrum). An annihilation rate $\Gamma_A$ of 1 s$^{-1}$ has been assumed for those lines.

searches where we relied solely on the track channel produced by muon neutrino CC interactions, here we take advantage of PINGU's ability to reconstruct cascade directionality and use all neutrino flavors and interactions. While PINGU will offer the additional potential to use energy spectral information [83] as well, we do not use that here. This study focuses on the low-mass WIMP range and considers only events that interact inside the PINGU volume.

In accordance with the assumptions in Sec. 4 the down-going atmospheric muon background is completely vetoed, so that the background consists only of atmospheric muon neutrinos, which are generated following the Honda flux model. The background at final analysis level from atmospheric neutrinos has previously been calculated to be of order one event [5], and is consequently not included.

All signal simulations are made with DarkSUSY [90] and WimpSim [91], which describe the capture and annihilation of WIMPs inside the Sun and the consequent production, interaction, and propagation of neutrinos from the core of the Sun to the detector, in-

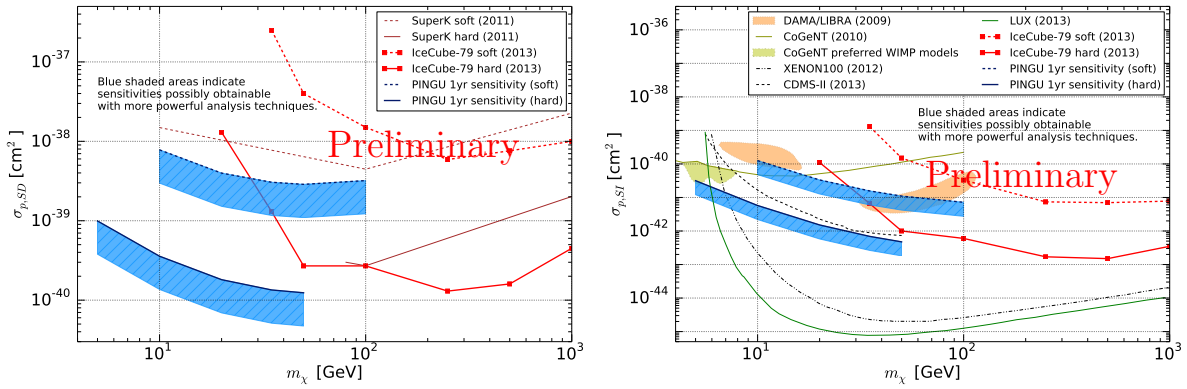


Figure 29: PINGU 40-string sensitivity on $\sigma_{p,SD}$ (left figure) and $\sigma_{p,SI}$ (right figure) for hard (solid blue) and soft (dashed blue) annihilation channels over a range of WIMP masses for a live-time of one year. The sensitivities are compared to the present IceCube limits [5] and limits from Super-K [84], CoGeNT [85], XENON100 [86], CDMS-II [87], and the LUX experiment [88]. The filled patches mark possible signal regions associated with data from DAMA/LIBRA [89, 81] and CoGeNT [85].

cluding three-flavor oscillations and matter effects. The expected neutrino signal flux from WIMP annihilations in the Sun is calculated by weighting the simulated neutrino events with the WIMP channel dependent neutrino spectra obtained from DarkSUSY. The zenith dependent Sun position throughout the year is accounted for.

In this study, the event selection explicitly follows the one detailed in Sec. 4. All events are required to have a successful reconstruction and satisfy the additional containment criteria listed in 4.1.1. We apply a fixed search window around the position of the Sun with a half-cone opening angle of 10°. Figure 28 shows the number of expected background and signal events as a function of the angle $\Psi$, defined as the angle between the reconstructed track/cascade and the direction of the Sun, for an expected live-time of one year. Fig. 28 shows three different signal channels with increasing WIMP mass assuming an annihilation rate of $\Gamma_A$=1 Hz. Solid and dash-dotted lines show the contributions from the track and cascade channels, respectively. The sum of the bin contents from $\cos(\Psi) = 1$ to $\cos(\Psi) = 0.985$ (indicated by the dashed black vertical line) yields the total number of background ($n_{\rm bg}$) and signal events ($n_{\rm s}$) for a cone around the Sun with an half-opening angle of 10°, respectively.

Under the assumption of no signal, we calculate the 90% CL median upper limit $\mu_{\rm s}^{90}$ on the number of signal events, given $n_{\rm bg}$, using [92]. The limit on $\mu_{\rm s}^{90}$ is compared to $n_{\rm s}$, which was calculated for $\Gamma_A = 1$ s$^{-1}$, to derive the 90% CL limit on $\Gamma_A$ for each

WIMP model. Limits on $\Gamma_A$ are then converted into limits on the spin-dependent, $\sigma_{p,SD}$, and spin-independent, $\sigma_{p,SI}$, WIMP-proton scattering cross-sections, using the method from [91]. Figure 29 shows the calculated sensitivities as a function of WIMP mass for the soft (blue dashed) and hard (blue solid) annihilation channels obtained in this study. The blue shaded areas indicate the expected range of sensitivity possibly obtainable with improved analysis techniques. Such improvements include higher signal selection efficiency, an optimized maximum likelihood analysis as used in [5], and better atmospheric neutrino background rejection (e.g., through use of spectral information). Additional ideas to further advance this search are discussed below. In contrast to the expected improvements (shaded area), we are currently not able to reliably quantify their impact on the expected sensitivity.

### *8.3. Galactic Center WIMPs*

The expected differential neutrino flux from dark matter annihilations at the Galactic Center (GC) is proportional to the differential neutrino multiplicity per annihilation, $\frac{dN_\nu}{dE}$, and the line of sight integral over the square of the dark matter density at an angle of $\psi$ from the GC, $J(\psi)$ [79].

Searches for dark matter self-annihilations in the GC have been performed by IceCube in the past, using the NFW dark matter density profile [93] as a benchmark. The first GC analysis used the partially instrumented 40-string IceCube detector, probing $\langle \sigma_A v \rangle$ for WIMP masses down to 100 GeV for several annihilation channels [76]. The two most recent GC analyses use the almost-completed IceCube detector (comprised of 79 strings), including DeepCore [94]. DeepCore allows us to constrain WIMP models with masses as low as 30 GeV. The sensitivity to $\langle \sigma_A v \rangle$ in the GC was improved by up to four orders of magnitude for WIMP masses of 100 GeV ($\tau^+\tau^-$) compared to the previous IceCube 40-string analysis. For PINGU an even lower energy threshold in the sub-10 GeV region is expected.

The GC, in the southern hemisphere at $-29^\circ$ declination, is a challenging target for IceCube due to the high rate of down-going atmospheric muon background events. Veto methods against atmospheric muons [94], that were developed for the most recent 79-string GC analysis, significantly improved the sensitivities of analyses focused on low-energy events in the southern hemisphere. This turns IceCube into an efficient $4\pi$ detector for indirect dark matter searches. These methods reject muon background while retaining low energy starting events inside a fiducial region, and make it feasible to achieve an event selection with an adequate neutrino purity for PINGU.

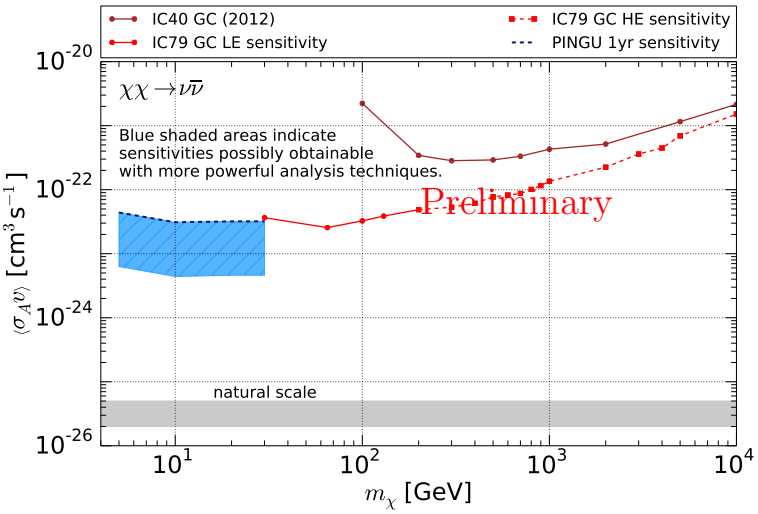


Figure 30: PINGU 40-string sensitivity on $\langle\sigma_A v\rangle$ for direct annihilations into neutrinos over a range of WIMP masses for a live-time of one year. The sensitivities are compared to limits from the IceCube 40-string analysis [76] and the sensitivities of the most recent 79-string GC analyses [94].

The sensitivity to $\langle\sigma_A v\rangle$ for a GC analysis for WIMP masses between 5 and 30 GeV with PINGU is derived in a straightforward event-based MC analysis. This analysis is very similar to the study described in Sec. 8.2. In contrast to the solar WIMP analysis, where a perfectly efficient atmospheric muon veto was assumed, we use the level of atmospheric muon background in the 79 string GC analysis (neutrino purity of 10% at final analysis level). This provides a conservative sensitivity estimate for PINGU. We assume a live-time of one year, the baseline 40-string PINGU detector geometry, and WIMP annihilations into neutrinos for this study. The resulting neutrino line spectrum yields approximately equal number of neutrinos and anti-neutrinos of all flavors after annihilation and neutrino oscillations. We consider muons produced through CC interactions the only signal detection-channel for this conservative study (all-flavour prospects are discussed below). The number of signal and background events are calculated in a cone around the GC with a half-opening angle of 10° by weighting the simulated neutrino events according to the expected signal and atmospheric neutrino background flux, respectively. The number of expected atmospheric muon background events ($n_{\mathrm{bg},\mu}$) are added to the atmospheric neutrino background ($n_{\mathrm{bg},\nu}$) with expected purity to determine the total background ($n_{\mathrm{bg}}$).

Using the statistical method as described in section 8.2.2, we derive the 90% CL limit on $\langle\sigma_A v\rangle$ for each WIMP model. Figure 30 shows the calculated sensitivities as a function of

WIMP mass for the direct neutrino annihilation channel obtained in this study. Again, the blue shaded areas indicate the expected range of sensitivity possibly obtainable with improved analysis techniques. Here, the expected range of sensitivities spreads over a larger region than in Sec. 8.2, driven by the remaining contribution of atmospheric muons to $n_{\mathrm{bg}}$. Consequently, the most optimistic range of the blue shaded area assumes a more efficient atmospheric muon veto (perfect muon veto in the limit).

*8.4. Outlook and conclusions*

With one year of data PINGU will be able to test claims of signals in the spin-independent region for dark matter annihilations in the Sun yielding hard neutrino spectra. The search for neutrinos from dark matter annihilations in the Sun will provide an independent method to test the anomalous signals from DAMA/LIBRA [89, 81], CoGeNT [85, 95], and the silicon data from CDMS-II [87] (CDMS-Si). PINGU will also be able to test for dark matter annihilations near the Galactic Center.

The PINGU sensitivities discussed in this Letter are based on standard analysis methods utilized in IceCube, which have been kept intentionally simple. The results presented here are therefore a conservative estimation since PINGU offers the possibility of applying analysis methodologies that go beyond what we have used thus far in IceCube and DeepCore. These include a more precise definition of contained and partially-contained events, a better energy estimation from the measured track length allowing us to use spectral information, and particle identification, each of which can potentially confer greater sensitivity to dark matter.

## 9. Supernova Neutrinos

### *9.1. Introduction*

If a core collapse supernova explosion were to happen in the near future in our galaxy, IceCube would provide the world's most precise neutrino rate determination, with a significance larger than 20 standard deviations for distances up to 20 kpc. The signal is statistically extracted from the coherent rate increase in all IceCube sensors that is induced by Cherenkov photons emitted from neutrino-induced positrons. The noise rates of individual DOMs are roughly 500 Hz, which can approximately be cut in half by applying an artifical deadtime, eliminating most of the correlated noise observed at low temperatures. The supernova detection significance deteriorates significantly at the positions of the Magellanic Clouds and beyond because the neutrino fluence depends on the inverse distance squared and the DOM noise becomes dominant. Furthermore, individual neutrino interactions are not detected such that the energy and type can not be determined for each neutrino. However, it has been shown [96], that the average neutrino energy can in principle be traced to better than 30% accuracy for distances less than 10 kpc. Recently, the IceCube data acquisition system has been upgraded to store the timestamps of all hits. With this information at hand, one can deduce the neutrino energy from a comparison of single rates with coincident rates, where the latter is the rate at which a single neutrino interaction deposits light in two (or more) neighboring modules. In IceCube, however, the coincidence rates are only on the order of a few per mil if a tight coincidence window is used.

Due to the much higher sensor density both vertically and horizontally, the coincidence rates in PINGU will be much higher, of order 1%. This will lead to a much improved determination of the average neutrino energies, particularly at larger distances, and will allow one to extract information on the neutrino energy spectral shape. In addition, some improvement in the detection significance for supernova explosions in dwarf galaxies orbiting our Milky Way may be achieved by employing coincidences in a short coincidence interval $\Delta t$. Note that the significance for a supernova detection with $n_k$ signal events and optical module noise $r$ roughly scales like $n_k \cdot (\Delta t \cdot r)^{-k/2}$ for a k-fold coincidence.

### *9.2. Monte Carlo Simulation*

Two simulations were conducted to independently characterize the sensitivity of the PINGU low energy in-fill. In the first simulation, the effective volume is evaluated for var-

ious coincidence conditions for each detector configuration, namely IceCube, DeepCore, and PINGU, where the latter sub-array consists of 20 strings of 60 standard IceCube DOMs operating at $4\pi$ sensitivity. In the second simulation, the significance of the collective rate deviation is determined with respect to supernova distance for the IceCube detector in comparison to its subsequent generation extensions, DeepCore and PINGU. This simulation considers the baseline 40-string PINGU geometry discussed generally in this letter.

The first simulation was conducted and cross checked with two independent GEANT-4 based codes for various detector configurations (IceCube, DeepCore and PINGU). The light yield is found to roughly scale with the absorption length in the ice. Uncertainties connected to the varying ice properties as a function of depth were assessed.

It is important to reject atmospheric muons when applying tight coincidence criteria. The atmospheric muon simulation used in this study was generated following the Gaisser flux model [97]. In a second step, a simple and efficient muon rejection algorithm was applied. A second set of atmospheric muon background was simulated as a cross check, using standard IceCube simulation tools and the CORSIKA air shower generator [98]. These studies demonstrated that the distance reach and average energy determination are not strongly affected by the presence of the remaining atmospheric muon background. However, some improvements should be possible by using the outer detector layers to act as a veto.

The detector sensitivity can be characterized by the effective positron volumes per optical module $V_{\rm eff}(e^+) = N_{\rm detected}/n({\rm e}^+)$, where $N_{\rm detected}$ is the number of detected hits in each optical module for a given coincidence condition. The energy dependent density of positrons from neutrino interactions in the ice is denoted by $n({\rm e}^+)$. Table 4 summarizes the effective positron volumes, assuming an average neutrino energy $\langle E_{\bar{\nu}_{\rm e}} \rangle = 12.6$ MeV. The numbers are provided for IceCube, DeepCore and PINGU, imposing various coincidence criteria. Clearly, PINGU would provide substantially larger coincidence probabilities than IceCube.

In the second study, low energy supernova neutrinos were injected in each detector geometry (IceCube, DeepCore, PINGU) with levels responding to a O-Ne-Mg 8.8 $M_\odot$ supernova [99] at 10 kpc. The collective hit rate throughout the entire detector is compared to the expected non-Poissonian noise levels, generated with the detector noise model. The significance, calculated as the collective rate excess per DOM $\Delta\mu$ divided by its measured uncertainty $\sigma_{\Delta\mu}$, is approximately proportional to the square root of the total number

| Detector | single hit | nearest neighbor | triple coincidence |
|---|---|---|---|
| IceCube | 583 $m^3$ | 0.6 $m^3$ | 0.0002 $m^3$ |
| DeepCore | 767 $m^3$ | 2.7 $m^3$ | 0.03 $m^3$ |
| PINGU | 912 $m^3$ | 4.4 $m^3$ | 0.11 $m^3$ |

Table 4: Effective positron volumes $V_{\text{eff}}(e^+)$ per optical module for various coincidence conditions in IceCube, DeepCore and PINGU, assuming $\langle E_{\bar{\nu}_e} \rangle = 12.6$ MeV.

of optical modules within the detector (see Fig. 31). For statistically independent DOM rates, it should be distributed according to a Gaussian with unit width[6], such that its value corresponds to the number of standard deviations from the null hypothesis of no signal.

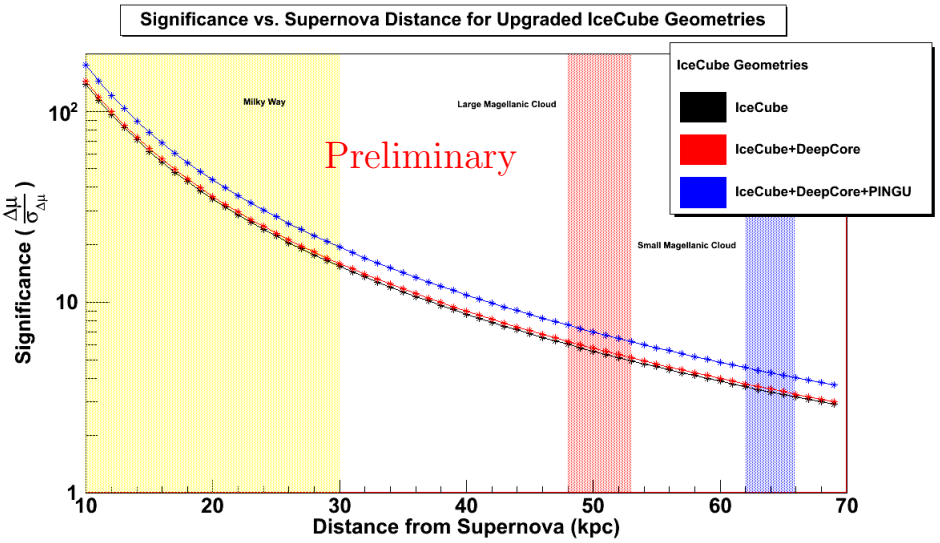


Figure 31: Significance as a function of distance for a a O-Ne-Mg 8.8 $M_\odot$ supernova [99]. The sensitivity of the baseline 40-string PINGU geometry is compared to the standard IceCube geometries. For reference, the positions of the Milky Way and the Magellanic Clouds are indicated. Note that a trial factor is not included.

[6]In practice, statistically correlated hits introduced by atmospheric muons cannot be fully removed, which leads to a widening of the distribution.

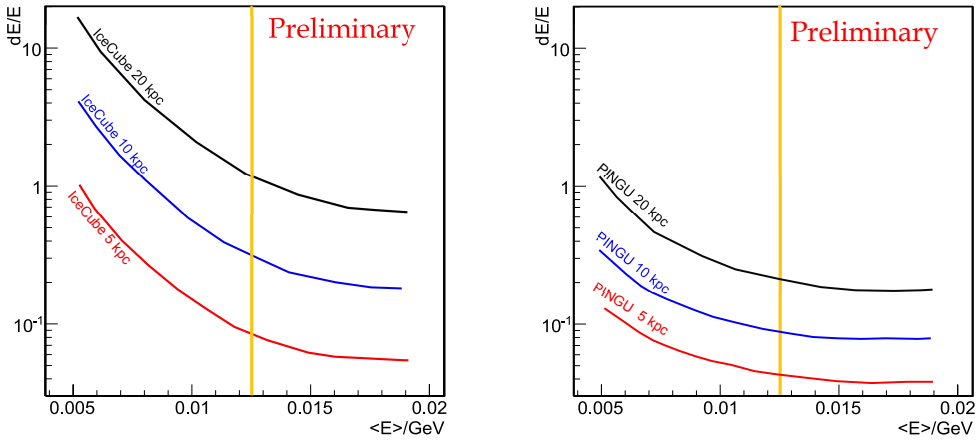


Figure 32: Comparison of the precision on the determination of the average neutrino energy in (left) IceCube and (right) PINGU 20-string geometry for a supernova at 20 (black), 10 (blue) and 5 (red) kpc distance.

### *9.3. Determination of the average neutrino energy*

The average neutrino energy is correlated with the ratio of coincident events to single hits. By exploiting this information for a future galactic supernova, the average neutrino energy could be determined in IceCube with MeV resolution for a supernova at 10 kpc distance. The energy dependence becomes stronger when the optical modules are closer together yielding a higher rate of coincidences. It has previously been demonstrated that sub-MeV resolutions for dense core detectors [96, 100] can be achieved.

The relative precision is depicted in Fig. 32 as function of distance and average energy. To be most conservative, flux, energy and spectral shape were taken from the collapse of an O-Ne-Mg 8.8 $M_{\odot}$ progenitor star, the lowest mass progenitor known to undergo a core collapse. We also assume the conservative case of a partially instrumented PINGU configuration with 20 strings.

### *9.4. Providing a measure of the spectral shape*

Different coincident hit modes show distinct differences in the neutrino energy dependence. These can be used to characterize the spectral shape of the neutrino emission, in addition to the average energy. Assuming a neutrino spectral shape parametrized with three parameters, the luminosity $L_{\nu}$, the average neutrino energy $\langle E_{\bar{\nu}_e} \rangle$ and a shape parameter

$\alpha$ [101] and using single, double and triple coincident hit modes in a $\chi^2$ fit, $\langle E_{\bar{\nu}_e} \rangle$ and $\alpha$ can be extracted simultaneously.

A scan of the parameter space for a simulated supernova at 10 kpc distance is shown in Fig. 33 as function of average energy and $\alpha$ for IceCube and PINGU. The color scale indicates the $\log_{10}(\chi^2)$ value for the parameter values tested. Note that $\alpha$ and $\langle E_{\bar{\nu}_e} \rangle$ are almost degenerate. The increased rates at higher hit modes in PINGU lead to a substantially smaller uncertainty on the parameters.

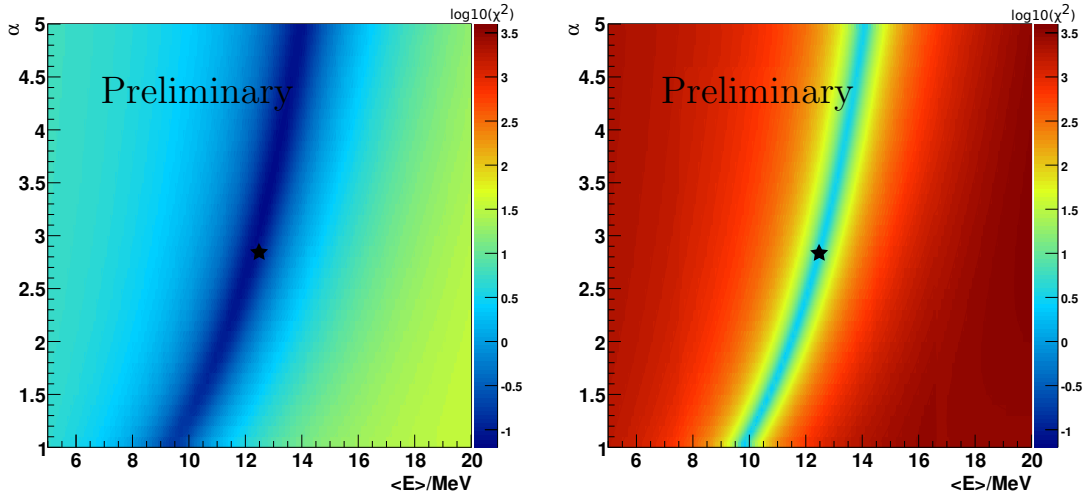


Figure 33: Combined determination of the average neutrino energy and the spectral shape parameter $\alpha$ for IceCube (left) and PINGU (right) using a $\chi^2$ method. The input value ($\langle E_{\bar{\nu}_e} \rangle = 12.6$ MeV, $\alpha = 2.84$) is denoted by a star.

### *9.5. Conclusions and outlook*

PINGU will enhance IceCube's ability to detect and interpret very low energy ($E_\nu \sim$ 15 MeV) neutrino bursts from supernova explosions. With a dense array of 40 PINGU strings deployed with hiqh quantum efficiency sensors, the galactic supernova sensitivity will almost double when compared to IceCube alone. The greatest benefit comes from the improved determination of the average supernova neutrino energy provided by PINGU's closer module spacing. The average energy will be measured roughly a factor of five better than with IceCube. PINGU would also allow us to determine the spectral shape, once the average neutrino energy is known.

Lowering the PMT noise rates will be an important ingredient for the detection of supernovae in neighboring galaxies in an envisaged low energy, multi-megaton future detector succeeding PINGU. Very low noise rates should be achieved by collecting light with wavelength shifters, read out with highly sensitive PMTs with a small cathode area. Extending the accepted wavelength range down to 200 nm by using fused quartz windows would increase the detection efficiency by a factor of approximately 2.7 (weighted for the optical module sensitivity and the $1/\lambda^2$ dependence of the Cherenkov photon flux). The PINGU deployment will allow us to test these technical improvements by deploying prototype modules as discussed in section 14.1.

## 10. Instrumentation

### *10.1. IceCube-Based Design*

The PINGU instrumentation plan closely follows the design successfully used in IceCube and its DeepCore extension. Many engineering tasks have already been completed for IceCube and can be directly reused or leveraged for PINGU.

### *10.2. Sensor Configuration*

As described earlier in Sec. 2.2, the baseline PINGU detector will consist of 2400 optical sensor modules deployed within the DeepCore section of the IceCube volume (Fig. 5), at depths 2150-2450 m. Each module includes a 10-inch diameter Hamamatsu R7081-02MOD PMT with enhanced quantum efficiency like those used in DeepCore, along with electronics to operate the PMT, send digitized signals to the surface, and perform calibration tasks.

### *10.3. Optical Sensor Design*

The PINGU sensor module (PDOM, Fig. 34) will be similar to the IceCube Digital Optical Module (DOM) [102], with updates and appropriate adaptations. The exterior components will be identical or only minimally adjusted, in order to make use of the IceCube experience as direct verification of the corresponding design requirements. These include the glass sphere, cable penetrator, electrical connectors, external hardware and assembly procedures. This reuse is particularly important because of the challenging environment during deployment and freeze-in. Of the 5160 IceCube DOMs deployed at depth, 98.4% were operable after this critical phase, with only 0.4% failing in subsequent long-term operation.

Critical components inside the DOM are also well-proven for long-term reliability and can be directly employed in the PDOM design, including the PMT and base divider, optical gel, mu-metal shield, and the high voltage generator.

As shown in Fig. 35, the PDOM will have a single "Main Board" containing electronics for waveform digitization, control, and communication with the surface. Modules on this board will reproduce most of the functionality of the original DOM Main Board,

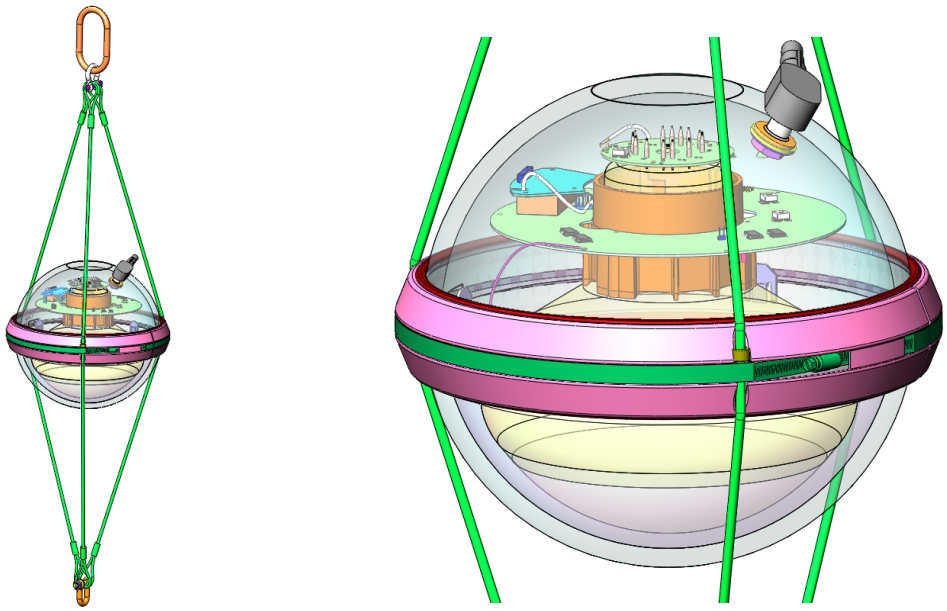

Figure 34: PINGU Digital Optical Module (PDOM).

which cannot be remanufactured due to numerous obsolete components. The new design includes simplifications and uses up-to-date electronic technology to reduce cost, power and board space. The previous multi-channel analog circuitry and custom digitizers are replaced by a single commercial ADC chip, with triggering and data processing handled by a more capable FPGA-based processor. All triggered waveforms will be sent to the surface after suitable compression, allowing the new design to omit complex circuitry previously used to detect local coincidences between modules. As before, PMT waveforms will be digitized and deconvolved as needed into individual photoelectron signals; the new design will allow the deconvolution to be done before transmission of data to the surface.

Table 5 lists comparisons with the IceCube DOM, including specification of time and charge resolutions similar to those previously achieved. Because of the lower typical event energy compared to IceCube, the reduced dynamic range of 100 photoelectrons per 15 ns is expected to be sufficient, but the final specification will be determined after further simulations.

Simplifications of the Main Board design also allow us to incorporate the high voltage

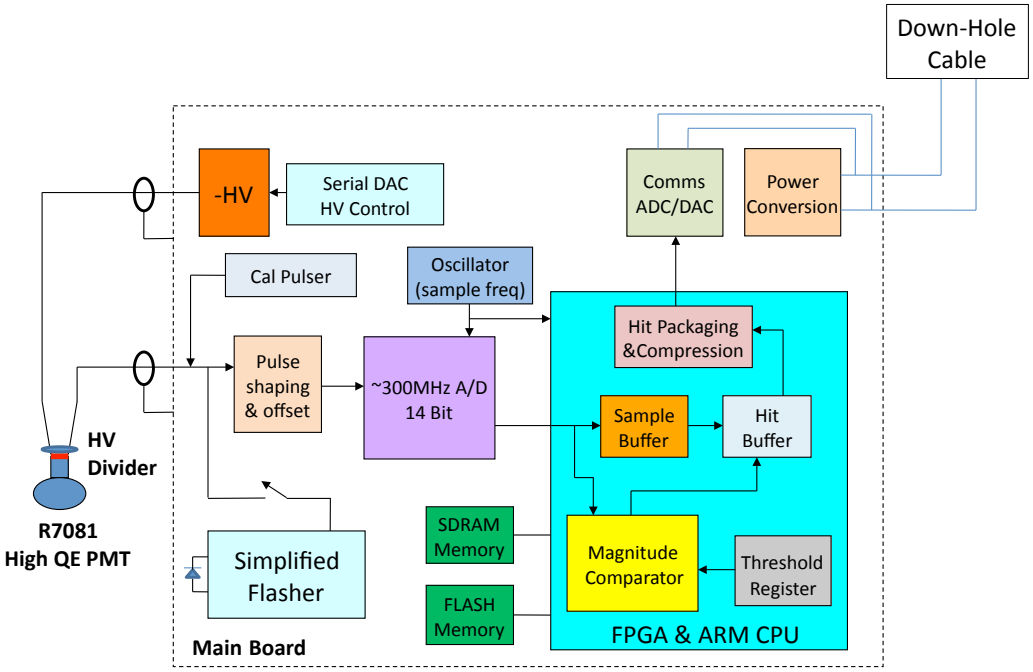


Figure 35: Functional block diagram for data acquisition in the PDOM, focusing on the Main Board.

generator and calibration flasher components (Sec. 12) onto this same board, reducing the overall module complexity and cost. The previous design also included an analog delay board to allow for triggering the custom waveform digitizers after detection of a PMT pulse. This is not needed in the new design because the continuously-digitized PMT output is buffered in the FPGA while threshold crossings are detected digitally.

As part of the Main Board redesign, the PDOM firmware programming will be updated. This will be done in a way that preserves the original code structure and communications protocols as much as possible, ensuring a high level of compatibility with existing modules in the IceCube data acquisition system.

| | PDOM Specification | Original (IC) DOM |
|---|---|---|
| Glass sphere | Benthos 13" borosilicate | same |
| Cable penetrator, connector | SEACON custom assembly | same |
| PMT | 10 inch diameter, R7081-02 (Hamamatsu, High-QE version) | same (IC DeepCore) |
| SPE Time Resolution (relative to PDOM clock) | 2 nsec | same |
| SPE Noise Rate at –20°C | <500 Hz | same (IC DeepCore) |
| Clock Synchronization | 3 nsec | same |
| Digitizer Charge Resolution | <0.1 SPE | same |
| Linear Dynamic Range Limit | 6 PE/nsec (digitizer limit) | 30 PE/nsec (PMT limit) |
| Power Consumption | 2 W | 3.5 W |
| Multi-hit Coincidence | Not required in-ice | Required for full readout |

Table 5: PDOM design specifications compared to the original IceCube DOMs as built.

### *10.4. Cable*

Each PINGU string will be deployed along a single cable similar to the IceCube cables. These cables consist of multiple twisted wire pairs, each of which serves power and communications for several PDOMs, a polymer core for structural support, and a tough outer sheath. The PINGU module spacing motivates some changes to the cable configuration, but the electrical and mechanical specifications will be essentially the same as for previous IceCube cables. As for the PDOM design, this allows reuse of a proven engineering solution, leveraging the IceCube project experience with procurement and verification of this critical component.

Figure 36 shows how the PDOMs are attached to the down-hole cable. The cable itself carries the load from the top of the PDOM chain, up 2150 m to the surface of the ice. In the instrumented depth range, the load is carried alternately by short segments of steel wire rope and the PDOM harnesses, with electrical cables secured appropriately alongside. The main load is transferred from the down hole cable to the steel rope by grips above the topmost PDOM and at the bottom of the chain. These cable grips are like those used in IceCube above and below every DOM, but the closer PINGU spacing allows most of them to be replaced by the simpler and lower cost steel rope hardware.

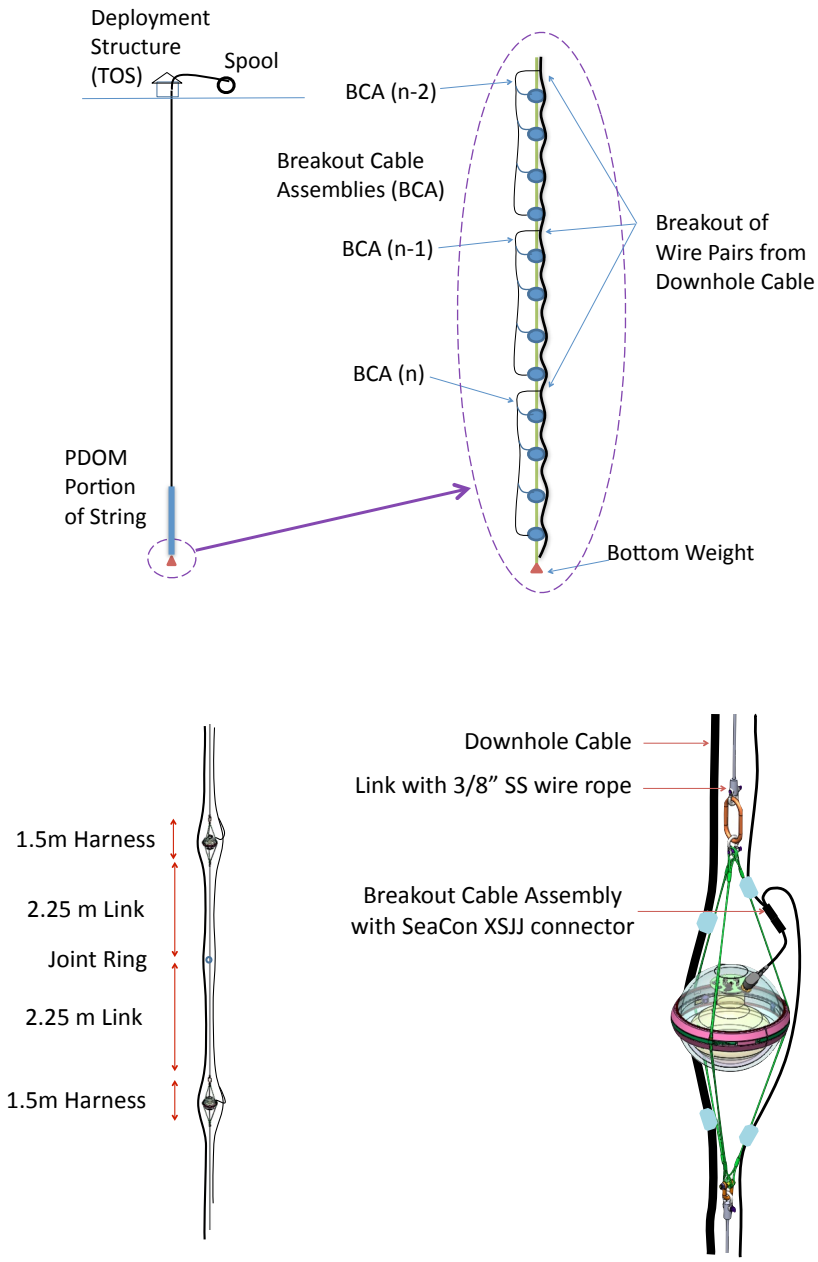


Figure 36: Attachment and support of PDOMs along a PINGU string. The Seacon XSJJ connectors are of the same type used in IceCube.

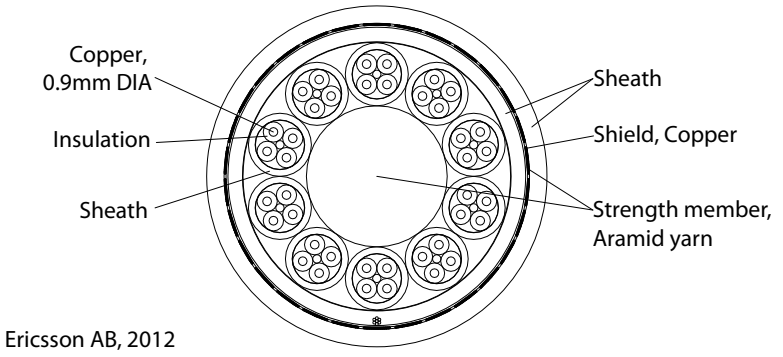


Figure 37: Cross section of an Ericsson cable designed for a PINGU string. Outer diameter is 36 mm.

Because of a lower power design and improved data compression in the PDOM, fewer wire pairs are required compared to IceCube. As shown in Fig. 36, each group of four PDOMs is serviced by one wire pair broken out from the main cable. This is to be compared with only two DOMs per wire pair in IceCube. Another simplification of the cable design comes from the omission of extra wires previously dedicated to detecting local coincidences between module hits, so that each breakout construction is much more straightforward. Together with the smaller number of breakouts per string, which could even be grouped as two wire pairs per eight PDOMs, the changes amount to a significant savings of cost and risk. Figure 37 shows a corresponding adaptation of the IceCube cable design supplied by Ericsson AB, the manufacturer of the original cables.

Strings are connected to data acquisition computers via surface cables that run to the IceCube laboratory building. New cable entry points will likely be required for the PINGU surface cables, as the existing ones are nearly full and can only accommodate up to 20 additional cables.

### *10.5. Drilling and Deployment*

PINGU strings will be deployed in holes drilled with an upgraded IceCube Enhanced Hot Water Drill, each approximately 55 cm diameter and 2500 m depth as for the original IceCube strings. The drill provides 5 MW of thermal power in the form of a high-pressure (1000 psi) and high flow (200 gallons/minute) 90°C water jet to melt ice to a depth of 2500 m in 30 hours. After drilling each hole, a string of modules is deployed over a period of 10 hours and will be fully frozen after 3 weeks.

During construction of IceCube, a highly trained crew of 30 drillers were able to drill up to 20 holes in each South Pole construction season (Table 6). Key personnel from the IceCube project and the South Pole support network remain active in hot water drilling and will still be available for PINGU, enabling PINGU to leverage their extensive experience to optimize the required drilling time and effort. Existing equipment and procedures can be utilized, including necessary refurbishment and replacement of some components, to complete PINGU construction within four seasons. As shown in Table 7, the first season will be used for reassembly, staging and testing of the drill equipment, followed by three for drilling and deployment.

| Season | Strings deployed |
|---|---|
| 2004-2005 | 1 |
| 2005-2006 | 8 |
| 2006-2007 | 13 |
| 2007-2008 | 18 |
| 2008-2009 | 19 |
| 2009-2010 | 20 |
| 2010-2011 | 7 |

Table 6: IceCube yearly records for drilling and deployment.

| Season | Special activities | Strings Deployed |
|---|---|---|
| 2016–2017 | Drill Rebuilding and Staging, Firn Pre-drilling | |
| 2017–2018 | Recommission Drill | 6 |
| 2018–2019 | | 16 |
| 2019–2020 | Decommission Drill | 18 |

Table 7: PINGU drilling and deployment schedule.

The IceCube drill is a complex system with many components, including complete written and video documentation of its operation. Following the last deployments in 2010–2011, the system was winterized for storage and to facilitate reuse (Fig. 38). Major components remain in IceCube/NSF stewardship, such as the hose reel, drill towers, and associated structures. These represent significant engineering solutions and assembly efforts that can be reused by PINGU. Heating plants, high pressure pumps, and water tanks remain similarly available. Other components were allocated for use by other projects. Only

Figure 38: IceCube drill components stored at South Pole, 2011.

some of those components are still at the South Pole. A preliminary inventory of drill-related equipment needing replacement has been made for PINGU cost estimation (see Sec. 15). To recommission the drill system, PINGU will likely need to replace the main drill hose, cable reels, electrical generators and distribution, the independent firn drill, and the Rodwell system that supplies make-up water from melted snow.

Certain aspects of the drilling system will be upgraded for PINGU. In particular, improvements are planned that will increase optical clarity of the refrozen ice near the PDOMs. In AMANDA and IceCube, it was found that light scattering is enhanced in such refrozen ice, modifying the DOMs' angular response function and complicating calibration and systematic error studies. The effect is most apparent for near-vertical background muons, where downward traveling light gets scattered in the upward direction and more easily strikes the PMT photocathode (Fig. 39). Study of the amount and timing of photons in such events has resulted in a quantitative hole ice model that is routinely used for simulation and analysis of neutrino events in IceCube. Subsequently, a camera system

was deployed in one IceCube hole and confirmed the scattering visually.

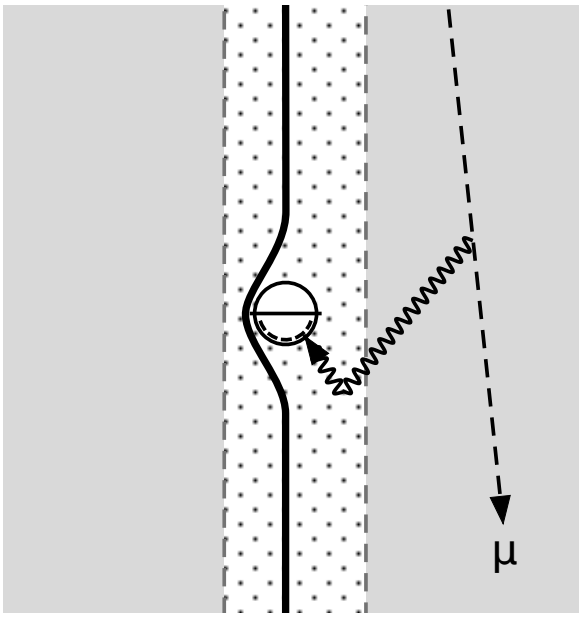


Figure 39: Scattering of light by bubbles in hole ice near DOMs in IceCube. The photocathode is on the bottom side of each DOM, indicated with a dashed curve.

The hole ice scattering is believed to be caused by dissolved gas that comes out of solution as very small bubbles during the refreeze process. For the surface tanks of the IceCube array (IceTop), a special degassing system was used to ensure clear ice, but this degassing was not performed for water in the deep holes of AMANDA and IceCube. Glacial ice incorporates air entrained with the snow from which it was slowly formed over thousands of years, but in a clathrate solid form that is optically clear. The hole refreeze process takes place over a much shorter time scale, apparently resulting in the observed clouding. Supporting this view is the amount of air measured in the original ice, about 600 mg/kg, and the solubility of air in cold water, only 20 mg/kg at 1 bar. Drill circulation passes about two-thirds of the meltwater through equipment at the surface, where much of the gas can escape, but the remaining one-third still contributes 200 mg/kg to the final mix. During refreezing, the inward growing ice phase can exclude this dissolved gas into the remaining liquid phase along the axis, where the concentration thus increases until it reaches saturation even at the high pressures in the hole (200 bar). At this point bubbles can be expected to form a cloudy core, consistent with the camera observations.

For PINGU, the drilling operation will be modified so that the instrumented region of the hole contains only water that has been brought to the surface and degassed. Standard membrane degassing equipment will remove 85% of air dissolved at atmospheric pressure, leaving only 3 mg/kg for return to the hole. By slowing the drilling in the bottom 350 m of depth and then raising the drill head slowly while injecting cold degassed water, gas-laden water will be displaced above the PINGU fiducial volume while adding only a few hours to the drilling time. Other changes and additional filtering will also prevent introduction of mineral impurities from the heating equipment and their possible precipitation. Possible ways to reduce ice fracturing through pressure reduction during refreeze are also under consideration. In this way the PINGU hole ice is expected to be made effectively clear. The final degree of light scattering near PINGU modules, as well as in the bulk ice away from the holes, will be precisely calibrated by studies with LED beacons and downgoing background muons (Sec. 12).

Deployment of PDOMs into PINGU holes will be similar to IceCube deployment, with some modification for the use of steel wire rope between PDOMs (Fig. 36). One AMANDA string was successfully deployed with such steel rope, but the standard IceCube procedure involved attachment of harnessed DOMs directly to the main electrical cable, with installation of special grips for transferring the vertical load between harness and cable. In PINGU, the chain of sensor modules will be assembled and lowered by repeatedly adding harnessed PDOMs and steel rope links. This is done in an iterative process that supports the already deployed section on a tethered hook while the next PDOM or rope segment is suspended above it from a chain hoist. After attachment of the new component, the whole load is hoisted slightly up to allow detachment of the tether and then lowered a few meters to allow attaching the new top to the tether. In synchrony with this, the main electrical/support cable is lowered and secured appropriately to the PDOM chain, along with its breakout cable assemblies that connect to the PDOMs. After the final PDOM link is deployed, support is transferred to a grip on the main cable and the assembly is then lowered 2150 m into the hole. The equipment for handling the main cable, the enclosing structure and procedural safeguards can all be reused from IceCube, giving confidence in achieving a similarly successful operation.

## 11. The Data Acquisition System

The IceCube data acquisition system (DAQ) is now a mature and well-understood composition of firmware and software components maintained by a team of IceCube scientists and software professionals. In order to leverage the existing infrastructure, the PINGU digital optical module (PDOM) will be designed in such a way as to be compatible with the IceCube DAQ.

### *11.1. PDOM Firmware and Software*

As described in section 10.3, PDOMs, like their IceCube counterparts, trigger and digitize PMT pulses autonomously. In the case of the PDOM, the digitization process is foreseen to be continuous and the trigger formed digitally with logic in the FPGA. Triggered pulses will then be sent to a deconvolution module existing in firmware or software or some combination of the two running within the PDOM. This module will extract the underlying photon pulse charge and local time stamp from the sampled waveforms and output the resulting list of (charge, time) pairs to a memory buffer. The data volume of this representation of the pulses is approximately ten times more compact than the uncompressed waveforms, thereby dramatically increasing the effective buffer depth on the DOM and decreasing the bandwidth requirements on the DOM-to-surface communications channel. The information content of these data objects will be made compatible with the stream output by the IceCube DOM: the minimum needed to process the objects is an identifier of the originating channel and a timestamp. Further information, such as charge, is optional and may be used if available. To support these anticipated changes in the PDOM hardware design, the following new features will be implemented:

- PDOM-specific digitizer hardware, including firmware-based trigger
- PDOM-specific FPGA and embedded hardcore ARM CPU,
- Development of firmware and software to perform in-DOM pulse deconvolution,
- Development of firmware to support the higher density of channels per wire pair relative to the IceCube DOM.

### *11.2. Integration of PINGU Channels into IceCube Surface DAQ*

PINGU channels will be integrated into the IceCube data acquisition system as shown in Figure 40. The PINGU readout hub (StringHub) components are each connected to a string of PDOMs. They extract hit summaries (channel and time information, currently) from the stream of data buffers sent by the PDOMs and send them to a trigger unit. The trigger examines the stream of hits and identifies patterns of interest by sending a trigger to the Global Trigger unit which merges triggers from the sub-detectors overlapping in time. The global trigger signal is then sent to an Event Builder processor which requests the full readout data, including waveform information buffered in the hubs, in time windows around the triggers and packages this data into an event data structure on disk. The individual components, and their changes relative to IceCube entities are discussed in the following paragraphs.

#### *11.2.1. PDOM Communications System and Readout Electronics*

It is expected that between 4–8 PDOMs will share a common copper pair connection to the surface in order to reduce the cost and size of the surface-to-PDOM cables relative to the IceCube in-ice cable system. This is a two- to four-fold increase in the channel aggregation and will require upgraded communications firmware. At the same time it will be necessary to increase the density of the readout electronics in order to accomodate additional PINGU channels in the rackspace available in the IceCube Computing Laboratory. An improved readout system is currently being designed to meet these new requirements of PINGU and simulataneously profit from the opportunity to replace the aging electronics and associated computing of the existing readout subsystem, the DOMHub. The communications must be made compatible with existing IceCube channels to allow for a uniform deployment of readout hardware across all channels. Despite this requirement, it will be possible, via advanced protocol-discovery during the link negotiation phase to encompass the improved communications protocol of the PINGU channels using more robust phase-shift keying modulation techniques while still supporting the baseband signaling currently used in IceCube.

In addition to data communication, the IceCube and PINGU data transmission protocols are required to implement a mechanism for time translation between the local timestamps in the IceCube and PINGU DOMs and the globally referenced time system UTC. In IceCube this mechanism is known as RAPCal and is fully documented in [102]. The corresponding solution for PINGU DOMs is currently under design with requirements for

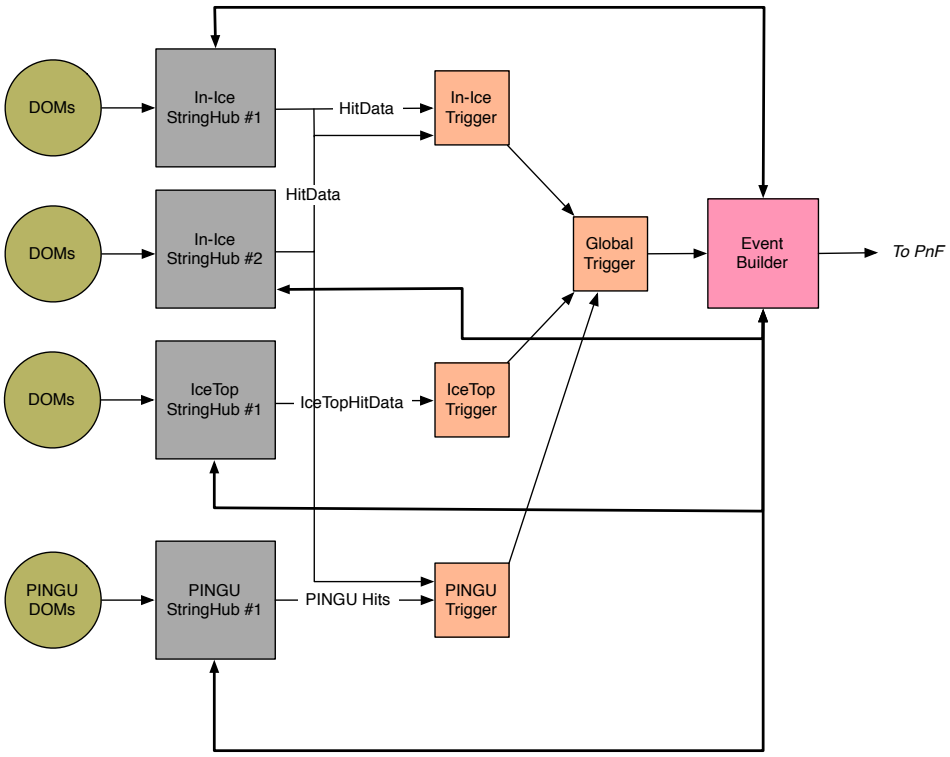


Figure 40: Schematic representation of the integration of the PINGU digital optical module channels into the IceCube data acquisition system. At left are the optical modules (circles), an entire string of which are connected to data collection processes running on the readout computers (grey boxes). In IceCube there are 86 such entities corresponding to the deep ice modules and another 11 entities for the IceTop surface channels. From software there is no limitation to the number of readout hosts in the system. The StringHub readout processors forward optical module hit summaries to the trigger processors which may, upon detection of an interesting hit pattern, request a readout of all hits in the detector in a given time window around the trigger time. Although the PINGU trigger is shown in this schematic operating only on hits from the new, PINGU DOMs, trigger processors could also operate on hits from PINGU and the existing IceCube DeepCore DOMs in combination. Each global trigger results in an event being built by the Event Builder. These events are then sent to the Processing and Filtering (PnF) farm at the South Pole for initial reconstruction and data reduction.

the same or better time resolution with respect to RAPCal (less than 5 ns) and which loosens the cable crosstalk specification. With the above-mentioned phase-shift keying modulation schemes, pseudo clock recovery can be implemented.

At the application level, the PINGU readout hubs should function nearly identically to those of IceCube: each hub collects and buffers data, sending pulse hit summaries to the trigger processors. The notable extension to the functionality concerns tagging which hits to send to the triggers. Due to past computing limitations in sending the full 2.5 MHz rate of hits to the triggers, only hits tagged with local coincidence triggers in the ice are forwarded to the triggers. This reduces the rate of hits into the triggers to approximately 50 kHz. Recent improvements in both the computing hardware and the IceCube DAQ will support hit sorting and triggering at the expected aggregate PINGU hit rate of 2 MHz.

### *11.2.2. Triggers*

The DAQ layout depicted in Figure 40 explicitly separates the PINGU trigger processor from the IceCube trigger processor, providing a degree of isolation between the two triggers. Development of another trigger processor specific to PINGU is the only infrastructure development forseen at the DAQ trigger infrastructure level. These modifications are minimal and only involve adding additional bookkeeping data structures to the trigger code. While existing DAQ trigger algorithms can be re-parameterized and used in PINGU, new trigger algorithms will also likely be developed to fully exploit the capabilities of the new subdetector. It is also possible that the PINGU triggering could operate as one or more trigger algorithms within the In-Ice Trigger unit. This latter configuration has the advantage that a single trigger can combine information from IceCube and PINGU channels to form a trigger.

No additional work is needed on the Global Trigger.

## *11.3. Event Builder*

The Event Builder interacts with the readout computers through a rather simple network interface. Any PINGU readout hub properly implementing this interface will participate correctly in the event assembly process. As such, there are no customizations needed in the Event Builder for PINGU deployment.

## 12. Calibration

### *12.1. Overview*

PINGU event reconstruction uses the timing, location, and amount of deposited light in an event to reconstruct the properties of the incident particle: position, time, direction and energy. As discussed in Section 4.1.3, detector-related systematic effects have a smaller impact on the hierarchy measurement than physics-related systematic effects such as uncertainties in oscillation parameters. The most important detector systematics are those which impact the determination of the energy scale, especially the pDOM sensitivity and the propagation of light in ice. To provide a proper baseline for physics analyses, PINGU will carry out an independent, detailed calibration program to measure detector geometry, optical response of PINGU DOMs, and properties of the ice in which PINGU is deployed. The high-level physics analysis will then allow for and constrain systematic deviations from this baseline that could influence energy or angular response. While these constraints are already expected to be quite precise, comparison of any deviations with known detector-level uncertainties will serve as an independent check and add confidence to results.

In order to achieve the targeted precision, PINGU will build on the extensive calibration experience gained in IceCube, using light-emitting calibration devices built into each DOM, other calibration light sources within PINGU, and muons induced by cosmic ray air showers. PINGU will improve on IceCube's measurements of DOM response and calibration light source output in the lab in order to more accurately describe the response of pDOMs in the ice and better quantify systematic uncertainties from pDOM sensitivity and light propagation in ice. The following sections will summarize the expected uncertainty on low level detector quantities and planned improvements in the design of PINGU light sources.

### *12.2. Calibration of Low Level Detector Quantities*

#### *12.2.1. Timing*

PINGU DOMs will use a similar time calibration system to IceCube, whereby reciprocal pulses are sent between the free-running clock in the pDOM and the master clock on the surface, resulting in a time synchronization across the detector of 3 ns or better [27]. This timing calibration system will run continuously during data acquisition. Calibration

light sources with known timing will be used during commissioning to test that times are accurately recorded and transmitted through the offline software chain.

### *12.2.2. Detector Geometry*

The position of IceCube DOMs have been measured to within 1 m with several methods, which we will also use in PINGU. During pDOM deployment, the position of strings will be surveyed and the absolute depth of the pDOMs will be estimated using data from the drilling process and pressure sensors attached to the bottom of each string. The vertical distance between pDOMs will be measured with a laser ranger or similar device during deployment, and will be corrected for possible cable stretching. Corrections to these methods will be applied using *in situ* light sources to triangulate the final position of modules in the ice. IceCube also includes several DOMs with onboard inclinometers to measure possible differential ice flow which would cause time-dependent changes in the detector geometry; such devices may also be installed in PINGU.

### *12.2.3. Direction*

IceCube has measured a deficit of multi-TeV cosmic rays from the direction of the Moon, thus demonstrating the ability to locate a point source in the sky to within 1° [103]. Due to its smaller size, PINGU may not have sufficient statistics to measure the moon shadow within a year, but muons which trigger both IceCube and PINGU can be used to compare PINGU's directional reconstruction to that of IceCube. Direction reconstruction at energies below the IceCube trigger threshold will be determined with Monte Carlo.

### *12.2.4. DOM Response*

The DOM response to light depends on the inherent efficiency of the PMT, the optical properties of the DOM housing and the optical properties of the ice itself. The effective mean single photon detection efficiency in IceCube DOMs, incorporating all of these effects, is currently known to better than 10%. PINGU's goal is to improve this measurement to better than 5%. In order to achieve this goal, the pDOM sensitivity, light source output and optical properties of the ice will be measured independently in PINGU and then verified in a combined check where each calibration light source yields the predicted response in all surrounding pDOMs. Based on existing studies in IceCube, the use of selected high quality low energy (close to minimum ionizing) muons is expected to allow

measuring the absolute sensitivity of DOMs independently to precision better than 5%. The independent measurements of pDOM sensitivity and light source intensity will be performed in the lab, before shipping and deployment in ice. In particular, the sensitivity of a selected subset of pDOMs will be thoroughly characterized as a function of wavelength and angle, with illumination and detection angles varied by rotation of pDOMs in a water tank. To transfer this detailed characterization to the full population, all pDOMs will undergo a time-efficient testing process similar to that which was used in IceCube [27], but with increased emphasis on angular and wavelength dependences.

The angular dependence of the sensitivity can be affected by the hole ice, which is melted and refrozen during module deployment, as illustrated in Figure 41. Bubbles and fissures which form during refreezing introduce additional scattering. This scattering modulates the DOM's angular sensitivity compared to nominal laboratory values as shown in Figure 42 [2]. The degassing process planned for PINGU deployments (see Section 10) is intended to reduce or eliminate this phenomenon, consequently the response in ice would closely match the measurement in the lab. The calibration light sources will be designed to allow verification and measurement of any remaining effect *in situ*.

Precise measurement of common multi-photon signals also takes into account the gains of the PMT, preamplifier and ADC; these will be well calibrated by the same procedure as that used in IceCube, using responses to single photons and an onboard pulser.

#### *12.2.5. Bulk Ice Properties*

PINGU, like IceCube, uses the Antarctic ice as a calorimeter. The amount of light deposited in the DOMs is correlated with the energy released by the particle interaction. IceCube measurements have shown that the scattering and absorption properties of the bulk ice between the holes are highly location-dependent. Concentrations of dust in the ice vary with depth, creating approximately horizontal layers. These dust layers are not perfectly horizontal, therefore the concentration of dust at a given depth for one string can differ from the concentration of dust at the same depth for another string. Both the absorption and scattering lengths of the ice track the dust concentrations. Additionally, the strength of scattering in the ice appears to be anisotropic with respect to the azimuthal angle of the photon direction [104]. IceCube uses both muons and *in situ* light sources to measure the properties of the ice. By comparing signals in DOMs at different distances and directions, the ice properties can be determined independently of the originating light source intensity. Currently the scattering and absorption in IceCube are measured to within 10% [2]. The goal of PINGU ice properties calibration is to improve

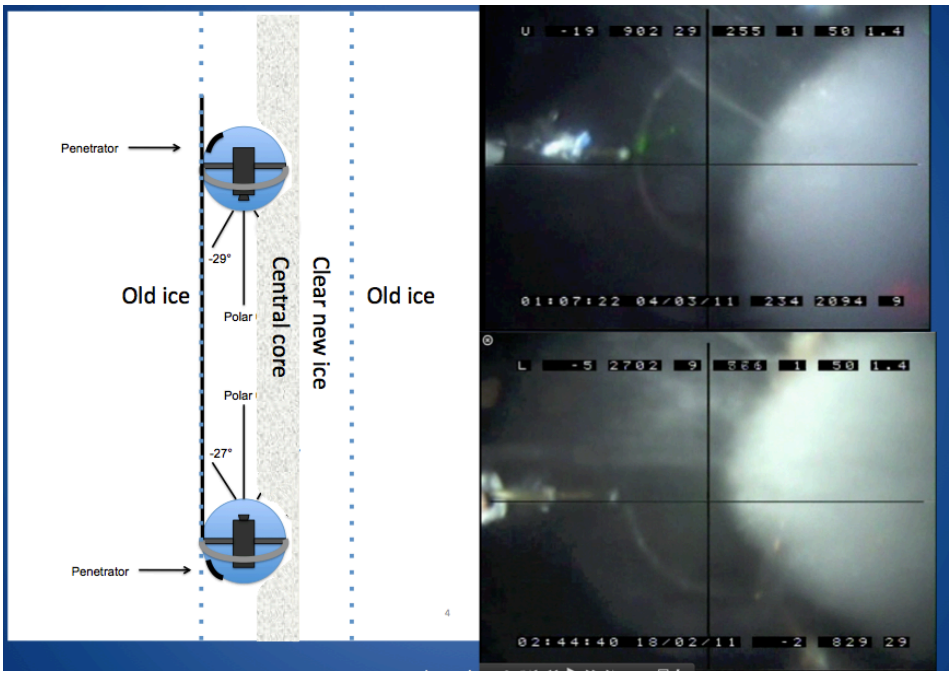


Figure 41: Left: sketch of refrozen hole ice showing an inner column with increased scattering due to bubbles. Right: photograph of hole ice in IceCube at approximately 2500 m depth.

that measurement to better than 3%. PINGU will measure the scattering and absorption lengths and characterize the scattering function at shorter distances than IceCube due to the closer spacing of PINGU DOMs, thus decreasing the effect of uncertainty on ice properties. The effects of the measured uncertainty will then be simulated to determine the overall effect on the energy scale uncertainty for the neutrino mass hierarchy measurement and other PINGU physics analyses.

### *12.3. Calibration Light Sources*

The accomplishment of PINGU's calibration goals requires improvements over the IceCube flasher design. Muons from cosmic ray interactions, signal sources which do not introduce extraneous light into the detector, will be used for both calibration, and monitoring of the detector during steady-state physics data taking. Calibration light sources with known properties will also be installed with PINGU. In order to measure the highly position-dependent ice properties, these calibration sources should be co-located with all PINGU DOMs. The primary calibration source will be LED "flashers" similar to those

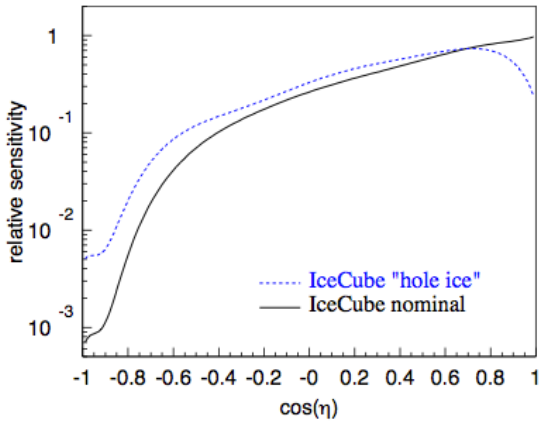


Figure 42: IceCube DOM sensitivity as a function of angular distance from the PMT axis. Black: nominal value from lab measurement. Blue: modified value including effects of hole ice.

present on all IceCube DOMs. These flashers are versatile devices with a range of settings which can be used to measure ice properties, pDOM sensitivity, timing, orientation and the coordinates of deployed modules. IceCube LEDs have proven to be very useful, but there are several improvements planned for both the design and characterization of PINGU light sources in order to achieve the desired calibration goals. A conceptual sketch of upgraded PINGU flashers is shown in Figure 43. An extensive simulation effort is currently underway to optimize the properties of the flashers.

- **LED light output**: Individual LEDs in IceCube show a spread of 20% around the average value in brightness. PINGU flashers will be individually calibrated during DOM production so that the brightness of each LED is known to within better than 3%. Photodiode monitoring of the LEDs on the control board will increase confidence in the calibration results and allow for better control of the brightness settings, especially at low light levels, which will be necessary in order to measure the ice properties across the short distances between PINGU DOMs. A preliminary high precision measurement of IceCube LED light output, using a NIST calibrated photodiode, shows that the overall light output can be measured to better than 3% if the angular emission pattern is well understood.

- **LED pulse timing profile**: In IceCube, the minimum LED pulse width is 7 ns. In order to measure the scattering function more precisely over short distances, the LED pulse width should be reduced below 2 ns so that the time behavior of the

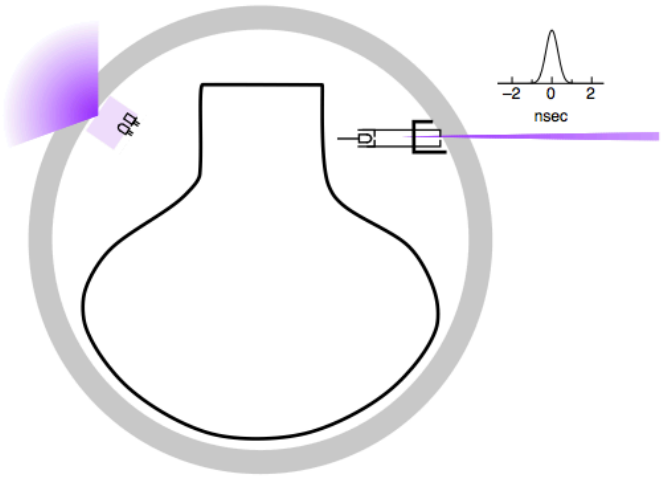


Figure 43: An upgraded PINGU DOM with flashers.

received light is almost entirely due to scattering rather than the source pulse shape. R&D efforts are underway to determine the feasibility of producing a 1 ns pulse in ice. Pulse widths of 3 ns have been produced in the lab using IceCube LEDs, and it is expected that widths of 1-2 ns can be achieved with updated hardware.

- **LED orientation**: IceCube LEDs are positioned at one of two zenith angle orientations: pointing horizontally outward (perpendicular to the cable) and pointing upwards at an angle of 45° above horizontal. Other angles are being investigated for PINGU flashers, such as flashers pointed straight upward or at a downward angle.

- **LED direction**: The orientation of the IceCube LEDs within a DOM is only known to within ±5°. A housing for the LED on the PINGU control board can control the direction to within 1°. The azimuthal LED orientations will be determined *in situ* using the observed light pattern in surrounding DOMs.

- **LED angular emission profile**: IceCube LEDs have a beam width of 10° in ice. Both wider and narrower beam widths are under investigation; a wide beam can be achieved by coupling the LED to a diffuser, and a narrow beam can be achieved by passing the LED light through a collimator. The LED emission pattern will be measured in the lab.

- **LED wavelength**: Most IceCube LEDs have a wavelength of 405 nm, with a few modules containing LEDs with wavelengths of 505, 450, 370 and 340 nm. PINGU DOMs may contain different wavelength LEDs in order to study the wavelength dependence of the ice properties and the DOM response in ice.

In addition to the all-purpose calibration flashers, we intend to deploy other special devices in selected locations. A high-resolution camera similar to one already deployed in IceCube will be deployed with at least one string to photograph the hole ice during and after refreeze. Comparison of PINGU hole ice photographs with photographs taken by IceCube will provide early data on the efficiency of the degassing and filtering program. We are also investigating the feasibility of generating a more comprehensive set of visual hole ice data via deployment of very low cost cameras in many or all PINGU DOMs.

A diffuse light source called the Precision Optical CAlibration Module (POCAM) is also under study. The purpose of the POCAM is to illuminate a large part of PINGU with a perfectly diffuse light source. The POCAM design under study, shown in Figure 44, includes

- A pulsed (nsec) light source, such as a single monochromatic LED equipped with a flat window or a multi-wavelength matrix of LEDs
- A sensitivity-calibrated photodiode to monitor the pulsed emission of the POCAM light *in situ* at the 1-2% precision level.
- A diffusing sphere. A series of ports will be created on the sphere to act as *in situ* precisely calibrated identical light sources. The light falling on the photodiode will be geometrically proportional to the light emitted from the ports on the sphere, providing a constant monitor of the light intensity.

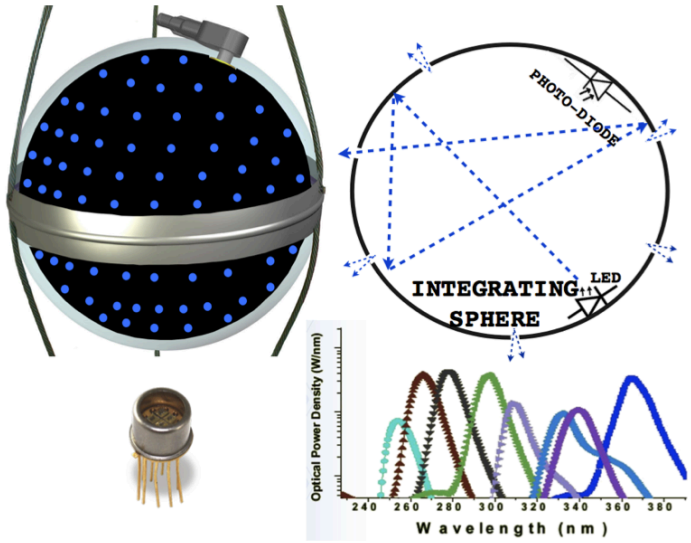


Figure 44: POCAM configuration under study, including spectrum of multiwavelength LED light source.

## 13. Monte Carlo Simulation Software

Simulations of the PINGU detector have been carried out using the Monte Carlo tools developed for the IceCube experiment. The strong similarities between the IceCube and PINGU hardware allow us to capitalize on the extensive efforts which have gone into refining the IceCube simulation model of both the Antarctic ice and also the hardware response. However, some modifications to the standard IceCube tools were necessary to produce reliable simulations of neutrino interactions in the range of 1-20 GeV, and some recent technical changes to the IceCube simulation tools are not extensively documented elsewhere, so a brief synopsis of the simulation tools is given here.

### *13.1. Neutrino Event Generator*

Although most high-energy IceCube neutrino simulations rely on the NuGen event generator (based on ANIS [105]), simulations of neutrinos interacting in the PINGU detector are based on the GENIE Neutrino Monte Carlo generator [106], which is used extensively in the accelerator-based neutrino physics community. GENIE conducts a full simulation of the neutrino-nucleon interaction, and produces a list of secondary particles exiting from the interaction vertex, modeling intranuclear interactions where necessary. All neutrino interaction channels are modeled by GENIE, although the bulk of the events detected by PINGU arise from deep inelastic scattering (DIS).

A wrapper was created to embed this package within the IceCube software framework. Events are generated isotropically from a user-defined power law distribution (normally $E^{-2}$) and can be reweighted to reproduce the atmospheric neutrino spectrum [35]. A newer atmospheric model was specifically developed for use at the South Pole [107] in order to accurately incorporate the Earth's geomagnetic effects on the arrival directions of neutrinos. The asymmetry in the flux as a function of azimuth and zenith starts at $\sim 10$ GeV and becomes more pronounced at lower energies. While a rewrite of the weighting software which incorporates the asymmetry is underway, an average flux over the full azimuth range was used to produce an atmopsheric neutrino flux value. This reweighting procedure permits rapid assessment of the impact of uncertainties in the true flux and spectrum of the atmospheric neutrinos. Although GENIE permits extensive modeling of the uncertainties surrounding the neutrino interaction physics, previous DeepCore analyses have shown that these uncertainties are largely degenerate in the DIS regime with variations of the atmospheric flux normalization and spectrum, and were therefore not evaluated separately.

To improve performance, neutrino interactions simulated outside of a cylinder of 200 m radius and 500 m height, centered on PINGU, are discarded at the outset. Because the atmospheric muon veto is extremely effective at rejecting particles originating outside of the PINGU fiducial volume, the reduction in neutrino rate at the analysis level introduced by this approximation should be negligible.

### *13.2. Atmospheric Muon Event Generators*

Computational resource limitations do not permit generation of event samples comparable to the expected atmospheric muon rates, so we rely primarily on the demonstrated muon rejection performance of the IceCube DeepCore detector to support our estimates of muon background rates. Because the outermost DeepCore instrumentation, which is deployed in the extremely clear ice below about 2100 m depth, will be used to reinforce the muon veto provided by the main IceCube detector, this estimate should be strongly conservative. Accordingly, our neutrino efficiencies are calculated by applying slightly modified DeepCore event selection routines to our simulated neutrino events, and the atmospheric muon samples produced for PINGU are primarily intended to confirm that these event selections behave as expected.

Two methods were used to produce samples of the atmospheric muon background. The first utilized full Corsika simulation of air showers produced by cosmic rays incident on the upper atmosphere, tracking the muons produced in such air showers to the PINGU detector. The second, known as the "muon gun," parametrizes the angular and energy distributions of the muons produced in the Corsika simulations and injected muons from a half-sphere extending just outside the IceCube detector volume.

### *13.3. Particle Propagation*

The relativistic particles produced at a GENIE neutrino interaction vertex were tracked by GEANT4 until they, and any daughter particles produced, fell below the Cherenkov threshold. All of the Cherenkov photons produced were stored for later propagation through the ice by a separate simulation program. This provides a more detailed model of the light emission from the neutrino interaction vertex than the standard IceCube tools, which relies instead on parametrized descriptions of prototypical hadronic and electromagnetc showers. Atmospheric muons traveling through the detector were modeled using the standard IceCube particle propagator MMC [108], instead of GEANT4.

### *13.4. Light Propagation*

Once the relativistic particles were propagated through the detector volume by GEANT4 or MMC, the Cherenkov photons produced were tracked by the IceCube software tool "clsim." This is a parallelized, GPU-based software package which permits full treatment of photon propagation throughout the extremely large volume occupied by IceCube. The depth-dependent optical properties of the Antarctic ice have been extensively studied by the IceCube Collaboration, and the full details of this optical model [2] were included. At each propagation step, photon scattering is modeled by numerical approximations to the Mie scattering function, as developed and tuned by IceCube.

### *13.5. Detector Response*

The main optical elements of the planned PINGU DOMs are identical to those used in DeepCore, so the detector response modeling of the DOMs was used without modification (except that an average calibration function was used for each DOM, rather than the individualized DOM models used in IceCube simulations). Recent studies of dark noise in IceCube have shown that there is a significant non-Poissonian component to the DOM noise, possibly arising from scintillation in the pressure glass or the PMT glass at very low temperatures; this effect was included in the detector simulation.

Although the digitization electronics used in PINGU will differ from the IceCube and DeepCore design, no modifications were made to the simulation software. The dynamic range of PINGU may be slightly narrower, but given the much lower energy range of the neutrinos of interest, saturation of the PINGU electronics should be rare for events of interest. The timing resolution of the PINGU electronics will be similar to that of IceCube, so the photon timing and pulse resolution should be similar. The PINGU electronics, based on fast ADCs, will provide this timing resolution over the full event time range without deadtime, whereas the IceCube electronics occasionally need to fall back on a slower FADC with coarser timing resolution.

In IceCube and DeepCore, data rates from individual DOMs are reduced by imposition of a local coincidence in hardware. If neighboring DOMs also detect light, a full data record is transmitted to the surface; otherwise, only a brief summary record is sent. No dedicated local coincidence circuitry is planned for PINGU, but we anticipate that faster FADCs, onboard photoelectron pulse extraction in FPGAs, and string-level software coincidence logic at the surface will allow us to fit PINGU data within the available cable bandwidth.

Again, to the extent that the PINGU hardware differs from the model used in simulation, the additional flexibility in software-based coincidence logic will only improve PINGU performance over the model used in simulation. We therefore have a high degree of confidence in our simulation of PINGU.

The trigger rate in DeepCore is quite low, demanding only three close-neighbor DOMs with locally-coincident hits within a time window of a 2.5 microseconds. Although this threshold may not be feasible given the much higher number of DOMs in PINGU, very few simulated neutrino events near the trigger threshold survive the relatively strict event selection applied to neutrino events used in the performance studies presented here. We anticipate that the inclusion of spatial, as well as timing, information into the PINGU trigger will permit use of trigger algorithms which would record all of the events used in these studies.

## 14. New Photon Detection Technologies

Given the superb properties of Antarctic ice, a megaton-scale detector with sensitivity to events at and below the GeV energy scale may be feasible in the future. Such a detector would provide sensitivity to proton decay and bursts of supernova neutrinos from nearby galaxies [109]. In order to reconstruct Cherenkov rings and strongly reduce backgrounds by coincidences, new photodetectors, providing a substantially larger photosensor coverage than IceCube DOMs, need to be developed. Such detectors may also provide a cost-efficient technology for high-energy extensions. The PINGU installation will allow us to co-deploy a selected set of new photon detection instruments, which subsequently will be calibrated and tested using the IceCube infrastructure. R&D efforts so far focus on the following directions:

- multi-PMT optical modules with increased photodetection sensitivity, directional information and precision timing and
- low noise, UV transparent, wavelength shifting, large area modules with relaxed timing requirements.

Both efforts take advantage of the excellent properties of Antarctic ice: low temperature, radioactivity and little absorption above UV wavelengths of 200 nm. To exploit the complementarity of the technologies, they may eventually be combined in a suitable way.

### *14.1. Wavelength-Shifter Optical Modules (WOMs)*

The size and energy threshold of future neutrino detectors are limited by the affordability of photosensitive area, where the main cost arises due to the PMTs. For the detection of low energy neutrino interactions, as from distant supernovae, very low noise is a deciding factor. One way to provide a cost reduction and low noise is the use of wavelength shifting and light guiding materials to concentrate the light onto one or a few PMTs with small photocathode area. The goal of the R&D project is to provide modules with the following properties:

- very low noise rates in the order of 10 Hz or below,
- UV sensitivity,

- large geometric acceptance and module sensitivity,
- long term stability,
- no necessity for magnetic shielding and
- adaquate timing resolution.

The main idea of the WOM is to increase the sensitive area of a PMT by using passive components that act as light collectors and concentrators (a sketch of the module is shown in Fig. 45). The required techniques and prototypes of wavelength shifting optical modules are under development at the University of Bonn with support by the JGU Mainz. The goal is to maximize the collection area for cigar-shaped modules that safely withstand high pressure, can be handled easily and may be produced at a price per photosensitive area, that is lower than that for standard optical modules. The current status of the R&D efforts on various components is discussed below.

**Housing:** In order to provide sensitivity at wavelengths below 300 nm and to suppress noise arising from radioactivity in the glass, quartz tubes of suitable dimensions have been investigated. An R&D project with the glass vessel manufacturer Nautilus GmbH resulted in a technical solution which, according to the manufacturer specifications and calculations performed at JGU, fulfills the requirements on pressure resistence. The design is a resonable compromise, taking into account weight, achievable dimensional accuracy and costs and consists of industrial fused silica tubes with 9 mm thickness, 114 mm diameter and 1200 mm length with hemispherical borosilicate caps. In total six modules were fabricated. In principle and if desired, the length of the modules could be extended by connecting additional glass tubes with stainless steel support rings that are glued to the rims of the glass cylinders.

**Wavelength shifting cylinder:** A wavelength shifting and lightguiding cylindrical tube, with a diameter to allow only for a small air gap between the tube and the pressure vessel, provides the optimal geometry for light concentration. In order to enhance the performance towards the UV, transparent tubes are coated with a thin film containing the fluorescent dye. Cherenkov photons, peaking in the UV, are absorbed and re-emitted isotropically at larger wavelength with a large fraction (up to 75%) guided towards the end via multiple total internal reflection. The tube material can be made of quartz glass, high quality PMMA or PVT. The thin films are produced through dip-coating techniques, where a range of dyes and host materials are currently being tested for optimal light yield, durability and long term stability.

**PMT and readout:** On both ends of the tube, the light is guided to the spherical surface of a PMT through adiabatic light guides, which are currently under development at the University of Bonn. The PMT diameter can be 2 inch or smaller and should have large sensitivity around the peak emission wavelength around 450 nm. The optimal choice for the PMT depends thereby on the choice of dye and tube thickness. The readout electronics for the PMT will be based on that developed for the PDOM altered to match the smaller dimensions of the housing.

**System performance:** Different wavelength-shifting materials have been tested in lab measurements as candidates for use in such a sensor. Photon capture efficiencies as high as 50% have been achieved. Based on these findings, we estimate that the effective photosensitive area of a prototype built with existing technology can easily exceed that of modules currently used *e.g.,* in IceCube. Additionally, the dark noise rate of such a module can be exceptionally low in the order of 10 Hz [110].

### *14.2. Multi-PMT Optical Modules (mDOMs)*

Current large volume Cherenkov neutrino telescopes use optical modules consisting of a spherical glass pressure vessel containing one large PMT, as well as front-end and digitization electronics. In contrast, multi-PMT optical modules [111], first developed for the future KM3NeT neutrino telescope in the Mediterranean Sea, house arrays of several small PMTs and their read-out electronics. Such modules offer a number of attractive advantages compared to the conventional layout:

- increased photocathode area with almost $4\pi$ acceptance,
- coincidence recognition,
- improved event reconstruction and background suppression due to directional sensitivity, as well as
- superior timing without a need for magnetic shielding.

The group at the University of Erlangen (ECAP) extended the KM3NeT spherical multi-PMT concept by incorporating 41 three-inch PMTs in a cylindrical layout with hemispherical caps. The goal is to achieve a similar price per cathode area as in conventional optical modules. The status of the R&D and prototyping efforts is discussed below.

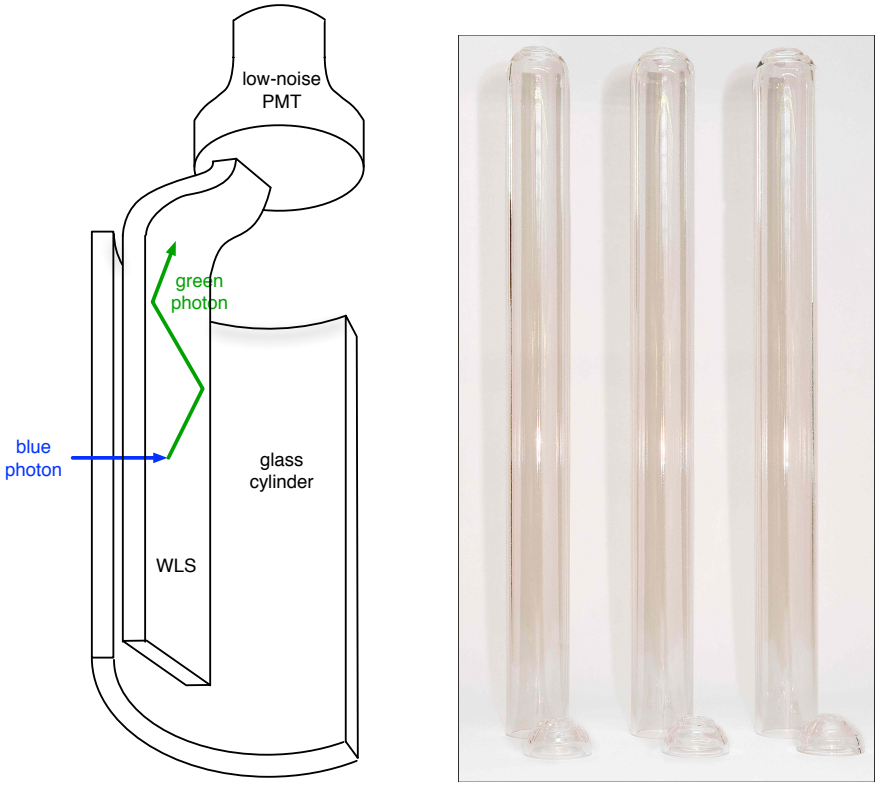


Figure 45: Left: Concept of the wavelength shifting optical module. Quartz pressure vessels with 114 mm outer diameter and 1200 mm length.

**Housing:** Unlike glass spheres, cylindrical pressure vessels are not commercially available in the appropriate size and pressure rating. Negotiations with a glass vessel manufacturer (Nautilus GmbH) have resulted in a technical solution which, according to the manufacturer specifications and finite-element calculations performed at ECAP, fulfills the requirements. A set of such vessels has been purchased for testing and prototyping. The pressure vessel consists of two cylindrical parts with hemispherical caps (see Fig. 46). The two segments are joined centrally by stainless steel flanges glued to the rims of the glass components. These ring structures improve the overall stability and can be used for mounting a PMT holding structure inside the vessel. Given the dimensions of currently available PMT prototypes, one segment is able to house 21 three-inch PMTs. The overall length (and thus the total photocathode area) of the module can in principle be enhanced by adding further cylindrical segments at the center.

**PMTs:** At the time of this writing, two companies (Hamamatsu and ET Enterprises) provide three-inch PMT prototypes that were optimized for KM3NeT w.r.t. to length ( $< 12$ cm), transit time spread (RMS $< 2$ ns) as well as other parameters. These PMTs are also considered for the use in the PINGU module (see Fig. 47). Their mushroom-shaped entrance windows offer superior timing and 10 dynodes provide the required gain. The ET Enterprise D792KFL has a slightly larger photo-cathode area than the Hamamatsu R12199-02 model and is shorter, which is favorable for the use in densely packed mDOMs. The noise rates are estimated to be below 200 Hz.

**Support structure:** The PMTs (and possibly calibration devices) will be suspended using a support structure that has to provide temperature resistance, limited shrinkage due to pressure and temperature, negligible chemical reactivity with PMT glass and optical silicon gel, low intrinsic radioactivity, and durability throughout the lifetime of the experiment. In the case of KM3NeT, the holding structure is currently produced by rapid prototyping ("three-dimensional printing"). This technique was found to be most flexible and cost-effective during the prototyping phase. ECAP recently acquired a rapid prototyping device and has run tests to gain experience with the technique. For mass production, alternative, more cost-effective production methods are also investigated.

**Readout electronics:** The readout electronics will be based on the KM3NeT layout. The analogue waveform produced by the PMT is converted to a time-over-threshold step function via a base-borne ASIC. This signal is collected, sent to the main logic board featuring an FPGA and a synchronized clock with a TDC unit, and is subsequently digitized. The development of a PINGU interface is ongoing. The total energy consumption of the mDOM is estimated to be below 9 W and the required bandwidth should be less than 175 kBytes/s.

**Current project status:** Parts for the construction of three glass vessels have been acquired. Three-inch PMT prototypes from both manufacturers, together with corresponding active bases from NIKHEF, are available at Erlangen and will be incorporated in the mDOM prototypes. A low-temperature test bench is under construction to measure properties crucial for the use in deep ice, such as the dark rate, under realistic conditions (down to -30° C). Simulations currently undertaken address the optical properties of the module and the impact of the utilization of mDOMs on the performance of a detector array, in particular for the detection of proton decays. The design of the PMT supporting framework, incorporating the experience gained from first KM3NeT layouts, is in progress. The possibility of fabricating the support structure (in parts or in total) with ECAP's in-house printer for cost reduction is also investigated.

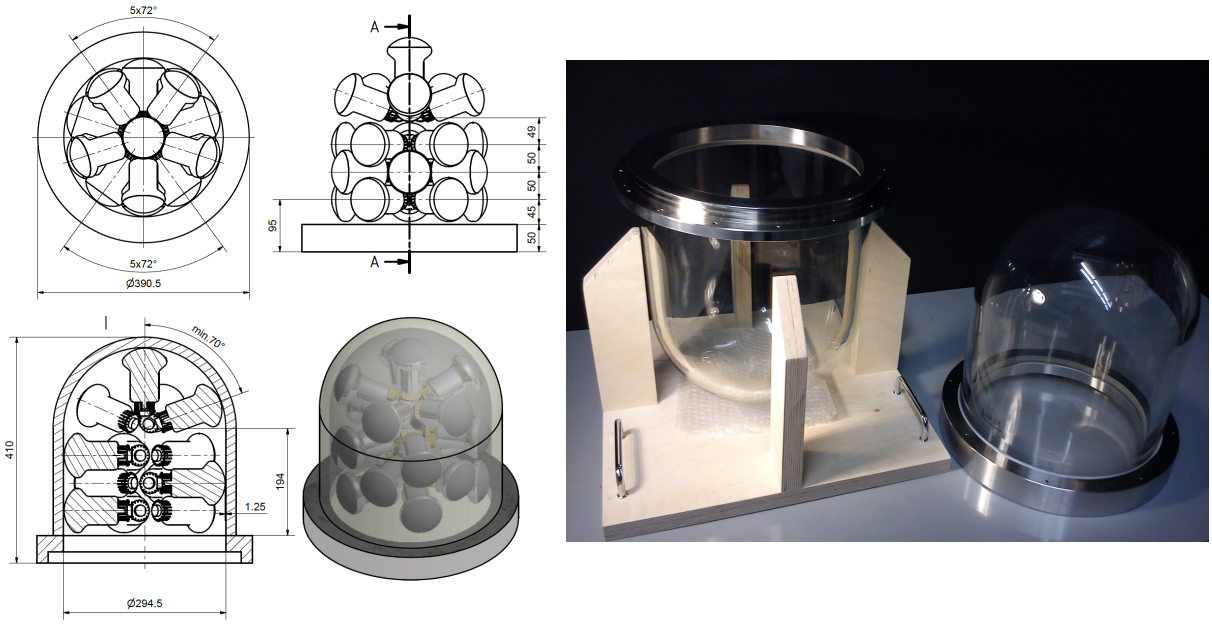


Figure 46: Left: Technical drawing of the current layout for the PINGU multi-PMT optical module. Dimensions given in mm. Right: Borosilicate vessel components available at Erlangen.

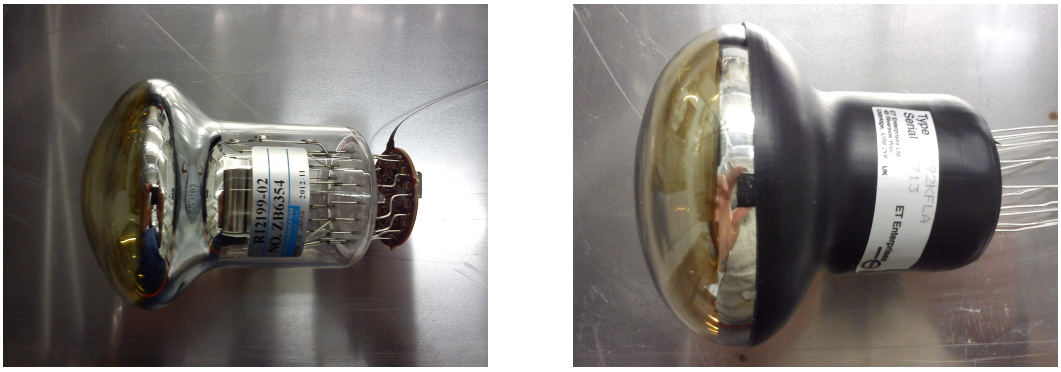


Figure 47: Left: R12199-02 is the most recent three-inch PMT prototype by Hamamatsu for the KM3NeT optical module. Right: D792KFL is the current ETL-Enterprise prototype.

## 15. Schedule and Cost

The proposed schedule for PINGU is largely based on the successful construction of IceCube. IceCube was completed on time and on budget over a 10 year period which included eight seasons of construction and installation at the South Pole starting in the austral summer of 2003/2004. IceCube construction was completed in January, 2011. The plan for the construction schedule of PINGU incorporates knowledge obtained from IceCube along with considerations related to the length of time between IceCube completion and the start of PINGU. The schedule for PINGU is broadly broken into the following sequence:

| | |
|---|---|
| PINGU R&D and Verification activities | October, 2014 to March, 2017 |
| PINGU Procurement | March, 2016 to June, 2019 |
| PINGU Instrumentation Production | June, 2016 to August, 2019 |
| PINGU Drilling and Installation | November, 2017 to January, 2020 |

PINGU will take approximately five years to build over six calendar years. The schedule does not currently take into account possible funding constraints related to federal budget years which begin each October.

PINGU construction, managed via a Work Breakdown Structure (WBS, see below) will use a series of milestones to track high level progress with respect to schedule that culminate in specific reviews, including the Preliminary Design Review (PDR), Final Design Review (FDR) and Production Readiness Review (PRR). After the funding is awarded, the first milestone will be a PDR and in the current timeline this is scheduled for June, 2015. The purpose of this PDR will be to verify the feasibility of the design of the Level 2 WBS deliverables of Drilling, PDOM, Cable Systems, Surface Instrumentation and Calibration.

Following a successful PDR, preparation will begin for subsequent FDRs to be held for the PDOM, Cable, Surface Instrumentation and Calibration systems. FDRs are formal processes and all documentation required for initiating the Procurement Process must be complete. This includes technical specifications, 3-d modeling drawings, and a completed Design Verification Report which shows that the design meets originally documented design requirements. We note that the IceCube supplier of raw cable, Ericsson, will potentially not be available to PINGU, and this introduces some technical risk to the project. A plan to mitigate this risk includes moving the design activities related to Cable Systems earlier so that procurement and production may also begin earlier. Similarly,

new design elements for the PDOM also increase the technical risk and the FDRs are planned for Spring 2016. This permits a start of procurement for these elements almost immediately and production of the Cable System to start in August 2016. The expected cable cycle time is four months per string, comparable to actual cable production for IceCube. FDRs to be held for the Surface Instrumentation and Calibration systems are currently planned for Summer 2017.

Once FDRs are complete, procurement can begin in earnest. The balance of 2016 will be allocated for the generation of Requests for Proposals (RFPs), contract negotiation and supplier award. Suppliers would ramp up production for delivery of components starting in early 2017. This is an aggressive time scale and will depend on the cooperation of the funding agencies and Purchasing Departments in the relevant institutions, but we aim to avoid underestimating the time required for successful procurement.

The PRR for PDOM, Surface Instrumentation and Calibration systems is scheduled for February, 2017. The PRR establishes that the project is ready for a sustained effort to integrate, test and deliver all needed instrumentation for the project. Manpower, materials and supplies, capital equipment deliveries, production documentation, jigs and equipment and facilities are all reviewed prior to the start of production. The start of PDOM production is planned for March, 2017 with an expected rate of 24 PDOMs per week. The production is assumed to take place at single facility located at the Physical Sciences Laboratory (PSL) (UW–Madison) in Stoughton, Wisconsin. PSL successfully integrated and tested approximately 3500 Digital Optical Modules for IceCube from 2004 to 2009. Physical infrastructure, along with key personnel, remains at PSL making this a low risk choice for a PDOM production facility.

The first scheduled PDOM deployment season for PINGU will be the 2017/2018 Pole season. It is planned that six holes would be drilled in this initial season. To accommodate a potentially faster drilling schedule, eight complete strings of instrumentation will ship from PSL and the associated Cable System production site no later than September, 2017 to meet Polar Program logistics requirements. Instrumentation production would take place continuously until August, 2019 to accommodate the deployment of 16 additional holes of detectors in the 2018/2019 Pole season and the final 18 holes in the 2019/2020 season. Final string commissioning and IceCube integration would occur through March, 2020 when PINGU would be complete. A detailed schedule is shown in Fig. 48, broken down by WBS element.

As with the schedule estimates described above, the cost estimates for PINGU are largely

based on extensive experience obtained from IceCube construction. We have created a detailed WBS with the following top level task areas:

1. Project Office
2. Drilling
3. PDOM
4. Cable System
5. Surface Instrumentation
6. Calibration System
7. IceCube Integration
8. Polar Operations (except drilling)
9. Antarctic Support Contractor

A detailed bottoms-up estimate that extends three levels into the WBS, including inflation but not contingency, provides the initial estimated costs shown in Table 8. (A cost breakdown by WBS with and without contingency is shown in Table 9.) Table 8 also includes the estimated incremental costs of PINGU being a part of a large scale IceCube high energy extension of order 100 strings. It should be emphasized that the costs include polar support. The actual detector cost without polar support would be approximately \$17M less and only \$38M as part of a full IceCube upgrade. Without contingency the cost of a deployed string is about \$1.2M and \$1M for the scenarios of PINGU as a stand alone project and the full IceCube upgrade, respectively.

## 16. Underground Facilities in Antarctica

At the Amundsen-Scott South Pole Station, operated as a scientific facility on behalf of the National Science Foundation (NSF), astrophysical observations have been underway for several decades, and to date represent the majority of ground-based astrophysical work in Antarctica. Recent overviews of neutrino, cosmic ray and astronomy programs at the South Pole have been presented at a workshop in 2011 in Washington [112] and at the Symposium 288, *Astrophysics from Antarctica*, at the International Astronomical Union General Assembly [113].

### *16.1. Logistics – the South Pole Station Facility*

The Amundsen-Scott station provides excellent infrastructure for scientific activities at the South Pole, including the IceCube Laboratory (see Fig. 1) building that houses power,

| | Item | PINGU Alone (M$) | PINGU within larger upgrade (M$) |
|---|---|---|---|
| Fixed costs | PINGU project | 20.6 | 7.0 |
| Per-string costs | PINGU project | 46.9/40=1.17 | 41.3/40=1.03 |
| | Polar support | 17.4/40=0.44 | 16.45/40=0.41 |
| | Total | 1.61 | 1.44 |
| non-US cost | Total | 25 | 25 |
| US cost | Total (w/o contingency) | 20.6+(1.61*40)-25 = 59.9 | 7.0+(1.44*40)-25 = 39.8 |
| | Total (w/contingency) | 25.5+(1.98*40)-25 = 79.4 | 8.7+(1.77*40)-25 = 54.6 |

Table 8: Estimated costs for the construction of the baseline 40-string PINGU detector alone (left column) and as part of a large scale IceCube upgrade of order 100 strings for a high energy extension (right column). For the latter, PINGU benefits from sharing the costs of the drill upgrade, hardware development and logistics. Included are estimated costs that include contingency and contributions from foreign funding agencies.

| WBS Number | WBS Name | Total w/o Contin. ($M) | Estimated Contingency | Total with Contin. ($M) |
|---|---|---|---|---|
| 1.1 | Project Office | 6.3 | 16% | 7.4 |
| 1.2 | Drilling | 11.7 | 28% | 15.0 |
| 1.3 | PDOM | 19.7 | 25% | 24.6 |
| 1.4 | Cable System | 12.8 | 25% | 16.0 |
| 1.5 | Surface Instrumentation | 3.4 | 25% | 4.2 |
| 1.6 | Calibration System | 3.9 | 22% | 4.8 |
| 1.7 | IceCube Integration | 5.9 | 16% | 6.8 |
| 1.8 | Polar Operations (except drilling) | 3.6 | 16% | 4.2 |
| 1.1-8 | Subtotal | 67.5 | | 83.1 |
| 1.9 | Antarctic Support Contractor (ASC) | 17.4 | 22% | 21.2 |
| 1.1-9 | Grand Total | 84.8 | 23% | 104.3 |

Table 9: Estimated costs for the construction of the baseline 40-string PINGU detector alone, broken down by WBS element. No foreign funding agency contributions are included. Contingency is based on estimated risk factors at WBS Level 2.

communications, and data acquisition systems for IceCube. The new South Pole Station facility, shown in Fig. 49, had been largely completed by 2008, prior to the completion of IceCube in December, 2010. The realization of IceCube established the South Pole ice cap as an underground laboratory that is available as a resource for scientific endeavors beyond IceCube.

Personnel and cargo are transported to the South Pole primarily by ski-equipped LC-130 aircraft operated by the New York Air National Guard (Fig. 50). Cargo can also be delivered by surface transport traversing the ice from the Antarctic coast, but LC-130's are used for most scientific equipment. In 2012/13, more than 100 LC-130 missions were flown to South Pole, delivering 26,000 lb each. An ice traverse mission can deliver 750,000 lb of cargo.

The station is accessible by aircraft from approximately November through mid-February, supporting a summer population of approximately 160, including both scientists and support personnel. During the remainder of the year, the station is occupied by approximately 40 winter-over personnel. Scientists typically make up around 25-30% of the personnel on station.

IceCube uses 60 kW of power and has access to a bandwidth of more than 100 GB/day for data transmission and detector control. PINGU is estimated to require roughly an additional 20% of the power and 10% of the bandwidth of IceCube. The primary means of data transmission from the South Pole is via a TDRS satellite link maintained by the NSF. Power is provided by the station generators and is highly reliable – the IceCube detector has been operated with an uptime of approximately 99% and is maintained on a daily basis by winter-over scientists on site.

### *16.2. Detectors – IceCube and Future Possibilities*

The recent successful detection of high energy neutrinos of astrophysical origin by IceCube [1], as well as measurements of neutrino oscillations [3, 4] and searches for dark matter [5] with DeepCore, has led the IceCube Collaboration to investigate possible extensions of IceCube with improved performance at both high and low energy. At high energy, an expanded detector in the deep ice and an improved surface array for identifying the air showers that produce atmospheric neutrinos are under consideration. PINGU is designed as an integral component of IceCube, extending its scientific program to lower energies but using the same fundamental techniques and equipment as the high-energy

extensions. It would be fully integrated into the existing IceCube data acquisition system. The plan is to exploit the existing IceCube and DeepCore sensors to veto cosmic ray backgrounds and augment the data collected from PINGU's fiducial volume. The use of the same fundamental techniques and equipment for the installation of PINGU and the high-energy extensions offers substantial cost savings in development, installation and operations.

### *16.3. Drilling – Access to the Deep Ice*

Deployment of any of these new instruments requires drilling holes in the ice. In order to do this under the harsh conditions of the project site, IceCube designed and developed a special system – the Enhanced Hot Water Drill (EWHD) – which melts a column of liquid water into the ice sheet, allowing instrumentation to be inserted before the water re-freezes. IceCube was able to drill up to 20 holes in a construction season, which lasts about three months. Drilling a single 60-cm diameter hole to a depth of 2500 m took about 30 hrs.

The EWHD represents a substantial investment in design and equipment, and while recommissioning the EHWD in full strength would require some effort, the IceCube extensions benefit greatly from the possibility of leveraging the existing expertise and equipment. The installation costs of these detectors are relatively small compared to excavation costs of a large volume detector in an underground mine, and the technical and cost risks are low. There are also efficiencies of scale between PINGU and the high-energy extensions of IceCube.

### *16.4. Operations*

Like DeepCore and IceTop, PINGU is designed as a component of the larger IceCube instrument. In addition to efficiencies of scale in the cost of drill refurbishment and electronics development, this approach offers substantial savings in the areas of software development and operations. Although the in-situ electronics would be somewhat different from those used in the existing IceCube detector, to take advantage of advances over the past decade, the data arriving at the surface from both PINGU and the high energy extensions would be identical to that generated by IceCube, IceTop and DeepCore. Because IceCube's data acquisition system was designed to operate as a collection of subdetectors, only minor work would be needed to incorporate new components such

as PINGU into IceCube. Once the PINGU data is incorporated into the data acquisition system, it will automatically flow along with the existing IceCube data through the remainder of the data processing and archiving system. Because IceCube can serve as a veto for the cosmic ray muons which dominate the IceCube trigger rate, PINGU data will not substantially increase the IceCube data rate. The IceCube winter-over scientists would maintain the PINGU electronics and computing systems along with those of the existing IceCube detector and the other extensions targetting higher energies. The only additional costs associated with PINGU operations would arise from the need to archive additional PINGU data and to maintain specialized Monte Carlo simulations for the low-energy physics targetted by PINGU.

## 17. Acknowledgements

IceCube acknowledges the support from the following agencies: U.S. National Science Foundation-Office of Polar Programs, U.S. National Science Foundation-Physics Division, University of Wisconsin Alumni Research Foundation, the Grid Laboratory Of Wisconsin (GLOW) grid infrastructure at the University of Wisconsin - Madison, the Open Science Grid (OSG) grid infrastructure; U.S. Department of Energy, and National Energy Research Scientific Computing Center, the Louisiana Optical Network Initiative (LONI) grid computing resources; Natural Sciences and Engineering Research Council of Canada, WestGrid and Compute/Calcul Canada; Swedish Research Council, Swedish Polar Research Secretariat, Swedish National Infrastructure for Computing (SNIC), and Knut and Alice Wallenberg Foundation, Sweden; German Ministry for Education and Research (BMBF), Deutsche Forschungsgemeinschaft (DFG), Helmholtz Alliance for Astroparticle Physics (HAP), Research Department of Plasmas with Complex Interactions (Bochum), Germany; Fund for Scientific Research (FNRS-FWO), FWO Odysseus programme, Flanders Institute to encourage scientific and technological research in industry (IWT), Belgian Federal Science Policy Office (Belspo); University of Oxford, United Kingdom; Marsden Fund, New Zealand; Australian Research Council; Japan Society for Promotion of Science (JSPS); the Swiss National Science Foundation (SNSF), Switzerland; National Research Foundation of Korea (NRF); Danish National Research Foundation, Denmark (DNRF)

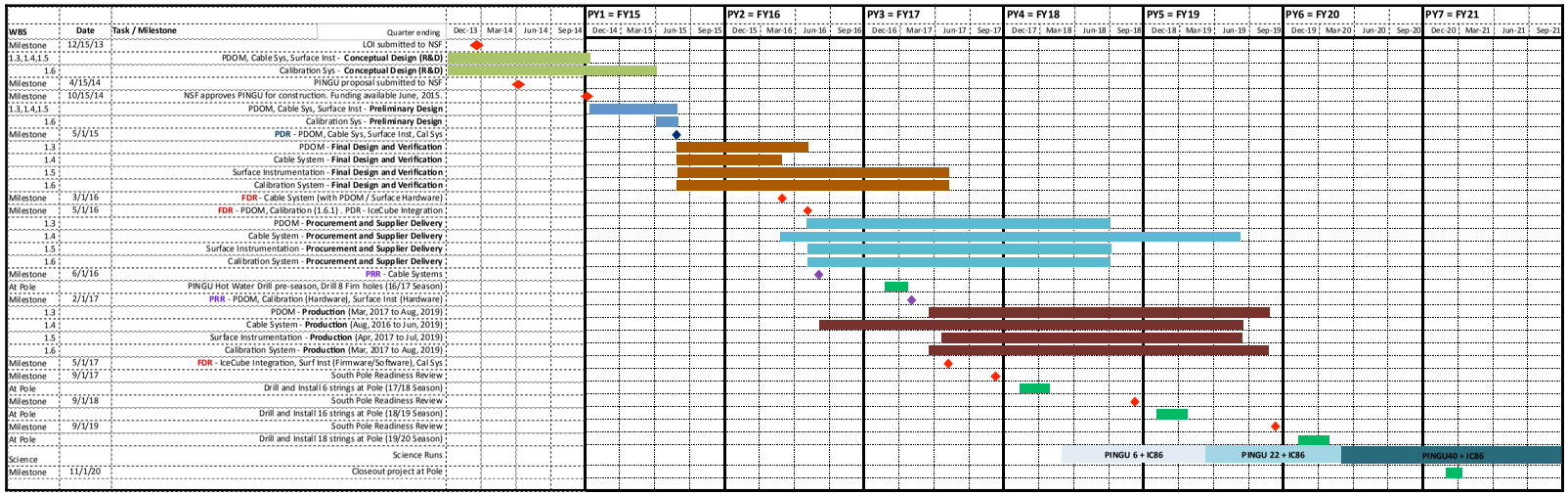


Figure 48: Schedule for PINGU R&D, preliminary and final design, procurement, Production and Drilling and Deployment phases. With an assumed funding start date of fall 2014, PINGU string deployments begin in the 2017/18 austral summer and finish in early 2020. Important review milestones are indicated by diamonds.

Figure 49: The new Amundsen-Scott South Pole Station in 2010.

Figure 50: LC-130 aircraft are used to transport cargo and personnel to the South Pole.

## Appendix A. Hierarchy Analysis Techniques

Three different statistical analyses were developed to assess the sensitivity of PINGU to the neutrino mass hierarchy. They fall on a continuum from highly detailed but computationally expensive simulations, to faster but more approximate models of the data to be obtained by PINGU. These analyses were developed independently, both to establish reliability via cross-validation and to enable comparisons to external studies reported in the literature, e.g. Refs. [41, 43, 26, 24].

Generally speaking, the more highly detailed analyses have been used to validate the approximations required by the faster analysis methods, which in turn are fast enough to incorporate a far broader range of systematic effects that might impact the sensitivity of PINGU. However, the more detailed analyses rely on finite libraries of Monte Carlo events; because the PINGU projections are based on a fully simulated analysis derived from the current DeepCore physics analyses, generation of the simulated PINGU events (in which individual Cherenkov photons are tracked throughout the IceCube volume) is rather time-consuming. The finite Monte Carlo statistics available for these studies produce an indirect but significant systematic bias in the results from the more detailed studies. The magnitude of this bias grows as the statistical fluctuations in the Monte Carlo sets increase, which led to over-optimistic initial projections from early Monte Carlo studies of PINGU based on limited statistics [46].

The Monte Carlo data sets presently available are approximately an order of magnitude larger than those used for the early studies, so that the bias due to statistical noise is now $0.2\sigma$. When the significance estimates from the full Monte Carlo studies are corrected downward to account for this bias, and the same sets of systematic effects are included in the various analysis methods, the estimates of PINGU's sensitivity to the neutrino mass hierarchy agree at the 5% level. Our estimate of the significance with which the hierarchy can be determined is therefore taken from the parametric analysis based on the Fisher information matrix, described in Appendix A.3, which incorporates the largest range of systematics and is free from any bias due to finite Monte Carlo statistics, but which relies on parametric descriptions of the detector performance. The more detailed analyses used to validate that analysis are described in Appendix A.1 and Appendix A.2.

*Appendix A.1. Likelihood ratio (LLR) analysis*

The most statistically detailed analysis uses a library of simulated events to predict the distribution of events in the $E_\nu$ vs. $\cos\theta_\nu$ space which would be expected from different possible combinations of true oscillation parameters. From these distributions, ensembles of pseudo-experiments are generated for each scenario, and a likelihood ratio method is used to determine, for each set of pseudo-data, the degree to which one hierarchy is favored by the pseudo-data. Although this approach is computationally too intensive to incorporate the full range of systematics under investigation, it provides a benchmark to ensure that the statistical approximations used in the other two methods are valid. At present we have only marginalized two systematic uncertainties as nuisance parameters in this analysis, the oscillation parameters $\Delta m^2_{\rm atm}$ and $\sin^2(\theta_{23})$.

The starting point for the analysis is the generation of two high-statistics "template" histograms of the $E_\nu$ vs. $\cos\theta_\mu$ space, analogous to the "Asimov" expectations described below. These histograms contain the expected observations for each bin, including both the physics modeled by GENIE, GEANT, and full Cherenkov photon propagation through a realistic ice model, and the effects of the detector resolution as predicted by the full reconstruction and event selection analysis pipeline. One histogram is produced for each hierarchy.

Ensembles of pseudo-data sets are then drawn from each template, with each bin in ($E_\nu$,$\cos\theta_\mu$) scaled to one year of livetime and repeatedly varied following Poisson statistics. These pseudo-data sets are compared binwise, using Poisson statistics, to each template to create log-likelihoods of observing the pseudo-data under a given hypothesis,

$$\ln\mathcal{L} = \sum_{i,j} n_{ij}\ln\mu_{ij} - \mu_{ij} - \ln n_{ij}!, \tag{A.1}$$

where $n_{ij}$ is the content of the $(i,j)$th bin in the pseudo-data and $\mu_{ij}$ is the expectation for that bin from a given (i.e., either inverted or normal hierarchy) template.

For each data set, two likelihoods are calculated, labeled $\mathcal{L}$( pseudo-data | template ):

$$\mathcal{L}(\mathrm{IH}|\mathrm{IH}) \quad \text{and} \quad \mathcal{L}(\mathrm{IH}|\mathrm{NH}), \quad \text{or} \quad \mathcal{L}(\mathrm{NH}|\mathrm{IH}) \quad \text{and} \quad \mathcal{L}(\mathrm{NH}|\mathrm{NH}), \tag{A.2}$$

depending on whether the pseudo-data set was generated assuming the inverted or the normal hierarchy was correct. These likelihoods are used to create the log likelihood ratios (LLR):

$$\frac{\mathcal{L}(\mathrm{IH}|\mathrm{IH})}{\mathcal{L}(\mathrm{IH}|\mathrm{NH})} \quad \text{or} \quad \frac{\mathcal{L}(\mathrm{NH}|\mathrm{IH})}{\mathcal{L}(\mathrm{NH}|\mathrm{NH})}, \tag{A.3}$$

respectively. We created and processed $10^5$ pseudo-data sets in this manner for each set of assumed true oscillation parameters, to ensure adequate coverage of the probability space.

To estimate the confidence with which a given hierarchy can be rejected, the likelihood ratio obtained for the pseudo-data set is compared to the distribution of LLRs expected if the opposite hierarchy were correct. (In principle, one could evaluate a Bayesian odds ratio or follow a quasi-Bayesian approach where the "null hypothesis" distribution were taken from a weighted average of possible oscillation parameters in the opposite-hierarchy space, but we find that the distributions of the LLRs are relatively stable with respect to the assumed oscillation parameters, so that the world-average oscillation parameters are used for the "null" distribution.) Our ensemble of pseudo-experiments produces a distribution of expected significances; to estimate PINGU's ability to distinguish the hierarchies we calculate the fraction of cases in which e.g. a NH data set will have a likelihood ratio more consistent with the IH template than the median of an ensemble of IH data sets, as shown in Fig. A.51. A similar calculation is made under the alternate assumption that the NH is the true hierarchy.

To investigate the impact of systematic uncertainties such as the experimental uncertainty on the measured value of $\Delta m^2_{\text{atm}}$, the procedure outlined above is modified as follows. Instead of one template for each hierarchy, a full set of templates is generated for each hierarchy, using a range of possible values of $\Delta m^2_{\text{atm}}$. We fit for $\Delta m^2_{\text{atm}}$ in each pseudo-experiment, by comparing each pseudo-data set to templates for each hierarchy generated over a range of $\Delta m^2_{\text{atm}}$ values corresponding to $\pm 2\sigma$ from the current world average. For each pseudo-data set, a LLR is calculated based on the templates yielding the best likelihood in the IH region of the oscillation parameter space and the best likelihood in the NH region of parameter space. This procedure mimics what we anticipate applying in the analysis of experimental data. In general, the $\Delta m^2_{\text{atm}}$ with the highest likelihood for a given pseudo-data set is not precisely the same as the $\Delta m^2_{\text{atm}}$ of the template from which it was drawn, in contrast to the situation when using the Asimov approximation.

The LLR analysis treats $\Delta m^2_{\text{atm}}$ and $\sin^2(\theta_{23})$ as nuisance parameters in the fit, and other systematics (both physics parameters and detector-related uncertainties) can be incorporated in the same manner. Although no other systematics were considered in the present analysis due to the rapidly increasing computation time needed to incorporate additional nuisance parameters, fully detailed event simulation, selection and reconstruction were used, the effects of Poisson fluctuations in the experimental observables were explicitly modeled, and no assumptions regarding the underlying distribution of the test statistics

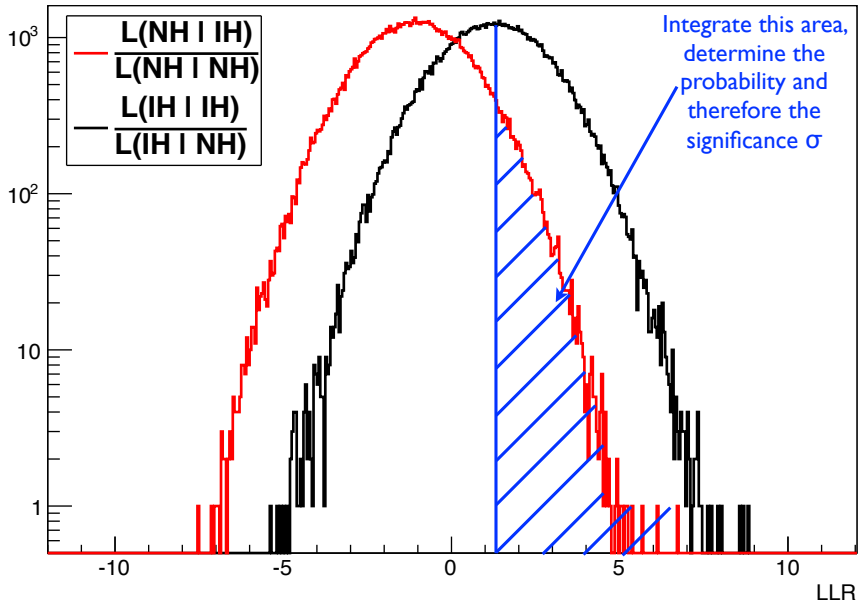


Figure A.51: Calculation of the expected significance for one set of pseudo-experiments using the log-likelihood ratio (LLR) method. Each curve shows the distribution of the ratio of the likelihood of observing the data under the IH hypothesis to that of observing the data under the NH hypothesis; i.e., the extent to which the data favor the IH. Higher values indicate that the data are more consistent with the inverted hierarchy, and lower values mean the data are more consistent with the normal hierarchy. The red curve is generated assuming the NH is true, and the black assuming the IH. The expected significance after one year of observation is given by the fraction of one distribution which lies beyond the median of the other, as shown.

were required. This analysis was therefore compared to the Asimov analysis technique, described below, to verify that the statistical assumptions made in that analysis are valid. We anticipate that the analysis of real data from PINGU would be undertaken using a full likelihood analysis similar to that described here.

*Appendix A.2. Asimov analysis*

Our second analysis likewise uses the library of simulated events, and therefore incorporates all correlations between the impact of systematics and reconstruction resolutions on

individual events, but uses the so-called "Asimov" approximation[7] instead of generating ensembles of pseudo-experiments for every possible combination of oscillation parameters [44]. Essentially, this technique assumes that statistical fluctuations in the experimental data are as likely to reinforce as to obscure the signature of the correct hierarchy, so that only the single data set most likely to be observed for given any set of oscillation parameters must be analyzed.

In this approximation, an estimate $\Delta\chi^2$ of the confidence levels with which a given set of oscillation parameters could be excluded can be defined as

$$\Delta\chi^2 = \sum_i \frac{(n_i^{true} - n_i^{alt})^2}{\sigma_{n_i}^2}, \tag{A.4}$$

where $n_i^{true}$ corresponds to the event expectation in bin $i$ for a given set of oscillation and nuisance parameters under study, $n_i^{alt}$ the expectation for any alternate set of oscillation and nuisance parameters, and $\sigma_{n_i}$ is chosen to be $\sqrt{n_i^{true}}$. A statistic of interest for this study is $\Delta\chi^2_h$, which we define to be the $\Delta\chi^2$ between the best-fitting set of oscillation and nuisance parameters in the normal hierarchy range of parameter space and the best fit in the inverted hierarchy space: $\Delta\chi^2_h = \Delta\chi^2_{\text{min,NH}} - \Delta\chi^2_{\text{min,IH}}$. Positive values of this parameter indicate that the inverted hierarchy is favored, while negative values prefer the normal hierarchy.

The analysis of a single representative data set should predict the median significance accurately as long as the effect being observed is small, $|n_i^{true} - n_i^{alt}| \ll n_i^{true}$, since for this case statistical fluctuations in the number of observed events in any real data set are approximately as likely to increase the significance of a measurement as to decrease it [114]. For the case at hand, the representative data set is sufficient for the purpose of calculating the median significance without the need to generate large ensembles of pseudo-experiments. This greatly increases the speed of the calculation. When quoting significances, we assume that the test statistic, $\Delta\chi^2_h$, follows a $\chi^2$ distribution with the appropriate number of degrees of freedom; the validity of this assumption is demonstrated below.

The representative data set is constructed from a full three-flavor simulation of atmospheric neutrinos, to which the reconstruction methods and selection criteria described in Sec. 4.1.1 are applied. The full details of the reconstruction including the shapes of the

[7]This is a reference to the Isaac Asimov short story *Franchise*, in which the single most typical voter replaces the full electorate.

tails and correlations between parameters are thus taken into account. All neutrino flavors are considered, not only $\nu_\mu$ CC (*i.e.*, "track") events, and in fact the cascade channel makes a substantial contribution to the overall significance.

An example of the expectation for $\nu_\mu$ CC events is shown in Fig. A.52. The overall expectation is calculated by summing the simulated events produced by all neutrino flavors, divided into a set which is reconstructed as "track-like" (primarily $\nu_\mu$ CC) and one reconstruced as "cascade-like" using the methods described in Sec. 2.6. The bin size is chosen such that it roughly matches the experimental resolution. The corresponding expectations for data sets assuming a variety of alternate values of the oscillation parameters can be calculated quickly by re-calculating the weights applied to each event in the Monte Carlo sample.

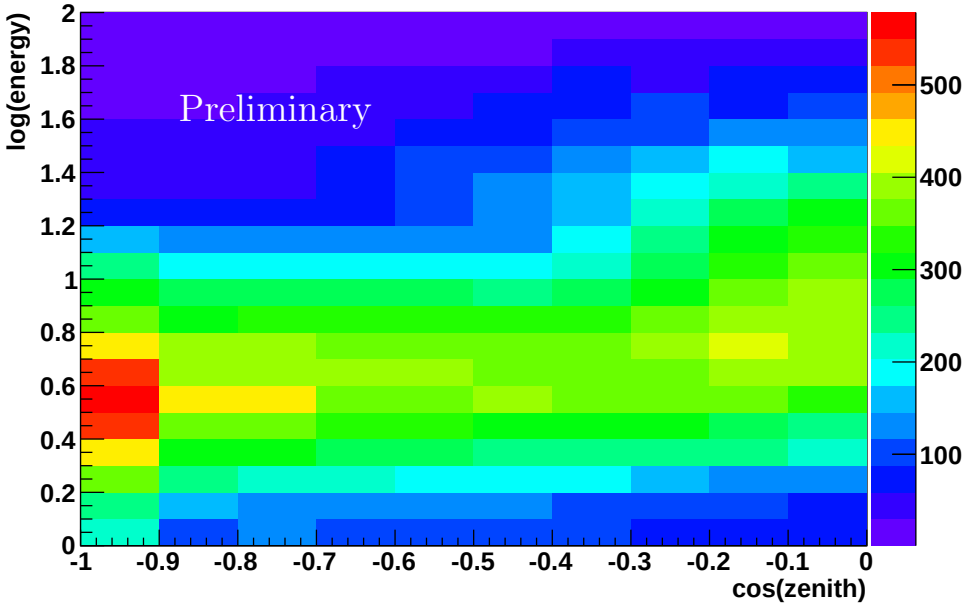


Figure A.52: Expected rate of $\nu_\mu$ CC events per year as a function of reconstructed $\log_{10} \mathrm{E}_\nu$ and $\cos\theta_\nu$. The oscillation parameters were set to $\Delta m^2_{\mathrm{atm}} = +2.42 \cdot 10^{-3}$ eV$^2$ (NH), $\sin^2(\theta_{13}) = 0.024$ and $\sin^2(\theta_{23}) = 0.39$. The full expected event rate includes neutrinos of all flavors, and both NC and CC events.

The representative event distribution for the true oscillation parameters, as a function of reconstructed $\cos\theta_\nu$ and $\log_{10} \mathrm{E}_\nu$, is then compared to expectations for the alternative hierarchy with a variety of different mixing angle and mass splitting parameters, and $\Delta\chi^2$

for each set of parameters is calculated according to Eq. A.4. Since statistical fluctuations are not modeled in the Asimov approach, $\chi^2 = 0$ by construction at the injected values of the oscillation parameters. The data set used to determine the neutrino mass hierarchy for one year of livetime has its minimum $\Delta\chi^2_h$ at a value of $-2.8$ (see Fig. A.53) for $\nu_\mu$ CC assuming ideal particle identification; the negative sign indicates that these pseudo-data prefer the normal hierarchy. (In this example, a maximal mixing angle $\sin^2(\theta_{23}) = 0.5$ would also be excluded at high significance.)

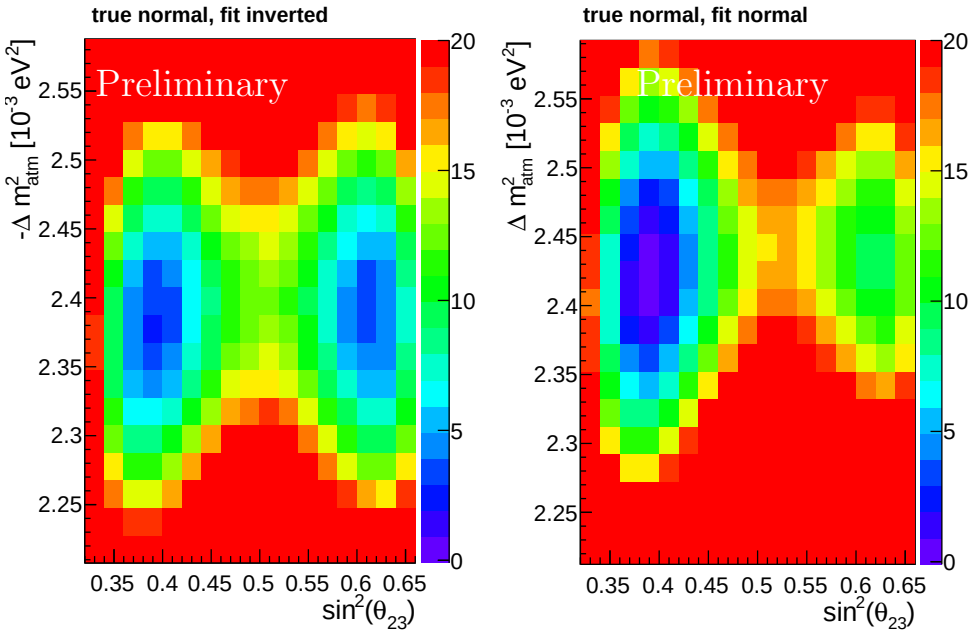


Figure A.53: Median values of $\chi^2$ expected when fitting oscillation parameters in the range around $\pm|\Delta m^2|$, corresponding the IH (left) and NH (right) scenarios. The $\chi^2$ for the injected parameters is zero by construction in the Asimov approximation, so that $\Delta\chi^2$ can be read directly from the color scale. The $1\sigma$, $2\sigma$, and $3\sigma$ contours correspond to $\Delta\chi^2$ of 1, 4, and 9 respectively. The normal hierarchy is assumed to be true in this example. The significance of the NMH determination, $\Delta\chi^2_h$, is given by the lowest $\Delta\chi^2$ seen in the IH range of $\Delta m^2$ shown in the left-hand plot, which in this example has a magnitude of 2.8 corresponding to an estimated significance of $1.7\sigma$.

When converting $\Delta\chi^2_h$ to a significance, we rely on Wilks' theorem. This theorem states that the $\Delta\chi^2$ between a null and alternative hypothesis will follow a $\chi^2$ distribution with number of degrees of freedom equal to the number of free parameters in the hypothesis. In this case, there is one free parameter (the hierarchy), so that $\sqrt{\Delta\chi^2_h}$ should approximately equal the significance in standard deviations. Concerns have been raised

in the literature (for example [114] and [115]) regarding the validity of this approach for estimating significances when determining the mass hierarchy, since the hierarchy is a binary parameter rather than a continuous one, and the hypothesis which plays the role of the null (the alternate hierarchy) is not nested in the hypothesis space as required by Wilks' theorem. To validate this estimate, we therefore implemented a study with large numbers of pseudo-experiments (but a reduced set of systematics) and compared the observed distribution of $\Delta\chi^2_h$ to the expected $\chi^2$ distribution with one degree of freedom. The cumulative distribution functions of $\Delta\chi^2_h$ under the opposite hypothesis are shown in Fig. A.54 compared to the $\chi^2$ distribution with one degree of freedom. These cumulative distribution functions are essentially the $p$-values of the test, since they provide the probability of observing a given value of $\Delta\chi^2_h$ or higher by chance and erroneously rejecting the correct hypothesis. The various lines correspond to ensembles of pseudo-experiments assuming different true values of the oscillation parameters (under the normal hierarchy). For most assumed true values of these parameters, the p-value estimated from $\sqrt{\Delta\chi^2_h}$ *exceeds* the p-value obtained from the simulated distribution of the test statistic in the pseudo-experiments (indicating that the estimated significance is in fact conservative), and in no case is the significance substantially overestimated. [8]

The systematic uncertainties detailed in Sec. 4.1.3 are incorporated into this method as nuisance parameters in the $\chi^2$ sum, in exactly the same manner as the physical oscillation parameters $\Delta m^2_{\text{atm}}$ and $\sin^2(\theta_{23})$. They are simultaneously fit to the data with penalty terms (priors) according to the current estimated uncertainties. Comparisons of the estimated median $\Delta\chi^2_h$ with and without these systematics included are shown in Fig. A.55. The final sensitivity, including systematic errors, is presented in Sec. 4.1.3.

When estimating the significance obtained from a full MC simulation, one must take into account that the underlying template (Asimov) distributions are produced with finite MC event statistics [116]. The signal arises from a difference in oscillation probabilities and the expectations under both the NH and IH scenarios are calculated from the same set of Monte Carlo events, with different weights applied to each event depending on the oscillation parameters at hand. Thus, fluctuations will enter both the NH and IH templates in a correlated manner and the error due to these fluctuations largely cancels.

[8] We note that, in contrast to the method studied by [114], we are fitting for the mass splitting parameter, $\Delta m^2$, which is indeed a continuous parameter as required by Wilks' Theorem. We have confirmed that if we were to assume a *fixed* value of $\Delta m^2$ based on external measurements, rather than fitting for it, we would be unable to determine the hierarchy correctly over much of the allowed parameter space, as suggested by [114].

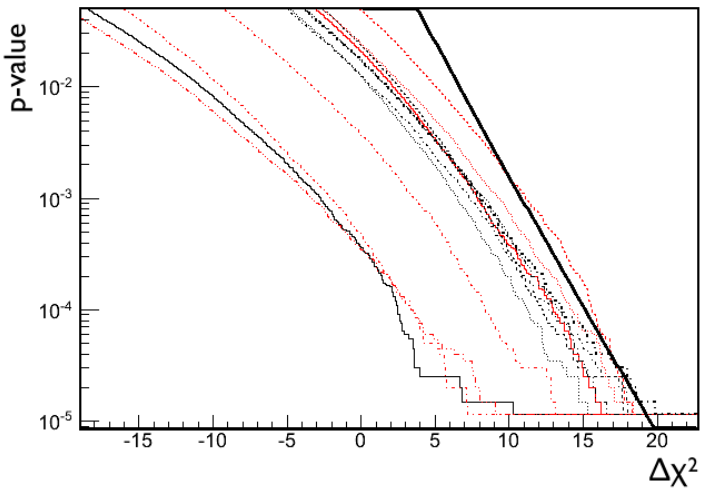


Figure A.54: Comparison of the significance estimated by assuming the $\Delta\chi^2_h$ statistic follows a $\chi^2$ distribution with 1 d.o.f. (heavy black line) with the actual significance of a given value of $\Delta\chi^2_h$ as determined by simulating ensembles of pseudo-experiments with different values of the various oscillation parameters. Unlike the $\Delta\chi^2$ obtained when comparing a hypothesis to a null nested into the hypothesis space, $\Delta\chi^2_h$ can be either positive or negative with the sign indicating the preferred hierarchy (in this case, the normal hierarchy). Where the heavy black line is above the cumulatives of the pseudo-experiments (dashed and dotted lines), the true significance is underestimated by the method used here; where it is below, the true significance is overestimated.

However, the smearing due to reconstruction has to be properly sampled as well and we have found that, despite the equivalent of more than 5 years of experimental livetime, the templates are susceptible to fluctuations. The migration of events between observable bins due to the reconstruction is correlated for the two hierarchies, and this leads to a systematically positively biased estimate of the significance with which the hierarchy can be determined in the Asimov and LLR analyses. The size of this bias is estimated by resampling the events around their true energy and zenith angle using parameterized resolution functions identical to those used in the Fisher matrix analysis discussed below. For cascade-like events, where the signature in the $(\mathrm{E}_\nu, \cos\theta_\nu)$-plane only has large-scale features (cf. Fig. 12) and resolution-related effects are of minor importance, this reduces the signifcance by $0.15\sigma$ with the currently available Monte Carlo statistics. For track-like events in contrast a stronger correction of $0.74\sigma$ is needed for the chosen bin size. While selecting larger bins in $(\mathrm{E}_\nu, \cos\theta_\nu)$ can mitigate this systematic effect, it would diminish the power of a good detector resolution and unduly reduce the significance.

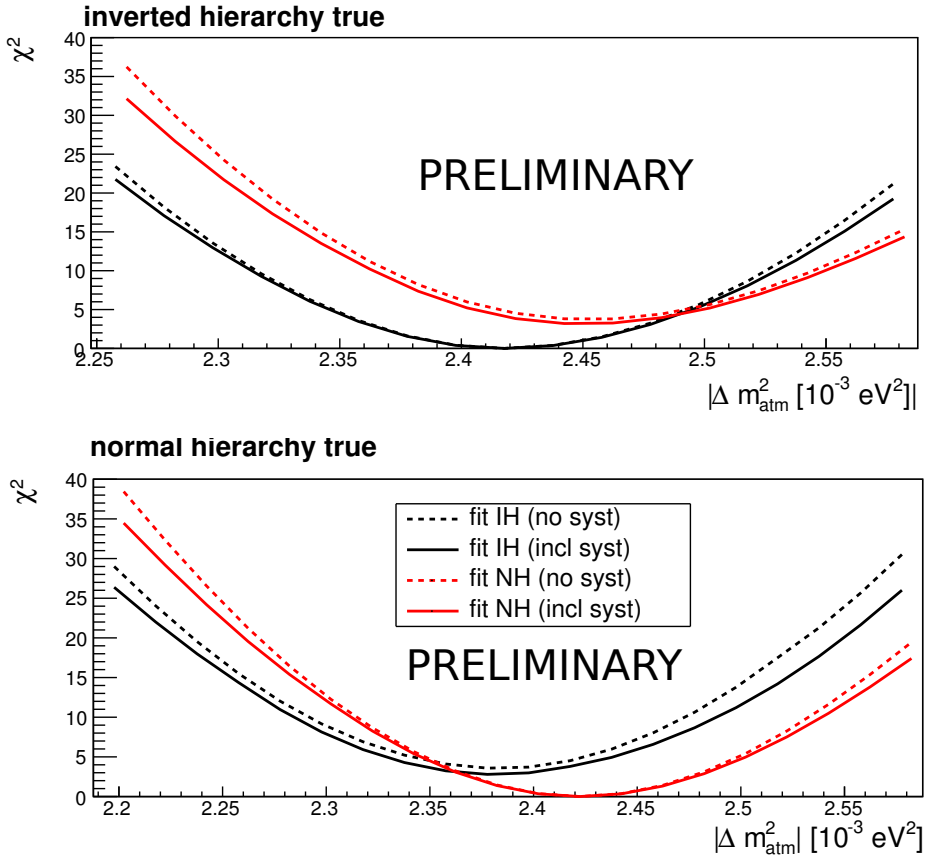


Figure A.55: The effect of the systematic uncertainties is visualized in this plot: $\Delta\chi^2$ as a function of $|\Delta m^2_{\text{atm}}|$ in both the IH (top) and NH (bottom) after marginalization over $\sin^2(2\theta_{23})$, with and without the inclusion of systematic uncertainties. In each plot, the red line shows the best-fit $\Delta\chi^2$ around the NH solution ($\Delta m^2 > 0$) and the black shows the region around the IH solution. The significance of the NMH determination, $\Delta\chi^2_h$, is the vertical difference between the two minima in each plot. Both physical nuisance parameters like $\sin^2(2\theta_{23})$ and detector-related systematics such as energy scale are accounted for by being fit simultaneously.

*Appendix A.3. Fisher matrix analysis*

To complement the Monte Carlo-based Asimov method described above, we employ a closely related method, the Fisher information matrix [45], that is tailored to evaluate the covariance of the parameter of interest in the presence of a large number of systematic errors. In a nutshell, one is evaluating the shape of the likelihood function at the (true)

minimum to obtain an estimate of the covariance matrix of the parameters. Since this can be done without probing the parameter space in all dimensions simultaneously, a large number of parameters (neutrino masses and mixing angles as well as parameters characterizing the systematic errors) can be incorporated quickly. This study uses parametric models for the effective volume, as well as the energy and neutrino angle resolution (which also take into account the effect of missing energy in $\nu_\tau$ and NC events). Being parametric, it is unaffected by the systematic bias due to statistical fluctuations described above.

At the heart of the method lies the Fisher information matrix, consisting of the partial derivatives of the event counts in each bin with respect to all parameters under study (calculated numerically) for the true parameters, weighted by the statistical errors:

$$F_{kl} = \sum_i \frac{1}{\sigma_{n_i}^2} \frac{\partial n_i}{\partial p_k} \frac{\partial n_i}{\partial p_l}, \tag{A.5}$$

where $p_k$, $p_l$ denote the parameters with index $k$ and $l$, while $n_i$ is the expected number of events in bin $i$ and $\sigma_{n_i} = \sqrt{n_i}$ the corresponding uncertainty. Inverting the Fisher matrix yields the full covariance matrix between the parameters, while the purely statistical uncertainty of parameter $i$ is given by $1/\sqrt{F_{ii}}$.

Since all parameters must be continuous to be incorporated, the mass hierarchy is represented by a parameter $h$, superimposing the observed event counts in each bin according to

$$n_i^{obs} = h n_i^{true} + (1-h) n_i^{alt}.$$

Inserting this parameterization with the partial derivative $\partial n_i^{obs}/\partial h = n_i^{true} - n_i^{alt}$ into Eq. A.5, one readily obtains the Asimov $\Delta\chi^2$ of Eq. A.4 where the significance of the NMH measurement is given by $1/\sigma_h$. Hence, in the limit of a single parameter $h$, one reproduces the Asimov method. The derivatives for the other parameters are obtained numerically and, in the range of interest, the linear approximation of the parameter dependence is sufficiently accurate (as previously shown in [115]). Only $\delta_{\mathrm{CP}}$ can not be incorporated reliably in this approach, due to the lack of external constraints on its value, but PINGU is expected to have low sensitivity to this parameter [43], which we have verified using the LLR analysis. Since the dependence of the hierarchy measurement on $\delta_{\mathrm{CP}}$ is small, we fix $\delta_{\mathrm{CP}} = 0$. Strong covariance of another parameter with the hierarchy parameter would indicate that there is a potentially important systematic which might affect our ability to measure the hierarchy.

We have found that when examining the same sets of external nuisance parameters, the results from the Fisher information matrix agrees well with the Asimov Monte Carlo simulation approach when accounting for the bias from limited Monte Carlo statistics. We are therefore confident that the parametric approximations used in this analysis are reliable, and use it to incorporate a wider variety of systematics and determine the sensitivity of PINGU to the hierarchy for longer exposures than can be estimated using the Monte Carlo-based methods.

## References


[1] **IceCube** Collaboration, M. Aartsen *et. al.*, "Evidence for High-Energy Extraterrestrial Neutrinos at the IceCube Detector," *Science 342,* **1242856** (2013) arXiv:1311.5238.

[2] **IceCube** Collaboration, M. Aartsen *et. al.*, "Measurement of South Pole ice transparency with the IceCube LED calibration system," *Nucl. Instrum. Meth.* **A711** (2013) 73–89, arXiv:1301.5361.

[3] **IceCube** Collaboration, M. Aartsen *et. al.*, "Measurement of Atmospheric Neutrino Oscillations with IceCube," *Phys. Rev. Lett.* **111** (2013) 081801, arXiv:1305.3909.

[4] S. Euler, L. Gladstone, C. Wiebusch, *et. al.*, "Measurement of atmospheric neutrino oscillations with IceCube/DeepCore in its 79-string configuration," *Proceedings of the 33rd International Cosmic Ray Conference* **-ICRC** (2013) , Rio de Janeiro, Brazil., arXiv:1304.0735.

[5] **IceCube** Collaboration, M. Aartsen *et. al.*, "Search for dark matter annihilations in the Sun with the 79-string IceCube detector," *Phys. Rev. Lett.* **110** (2013) 131302, arXiv:1212.4097.

[6] L. Wolfenstein, "Neutrino oscillations in matter," *Phys. Rev.* **D17** (1978) 2369–2374.

[7] S. Mikheyev and A. Y. Smirnov, "Resonant neutrino oscillations in matter," *Prog. Part. Nucl. Phys.* **23** (1989) 41–136.

[8] E. K. Akhmedov, A. Dighe, P. Lipari, and A. Y. Smirnov, "Atmospheric neutrinos at super-kamiokande and parametric resonance in neutrino oscillations," *Nucl. Phys.* **B542** (1999) 3–30, arXiv:hep-ph/9808270.

[9] R. Mohapatra, S. Antusch, K. Babu, G. Barenboim, M.-C. Chen, *et. al.*, "Theory of neutrinos: A White paper," *Rept. Prog. Phys.* **70** (2007) 1757–1867, arXiv:hep-ph/0510213.

[10] **T2K** Collaboration, K. Abe *et. al.*, "The T2K Experiment," *Nucl. Instrum. Meth.* **A659** (2011) 106–135, arXiv:1106.1238.

[11] **NOvA** Collaboration, M. Messier, "Extending the NOvA Physics Program," arXiv:1308.0106.

[12] **LBNE** Collaboration, T. Akiri *et. al.*, "The 2010 Interim Report of the Long-Baseline Neutrino Experiment Collaboration Physics Working Groups," arXiv:1110.6249.

[13] J. Hewett, H. Weerts, R. Brock, J. Butler, B. Casey, *et. al.*, "Fundamental Physics at the Intensity Frontier," arXiv:1205.2671.

[14] F. Feruglio, A. Strumia, and F. Vissani, "Neutrino oscillations and signals in beta and 0nu2beta experiments," *Nucl. Phys.* **B637** (2002) 345–377, arXiv:hep-ph/0201291.

[15] C. S. Fong, E. Nardi, and A. Riotto, "Leptogenesis in the Universe," *Adv. High Energy Phys.* **2012** (2012) 158303, arXiv:1301.3062.

[16] **NOvA** Collaboration, D. Ayres *et. al.*, "The NOvA Technical Design Report,".

[17] **Intensity Frontier Neutrino Working Group** Collaboration, A. de Gouvea *et. al.*, "Neutrinos," arXiv:1310.4340.

[18] **T2K** Collaboration, K. Abe *et. al.*, "Evidence of Electron Neutrino Appearance in a Muon Neutrino Beam," *Phys. Rev.* **D88** (2013) 032002, arXiv:1304.0841.

[19] P. Adamson, J. Coelho, G. Davies, J. Evans, P. Guzowski, *et. al.*, "CHerenkov detectors In mine PitS (CHIPS) Letter of Intent to FNAL," arXiv:1307.5918.

[20] **LBNE** Collaboration, C. Adams *et. al.*, "Scientific Opportunities with the Long-Baseline Neutrino Experiment," arXiv:1307.7335.

[21] Y.-F. Li, J. Cao, Y. Wang, and L. Zhan, "Unambiguous Determination of the Neutrino Mass Hierarchy Using Reactor Neutrinos," *Phys. Rev.* **D88** (2013) 013008, arXiv:1303.6733.

[22] **RENO-50** Collaboration http://home.kias.re.kr/MKG/h/reno50/.

[23] T. Thakore, A. Ghosh, S. Choubey, and A. Dighe, "The Reach of INO for Atmospheric Neutrino Oscillation Parameters," *J. High Energy Phys.* **1305** (2013) 058, arXiv:1303.2534.

[24] M. Blennow, P. Coloma, P. Huber, and T. Schwetz, "Quantifying the sensitivity of oscillation experiments to the neutrino mass ordering," arXiv:1311.1822.

[25] K. Abe, T. Abe, H. Aihara, Y. Fukuda, Y. Hayato, *et. al.*, "Letter of Intent: The Hyper-Kamiokande Experiment — Detector Design and Physics Potential —," arXiv:1109.3262.

[26] W. Winter, "Neutrino mass hierarchy determination with IceCube-PINGU," *Phys. Rev.* **D88** (2013) 013013, arXiv:1305.5539.

[27] **IceCube** Collaboration, A. Achterberg *et. al.*, "First Year Performance of The IceCube Neutrino Telescope," *Astropart. Phys.* **26** (2006) 155–173, arXiv:astro-ph/0604450.

[28] **IceCube** Collaboration, R. Abbasi *et. al.*, "The Design and Performance of IceCube DeepCore," *Astropart. Phys.* **35** (2012) 615–624, arXiv:1109.6096.

[29] U. of Wisconsin-Madison Physical Sciences Lab, "Enhanced Hot Water Drill." http://www.psl.wisc.edu/projects/large/icecube/more-icecube/ewhd.

[30] C. Andreopoulos, A. Bell, D. Bhattacharya, F. Cavanna, J. Dobson, *et. al.*, "The GENIE Neutrino Monte Carlo Generator," *Nucl. Instrum. Meth.* **A614** (2010) 87–104, arXiv:0905.2517.

[31] **GEANT4** Collaboration, S. Agostinelli *et. al.*, "GEANT4: A Simulation toolkit," *Nucl. Instrum. Meth.* **A506** (2003) 250–303.

[32] **IceCube** Collaboration, D. Chirkin, "Photon tracking with GPUs in IceCube," *Nucl. Instrum. Meth.* **A725** (2013) 141–143.

[33] M. Ribordy and A. Y. Smirnov, "Improving the neutrino mass hierarchy identification with inelasticity measurement in PINGU and ORCA," *Phys. Rev.* **D87** (2013) 113007, arXiv:1303.0758.

[34] F. Feroz, M. P. Hobson, and M. Bridges, "Multinest: an efficient and robust bayesian inference tool for cosmology and particle physics," *Mon. Not. Roy. Astron. Soc.* **398** (Oct., 2009) 1601–1614, arXiv:0809.3437.

[35] M. Honda, T. Kajita, K. Kasahara, S. Midorikawa, and T. Sanuki, "Calculation of atmospheric neutrino flux using the interaction model calibrated with atmospheric muon data," *Phys. Rev.* **D75** (2007) 043006, arXiv:astro-ph/0611418.

[36] **IceCube** Collaboration, M. Aartsen *et. al.*, "Measurement of the Atmospheric $\nu_e$ flux in IceCube," *Phys. Rev. Lett.* **110** (2013) 151105, arXiv:1212.4760.

[37] A. Hoecker, P. Speckmayer, J. Stelzer, J. Therhaag, E. von Toerne, and H. Voss, "TMVA: Toolkit for Multivariate Data Analysis," *PoS* **ACAT** (2007) 040, arXiv:physics/0703039.

[38] **Particle Data Group** Collaboration, J. Beringer *et. al.*, "Review of particle physics," *Phys. Rev.* **D86** (Jul, 2012) 010001.

[39] G. Fogli, E. Lisi, A. Marrone, and A. Palazzo, "Global analysis of three-flavor neutrino masses and mixings," *Prog. Part. Nucl. Phys.* **57** (2006) 742–795.

[40] A. Dziewonski and D. Anderson, "Preliminary reference earth model," *Phys. Earth Planet. In.* **25** (1981) 297–356.

[41] O. Mena, I. Mocioiu, and S. Razzaque, "Neutrino mass hierarchy extraction using atmospheric neutrinos in ice," *Phys. Rev.* **D78** (2008) 093003.

[42] G. L. Fogli, E. Lisi, A. Marrone, D. Montanino, A. Palazzo, and A. M. Rotunno, "Global analysis of neutrino masses, mixings, and phases: Entering the era of leptonic cp violation searchers," *Phys. Rev.* **D86** (Jul, 2012) 013012.

[43] E. K. Akhmedov, S. Razzaque, and A. Y. Smirnov, "Mass hierarchy, 2-3 mixing and CP-phase with Huge Atmospheric Neutrino Detectors," *J. High Energy Phys.* **1302** (2013) 082, arXiv:1205.7071.

[44] G. Cowan, K. Cranmer, E. Gross, and O. Vitells, "Asymptotic formulae for likelihood-based tests of new physics," *Eur. Phys. J.* **C71** (2010) 1554.

[45] R. A. Fisher, "On the mathematical foundations of theoretical statistics," *Phil. Trans. Royal Soc. A* **220** (1922) 309–368.

[46] **IceCube/PINGU** Collaboration, M. Aartsen *et. al.*, "PINGU Sensitivity to the Neutrino Mass Hierarchy," arXiv:1306.5846.

[47] **MINERvA** Collaboration, L. Aliaga *et. al.*, "Design, Calibration, and Performance of the MINERvA Detector," arXiv:1305.5199.

[48] A. Gazizov, C. Spiering, M. Kowalski, K. Kuzmin, and V. Naumov *in preparation.*

[49] **AMANDA** Collaboration, J. Ahrens *et. al.*, "Muon track reconstruction and data selection techniques in AMANDA," *Nucl. Instrum. Meth.* **A524** (2004) 169–194, arXiv:astro-ph/0407044.

[50] **MINOS** Collaboration, P. Adamson *et. al.*, "Measurement of Neutrino and Antineutrino Oscillations Using Beam and Atmospheric Data in MINOS," *Phys. Rev. Lett.* **110** (2013) 251801, arXiv:1304.6335.

[51] **T2K** Collaboration, K. Abe *et. al.*, "Measurement of Neutrino Oscillation Parameters from Muon Neutrino Disappearance with an Off-axis Beam," arXiv:1308.0465.

[52] J. Leute, A. Groß, E. Resconi, *et. al.*, "Study of the sensitivity of IceCube/DeepCore to atmospheric neutrino oscillations," *Proceedings of the 33rd International Cosmic Ray Conference* **-ICRC** (2013) , Rio de Janeiro, Brazil., arXiv:1304.0735.

[53] M. Gonzalez-Garcia, M. Maltoni, J. Salvado, and T. Schwetz, "Global fit to three neutrino mixing: critical look at present precision," arXiv:1209.3023.

[54] D. Cherdack, M. Bass, and B. Wilson, "T2K future sensitivity predictions," http://tinyurl.com/o6t7wa8.

[55] W. Gilbert, *De magnete*. 1600.

[56] B. A. Buffett, "Earth's core and the geodynamo," *Science* **288** (2000), no. 5473 2007–2012, http://www.sciencemag.org/content/288/5473/2007.full.pdf.

[57] Y. A. Popov, S. L. Pevzner, V. P. Pimenov, and R. A. Romushkevich, "New geothermal data from the Kola superdeep well SG-3," *Tectonophysics* **306** (1999), no. 34 345 – 366.

[58] A. W. Hofmann, "Mantle geochemistry: the message from oceanic volcanism," *Nature* **385** (Jan., 1997) 219–229.

[59] W. F. McDonough, "Compositional Model for the Earth's Core," *Treatise on Geochemistry* **2** (Dec., 2003) 547–568.

[60] R. D. Oldham, "The constitution of the interior of the earth, as revealed by earthquakes," *Q. J. Geol. Soc.* **62** (1906), no. 1-4 456–475, http://jgslegacy.lyellcollection.org/content/62/1-4/456.full.pdf+html.

[61] J. S. Resovsky and J. Trampert, "Reliable mantle density error bars: an application of the neighbourhood algorithm to normal-mode and surface wave data," *Geophys. J. Int.* **150** (Sept., 2002) 665–672.

[62] D. E. Smylie, "The Inner Core Translational Triplet and the Density Near Earth's Center," *Science* **255** (Mar., 1992) 1678–82.

[63] W. McDonough and S. Sun, "The composition of the Earth," *Chem. Geol.* **120** (Mar., 1995) 223–253.

[64] F. Birch, "Elasticity and constitution of the Earth's interior," *J. Geophys. Res.* **57** (June, 1952) 227–286.

[65] D. R. Fearn and D. E. Loper, "Compositional convection and stratification of Earth's core," *Nature* **289** (Jan., 1981) 393–394.

[66] C. J. Allègre, J.-P. Poirier, E. Humler, and A. W. Hofmann, "The chemical composition of the Earth," *Earth Planet. Sc. Lett.* **134** (Sept., 1995) 515–526.

[67] J. Li and Y. Fei, "Experimental Constraints on Core Composition," in *Treatise on geochemistry, Vol. 2: The Mantle and core* (R. W. Carlson, ed.), vol. 2, ch. 2.14, pp. 1–31. Elsevier, Amsterdam, 2007.

[68] O. Narygina, L. S. Dubrovinsky, C. a. McCammon, A. Kurnosov, I. Y. Kantor, V. B. Prakapenka, and N. a. Dubrovinskaia, "X-ray diffraction and Mössbauer spectroscopy study of fcc iron hydride FeH at high pressures and implications for the composition of the Earth's core," *Earth Planet. Sc. Lett.* **307** (July, 2011) 409–414.

[69] J. A. Formaggio and G. P. Zeller, "From ev to eev: Neutrino cross sections across energy scales," *Rev. Mod. Phys.* **84** (Sep, 2012) 1307–1341.

[70] F. Zwicky, "Die Rotverschiebung von extragalaktischen Nebeln," *Helv. Phys. Acta* **6** (1933) 110–127.

[71] **WMAP** Collaboration, E. Komatsu *et. al.*, "Seven-Year Wilkinson Microwave Anisotropy Probe (WMAP) Observations: Cosmological Interpretation," *Astrophys. J. Suppl.* **192** (2011) 18, `arXiv:1001.4538`.

[72] G. Bertone, D. Hooper, and J. Silk, "Particle dark matter: Evidence, candidates and constraints," *Phys. Rep.* **405** (2005) 279–390, `arXiv:hep-ph/0404175`.

[73] G. Bertone, ed., *"Non-WIMP Candidates"*. Particle Dark Matter: Observations, Models and Searches. 2010.

[74] I. F. M. Albuquerque, L. Hui, and E. W. Kolb, "High energy neutrinos from superheavy dark matter annihilation," *Phys. Rev. D* **64** (2001) 083504.

[75] **IceCube** Collaboration, R. Abbasi *et. al.*, "Search for Dark Matter from the Galactic Halo with the IceCube Neutrino Observatory," *Phys. Rev.* **D84** (2011) 022004, arXiv:1101.3349.

[76] **IceCube** Collaboration, R. Abbasi *et. al.*, "Search for Neutrinos from Annihilating Dark Matter in the Direction of the Galactic Center with the 40-String IceCube Neutrino Observatory," arXiv:1210.3557.

[77] **IceCube** Collaboration, M. Aartsen *et. al.*, "An IceCube Search for Dark Matter Annihilation in nearby Galaxies and Galaxy Clusters," arXiv:1307.3473.

[78] **IceCube** Collaboration, R. Abbasi *et. al.*, "The IceCube Neutrino Observatory IV: Searches for Dark Matter and Exotic Particles," arXiv:1111.2738.

[79] H. Yuksel, S. Horiuchi, J. F. Beacom, and S. Ando, "Neutrino Constraints on the Dark Matter Total Annihilation Cross Section," *Phys. Rev.* **D76** (2007) 123506, arXiv:0707.0196.

[80] B. Dasgupta and R. Laha, "Neutrinos in IceCube/KM3NeT as probes of Dark Matter Substructures in Galaxy Clusters," *Phys. Rev.* **D86** (2012) 093001, arXiv:1206.1322.

[81] C. Savage, G. Gelmini, P. Gondolo, and K. Freese, "Compatibility of DAMA/LIBRA dark matter detection with other searches," *J. Cosmol. Astropart. P.* **0904** (2009) 010, arXiv:0808.3607.

[82] J. L. Feng, J. Kumar, D. Marfatia, and D. Sanford, "Isospin-Violating Dark Matter," *Phys. Lett.* **B703** (2011) 124–127, arXiv:1102.4331.

[83] C. Rott, T. Tanaka, and Y. Itow, "Enhanced Sensitivity to Dark Matter Self-annihilations in the Sun using Neutrino Spectral Information," *J. Cosmol. Astropart. P.* **1109** (2011) 029, arXiv:1107.3182.

[84] **Super-Kamiokande Collaboration** Collaboration, T. Tanaka *et. al.*, "An Indirect Search for WIMPs in the Sun using 3109.6 days of upward-going muons in Super-Kamiokande," *Astrophys. J.* **742** (2011) 78, arXiv:1108.3384.

[85] **CoGeNT** Collaboration, C. Aalseth *et. al.*, "Results from a Search for Light-Mass Dark Matter with a P-type Point Contact Germanium Detector," *Phys. Rev. Lett.* **106** (2011) 131301, arXiv:1002.4703.

[86] **XENON100** Collaboration, E. Aprile *et. al.*, "Dark Matter Results from 100 Live Days of XENON100 Data," *Phys. Rev. Lett.* **107** (2011) 131302, arXiv:1104.2549.

[87] **CDMS** Collaboration, R. Agnese *et. al.*, "Dark Matter Search Results Using the Silicon Detectors of CDMS II," *Phys. Rev. Lett.* (2013) arXiv:1304.4279.

[88] **LUX** Collaboration, D. Akerib *et. al.*, "First results from the LUX dark matter experiment at the Sanford Underground Research Facility," arXiv:1310.8214.

[89] **DAMA/LIBRA** Collaboration, R. Bernabei *et. al.*, "New results from DAMA/LIBRA," *Eur. Phys. J.* **C67** (2010) 39–49, arXiv:1002.1028.

[90] P. Gondolo *et. al.*, "DarkSUSY: Computing supersymmetric dark matter properties numerically," *J. Cosmol. Astropart. P.* **0407** (2004) 008, arXiv:astro-ph/0406204.

[91] J. Edsjö, "WimpSim Neutrino Monte Carlo." http://www.fysik.su.se/~edsjo/wimpsim/, 2013.

[92] W. Rolke, A. Lopez, J. Conrad, and F. James, "Limits and Confidence Intervals in presence of nuisance parameters," *Nucl. Instrum. Meth.* **A551** (2005) 493–503, arXiv:physics/0403059v5.

[93] J. F. Navarro, C. S. Frenk, and S. D. M. White, "The Structure of Cold Dark Matter Halos," *Astrophys. J.* **462** (1996) 563–575, arXiv:astro-ph/9508025.

[94] **IceCube** Collaboration, M. Aartsen *et. al.*, "The IceCube Neutrino Observatory Part IV: Searches for Dark Matter and Exotic Particles," arXiv:1309.7007.

[95] C. Aalseth, P. Barbeau, J. Colaresi, J. Collar, J. Diaz Leon, *et. al.*, "Search for an Annual Modulation in a P-type Point Contact Germanium Dark Matter Detector," *Phys. Rev. Lett.* **107** (2011) 141301, arXiv:1106.0650.

[96] V. Baum, L. Demirörs, L. Köpke, and M. Ribordy, "Supernova detection with icecube and beyond," in *International Cosmic Ray Conference*, vol. 8 of *International Cosmic Ray Conference*, 2011.

[97] T. Gaisser, *Cosmic Rays and Particle Physics*. Cambridge University Press, 1991.

[98] D. Heck, G. Schatz, T. Thouw, J. Knapp, and J. Capdevielle, "CORSIKA: A Monte Carlo code to simulate extensive air showers," *Forschungszentrum Karlsruhe Report FZKA 6019* (1998).

[99] L. Hüdepohl, B. Müller, H.-T. Janka, A. Marek, and G. G. Raffelt, "Neutrino signal of electron-capture supernovae from core collapse to cooling," *Phys. Rev. Lett.* **104** (2010) 251101.

[100] M. Ribordy, "Methods and problems in neutrino observatories," `arXiv:1205.4965`.

[101] M. T. Keil, G. G. Raffelt, and H.-T. Janka, "Monte carlo study of supernova neutrino spectra formation," *Astrophys. J.* **590** (2003) 971.

[102] **IceCube** Collaboration, R. Abbasi *et. al.*, "The IceCube data acquisition system: Signal capture, digitization, and timestamping," *Nucl. Instrum. Meth.* **A601** (2009) 294–316.

[103] **IceCube** Collaboration, M. Aartsen *et. al.*, "Observation of the cosmic-ray shadow of the Moon with IceCube," `arXiv:1305.6811`.

[104] **IceCube** Collaboration, D. Chirkin, "Evidence of optical anisotropy of the South Pole ice," *Proceedings of 33rd International Cosmic Ray Conference (ICRC2013)* (2013).

[105] A. Gazizov and M. P. Kowalski, "ANIS: High energy neutrino generator for neutrino telescopes," *Comput. Phys. Commun.* **172** (2005) 203–213, `arXiv:astro-ph/0406439`.

[106] C. Andreopoulos, A. Bell, D. Bhattacharya, F. Cavanna, J. Dobson, *et. al.*, "The genie neutrino monte carlo generator," *Nucl. Instrum. Meth.* **A614** (2010) 87–104, `arXiv:0905.2517`.

[107] M. Sajjad Athar, M. Honda, T. Kajita, K. Kasahara, and S. Midorikawa, "Atmospheric neutrino flux at INO, South Pole and Pyhäsalmi," *Phys. Lett.* **B718** (2013) 1375–1380, `arXiv:1210.5154`.

[108] D. Chirkin and W. Rhode, "Muon Monte Carlo: A High-precision tool for muon propagation through matter," `arXiv:hep-ph/0407075`.

[109] S. Böser, M. Kowalski, L. Schulte, N. L. Strotjohann, and M. Voge, "Detecting extra-galactic supernova neutrinos in the Antarctic ice," arXiv:1304.2553.

[110] L. Schulte, M. Voge, A. Hoffmann, S. Böser, L. Köpke, *et. al.*, "A large-area single photon sensor employing wavelength-shifting and light-guiding technology," arXiv:1307.6713.

[111] **KM3NeT** Collaboration, L. Classen and O. Kalekin, "Status of the PMT development for KM3NeT," *Nucl. Instrum. Meth.* **A725** (2013) 155–157.

[112] C. Pryke, A. Karle, and C. Kulesa, eds., *Report from the Workshop "Astrophysics from the South Pole: Status and Future Prospects"*. 2011.

[113] M. G. Burton, X. Cui, and N. F. H. Tothill, eds., *Symposium S288 (Astrophysics from Antarctica)*, vol. 8 of *Proceedings of the International Astronomical Union*. 2012.

[114] X. Qian, A. Tan, W. Wang, J. Ling, R. McKeown, and C. Zhang, "Statistical evaluation of experimental determinations of neutrino mass hierarchy," *Phys. Rev.* **D86** (2012) 113011.

[115] E. Ciuffoli, J. Evslin, and X. Zhang, "Confidence in a Neutrino Mass Hierarchy Determination," arXiv:1305.5150.

[116] R. J. Barlow and C. Beeston, "Fitting using finite Monte Carlo samples," *Comput. Phys. Commun.* **77** (1993) 219–228.